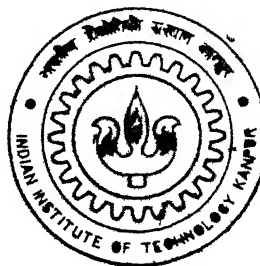


40106

**CORRELATION OF TEXTURES AND  
MICROSTRUCTURES IN A SERIES OF  
Ni-Co ALLOYS**

By

**Krishnendu Mukherjee**



893C

**DEPARTMENT OF MATERIALS AND METALLURGICAL ENGINEERING  
Indian Institute of Technology Kanpur  
APRIL, 2002**

# **CORRELATION OF TEXTURES AND MICROSTRUCTURES IN A SERIES OF Ni-Co ALLOYS**

A Thesis Submitted  
in Partial Fulfilment of the Requirements  
for the Degree of

**MASTER OF TECHNOLOGY**

By

**KRISHNENDU MUKHERJEE**

To the

**DEPARTMENT OF MATERIALS AND METALLURGICAL ENGINEERING**

**Indian Institute of Technology, Kanpur**

**APRIL, 2002**

4 FEB 2003

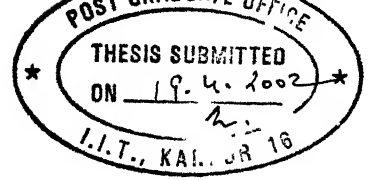
पुरुषोत्तम काशीनाथ केनकर पुस्तकालय

भारतीय प्रौद्योगिकी संस्थान कानपुर

अवाप्ति क्र० A-141866



A141866



## CERTIFICATE

This is to certify that the present work, entitled "**CORRELATION OF TEXTURES AND MICROSTRUCTURES IN A SERIES OF Ni-Co ALLOYS**" by Mr. Krishnendu Mukherjee has been carried out under our supervision and to the best of our knowledge it has not been submitted elsewhere for a degree.

**Dr. R.K. Ray**  
Professor  
Dept. of Materials & Metallurgical Engg.  
Indian Institute of Technology  
Kanpur

Date: 19/04/2002

**Dr. S. Sangal**  
Professor  
Dept. of Materials & Metallurgical Engg.  
Indian Institute of Technology  
Kanpur

Date: 19/4/02



## ACKNOWLEDGEMENT

---

I would like to convey my deepest sense of indebtedness and gratitude to my thesis supervisors **Prof. R. K. Ray** and **Prof. S. Sangal** for their inspiring guidance in every phase of this work.

I sincerely acknowledge the help and support rendered by Dr. Mungole to allow me to use the Image Analyzer of the Metallography Lab.

I would like to convey my sincere thanks to Mr. V. Kumar for extending all possible and sincere help through the course of this study and I feel very fortunate to have a laboratory assistant like him.

Finally I would like to mention those integral part of my IITK life, my friends, who have made every moment of stay here at IITK to rejoice in future. The list is endless, still, the support, cooperation and help rendered by my laboratory partners Suhas, Pinaki, Arijit, Deepti, Lt. Sanjay Chhabra, S. Sankaran, John, Subhashis, Kausik, and Pushpender Chhillar are gratefully acknowledged. Also I am thankful to Debu, Tapas Laha, Sudin, Natida, Sona, Amlan, Parthada, Sagnik, Santanu, Dulal, and Projitda for helping me in various ways.

Krishnendu Mukherjee

# CONTENTS

Page No.

## LIST OF FIGURES

## LIST OF TABLES

## ABSTRACT

1. INTRODUCTION.....	1
2. LITERATURE REVIEW.....	4
2.1 THE NICKEL-COBALT SYSTEM.....	4
2.2 THE COLD WORKED STATE.....	4
2.2.1 MICROSTRUCTURAL FEATURES OF THE COLD WORKED STATE.....	6
2.2.2 THE STORED ENERGY PRODUCED BY COLD WORKING.....	6
2.3 RECOVERY.....	6
2.3.1 RECOVERY MECHANISM.....	6
2.4 PRIMARY RECRYSTALLISATION.....	7
2.4.1 CLASSICAL NUCLEATION MODEL.....	7
2.4.2 SUBGRAIN GROWTH MODEL.....	7
2.4.3 STRAIN INDUCED BOUNDARY MIGRATION.....	7
2.5 GRAIN BOUNDARY MIGRATION.....	8
2.6 CONTINUOUS GRAIN GROWTH.....	9
2.7 MEASUREMENT OF TEXTURE.....	9
2.8 ROLLING TEXTURE OF Ni-Co ALLOYS.....	14
2.9 RECRYSTALLISATION TEXTURE.....	18
2.10 ESTIMATION OF GRAIN BOUNDARY ENERGY DISTRIBUTION.....	22
2.11 RELATION BETWEEN PDA AND TDA.....	24

<b>3. MATERIAL, MICROSCOPY AND IMAGE ANALYSIS.....</b>	<b>32</b>
3.1 MATERIAL AND INITIAL TREATMENT.....	32
3.2 COLD ROLLING.....	32
3.3 ANNEALING.....	32
3.4 TEXTURE MEASUREMENT.....	33
3.5 OPTICAL MICROSCOPY.....	33
3.6 IMAGE PROCESSING ALGORITHM.....	33
3.6.1 BINARIZATION/ THRESHOLDING.....	34
3.6.2 DILATION FILTERING.....	34
3.6.3 EROSION FILTERING.....	34
3.6.4 THINNING MORPHOLOGICAL FILTER.....	34
3.6.5 BITMAPS.....	40
3.7 TRIPLE POINT DETECTION.....	40
3.8 EVALUATION OF PLANE DIHEDRAL ANGLES (PDA).....	43
3.9 TRANSFORMATION OF PDA DISTRIBUTION TO TDA DISTRIBUTION.....	46
3.10 RELATIVE GRAIN BOUNDARY ENERGIES.....	46
<b>4. RESULTS AND ANALYSIS.....</b>	<b>47</b>
<b>5. DISCUSSION.....</b>	<b>122</b>
<b>6. CONCLUSIONS.....</b>	<b>125</b>
<b>REFERENCES.....</b>	<b>126</b>

## **APPENDIX**

## LIST OF FIGURES

Figure No.	Title of the figures	Page No.
2.1	Nickel-Cobalt equilibrium diagram	5
2.2	The rolling plane and rolling direction in a metal sheet subjected to rolling.	10
2.3	Schematic illustration of pole figure construction	11
2.4	(a): Specimen frame and crystallite frame. (b): The rotations for superimposing crystallite frame on reference frame. (c): Orientation space.	13
2.5	Effect of Composition on Stacking Fault Energy	15
2.6	{111} Pole figures showing the rolling textures of: (a) pure Ni; (b) Ni-10% Co; (c) Ni-20% Co; (d) Ni-30% Co; (e) Ni-40% Co; and (f) Ni-60% Co.	16
2.7	Plot Showing the Variation of $M_1$ (Volume Fraction) with % Co in Ni-Co alloys.	17
2.8	Texture of pure Copper (a) Cu type rolling texture, (b) Cube type annealing texture.	19
2.9	Schematic representation of growth of Cube Texture region during annealing.	21
2.10	Sectioning of a triple edge by a plane of polish randomly oriented at $(\theta, \phi)$ . $\alpha_1, \alpha_2$ , and $\alpha_3$ are the true dihedral angles and $\beta_1, \beta_2$ and $\beta_3$ are the corresponding plane dihedral angles; $\gamma_1, \gamma_2$ and $\gamma_3$ are the energy per unit area of the grain boundary planes.	23
2.11	An optical microstructure of a polycrystalline material. $\beta_1, \beta_2$ and $\beta_3$ are the plane dihedral angles at a triple point.	25
2.12	A polycrystalline structure (X) consisting of randomly oriented triple edges being sectioned by the plane of polish ( $T_2$ ).	26
2.13	A random section through two grain boundary planes meeting at an angle of $\alpha$ . The normal to the plane of section makes an angle $\theta$ with the z axis and the projection of the normal on the XY plane makes an angle $\phi$ with the X axis. The line of intersection of grain boundaries on plane of polish makes an angle $\beta$ .	27
3.1	(a) A typical grayscale image of a polycrystalline microstructure, (b) Bimodal gray level histogram of the image (a).	35
3.2	Transformed binary image (after applying thresholding algorithm) showing polishing/etching artefacts.	36
3.3	Result of applying dilation filter on Figure 3.2. The disappearance of peninsulas and etching artefacts is noticeable.	37
3.4	Image of microstructure obtained after erosion filter was applied on the image shown in Figure 3.3. It is noticeable here that the grain boundary has become continuous.	38

3.5	Image of the resultant microstructure after application of thinning filter on the image shown in Figure 3.4. The grain boundaries are now only one pixel thick.	39
3.6	Bitmap of the marked rectangular region in Figure 3.5. '0' refers to grain boundary pixels and '1' refers to matrix pixels.	41
3.7	A partial configurations of valid triple points. Remaining configurations can be generated rotating the matrices through $\pi/2$ , $\pi$ and $3\pi/2$ .	42
3.8	Illustration of pseudo triple points.	42
3.9	Tangents (thick lines) drawn to the fitted grain boundary segments (thin lines) at a triple point 'O'. 'A' and 'B' are arbitrary points on the segments.	45
3.10	Schematic of cumulative distribution for true dihedral angles: (a) $\alpha_{\max}$ , (b) $\alpha_{\min}$ . $\rho_1$ and $\rho_2$ are randomly generated number. $x_1$ and $x_2$ are corresponding $\alpha_{\max}$ and $\alpha_{\min}$ .	45
4.1	Micrographs of different Ni-Co alloys annealed for 15 minutes.	48
4.2	Micrographs of different Ni-Co alloys annealed for 30 minutes.	49
4.3	Micrographs of different Ni-Co alloys annealed for 1 hour.	50
4.4	Micrographs of different Ni-Co alloys annealed for 3 hours.	51
4.5	Micrographs of different Ni-Co alloys annealed for 10 hours.	52
4.6	Micrographs of different Ni-Co alloys annealed for 20 hours.	53
4.7	Micrographs of different Ni-Co alloys annealed for 50 hours.	54
4.8	Micrographs showing processed structure of different Ni-Co alloys annealed for 1 hour.	55
4.9	Micrographs showing processed structure of different Ni-Co alloy annealed for 50 hours.	56
4.10	Frequency distribution of relative energy ratio $\gamma_1/\gamma_3$ of different Ni-Co alloys annealed for 15 minutes.	58
4.11	Frequency distribution of relative energy ratio $\gamma_1/\gamma_3$ of different Ni-Co alloys annealed for 30 minutes.	59
4.12	Frequency distribution of relative energy ratio $\gamma_1/\gamma_1$ of different Ni-Co alloys annealed for 1 hour.	60
4.13	Frequency distribution of relative energy ratio $\gamma_1/\gamma_3$ of different Ni-Co alloys annealed for 3 hours.	61
4.14	Frequency distribution of relative energy ratio $\gamma_1/\gamma_3$ of different alloys annealed for 10 hours.	62
4.15	Frequency distribution of $\gamma_1/\gamma_3$ energy ratio of different alloys annealed for 20 hours.	63
4.16	Frequency distribution of relative energy ratio $\gamma_1/\gamma_3$ of different Ni-Co alloys annealed for 50 hours.	64
4.17	Frequency distribution of relative energy ratio $\gamma_2/\gamma_3$ of different Ni-Co alloys annealed for 15 minutes.	65
4.18	Frequency distribution of relative energy ratio $\gamma_2/\gamma_3$ of different Ni-Co alloys annealed for 30 minutes.	66
4.19	Frequency distribution of relative energy ratio $\gamma_2/\gamma_3$ of different Ni-Co alloys annealed for 1 hour.	67
4.20	Frequency distribution of relative energy ratio $\gamma_2/\gamma_3$ of different Ni-Co alloys annealed for 3 hours.	68

4.21	Frequency distribution of relative energy ratio $\gamma_2/\gamma_3$ of different Ni-Co alloys annealed for 10 hours.	69
4.22	Frequency distribution of relative energy ratio $\gamma_2/\gamma_3$ of different Ni-Co alloys annealed for 20 hours.	70
4.23	Frequency distribution of relative energy ratio $\gamma_2/\gamma_3$ of different Ni-Co alloys annealed for 50 hours.	71
4.24	Frequency distribution of relative grain boundary energy ratio $\gamma_1/\gamma_3$ for Ni-10% Co samples subjected to different annealing times.	72
4.25	Frequency distribution of relative grain boundary energy ratio $\gamma_1/\gamma_3$ for Ni-20% Co samples subjected to different annealing times.	73
4.26	Frequency distribution of relative grain boundary energy ratio $\gamma_1/\gamma_3$ for Ni-30% Co samples subjected to different annealing times.	74
4.27	Frequency distribution of relative grain boundary energy ratio $\gamma_1/\gamma_3$ for Ni-40% Co samples subjected to different annealing times.	75
4.28	Frequency distribution of relative grain boundary energy ratio $\gamma_1/\gamma_3$ for Ni-60% Co samples subjected to different annealing times.	76
4.29	Frequency distribution of relative grain boundary energy ratio $\gamma_2/\gamma_3$ for Ni-10% Co samples subjected to different annealing times.	77
4.30	Frequency distribution of relative grain boundary energy ratio $\gamma_2/\gamma_3$ for Ni-20% Co samples subjected to different annealing times.	78
4.31	Frequency distribution of relative grain boundary energy ratio $\gamma_2/\gamma_3$ for Ni-30% Co samples subjected to different annealing times.	79
4.32	Frequency distribution of relative grain boundary energy ratio $\gamma_2/\gamma_3$ for Ni-40% Co samples subjected to different annealing times.	80
4.33	Frequency distribution of relative grain boundary energy ratio $\gamma_2/\gamma_3$ for Ni-60% Co samples subjected to different annealing times.	81
4.34	The variation of frequencies of different classes of $\gamma_1/\gamma_3$ as a function of annealing time for Ni-10% Co samples.	83
4.35	The variation of frequencies of different classes of $\gamma_1/\gamma_3$ as a function of annealing time for Ni-20% Co samples.	84
4.36	The variation of frequencies of different classes of $\gamma_1/\gamma_3$ as a function of annealing time for Ni-30% Co samples.	85
4.37	The variation of frequencies of different classes of $\gamma_1/\gamma_3$ as a function of annealing time for Ni-40% Co samples.	86
4.38	The variation of frequencies of different classes of $\gamma_1/\gamma_3$ as a function of annealing time for Ni-60% Co samples.	87
4.39	The variation of frequencies of different classes of $\gamma_2/\gamma_3$ as a function of annealing time for Ni-10% Co samples.	88

4.40	The variation of frequencies of different classes of $\gamma_2/\gamma_3$ as a function of annealing time for Ni-20% Co samples.	89
4.41	The variation of frequencies of different classes of $\gamma_2/\gamma_3$ as a function of annealing time for Ni-30% Co samples.	90
4.42	The variation of frequencies of different classes of $\gamma_2/\gamma_3$ as a function of annealing time for Ni-40% Co samples.	91
4.43	The variation of frequencies of different classes of $\gamma_2/\gamma_3$ as a function of annealing time for Ni-60% Co samples.	92
4.44	The variation of mean of relative energy ratio $\gamma_1/\gamma_3$ of different alloys as a function of annealing time.	93
4.45	The variation of mean of relative energy ratio $\gamma_2/\gamma_3$ of different alloys as a function of annealing time.	94
4.46	The variation of co-efficient of variation of relative energy ratio $\gamma_1/\gamma_3$ of different alloys as a function of annealing time.	96
4.47	The variation of co-efficient of variation of relative energy ratio $\gamma_2/\gamma_3$ of different alloys as a function of annealing time.	97
4.48	Variation of intensity of cube component as a function of annealing time for different samples.	108
4.49	Variation of volume fraction of cube component as a function of annealing time for different samples.	109
4.50	Variation of intensity of cube component as a function of Co content and subjected to different annealing times.	111
4.51	Variation of volume fraction of cube component as a function of Co content and subjected to different annealing times.	112
4.52	Variation of volume fraction of cube and its twin component as a function of annealing time for different samples.	113
4.53	Variation of volume fraction of cube and its twin component as a function of Co content and subjected to different annealing times.	114
4.54	Variation of intensity of BsT component $\{437\}<4\ 11\ 7>$ as a function of annealing time for different samples.	115
4.55	Variation of volume fraction of BsT component $\{437\}<4\ 11\ 7>$ as a function of annealing time for different samples.	116
4.56	Variation of intensities of different texture components in Ni-40% Co alloy as a function of annealing time.	118
4.57	Variation of volume fractions of different texture components in Ni-40% Co alloy as a function of annealing time.	119
4.58	Variation of intensities of different texture components in Ni-60% Co alloy as a function of annealing time.	120
4.59	Variation of volume fractions of different texture components in Ni-60% Co alloy as a function of annealing time.	121

## LIST OF TABLES

Table No.	Title of the tables	Page No.
2.1	Physical properties of nickel and cobalt	4
2.2	Computed values of the coefficients $a_{ij}$ .	31
3.1	Chemical Composition of the Alloys	32
4.1-4.30	Texture components and their weightage	98



## **ABSTRACT**

An attempt has been made to correlate crystallographic texture with microstructure in a series of Ni-Co alloys in the recrystallised condition and during the grain growth stage. For this purpose Ni-10%Co, Ni-20%Co, Ni-30%Co, Ni-40% Co, and Ni-60%Co (all in wt.%) alloys were cold rolled 95% at room temperature and then subsequently recrystallisation annealed at 800°C for various lengths of time varying between 15 minutes to 50 hours. Crystallographic texture in the form of pole figures and ODFs, were measured for the different heat-treated samples. Optical microscopy was carried out and an automated methodology, based on image processing and analysis, has been developed in order to evaluate the plane dihedral angles and then the true dihedral angles in the microstructures. The relative grain boundary energy ratios were evaluated from the true dihedral angles.

The recrystallisation textures of Ni-10% Co to Ni-30% Co alloys are very similar. These are comprised of mainly the cube, its twin components, and the BsT component. In Ni-40% Co alloy the important recrystallisation texture components are the BsR component, the  $\{279\}\langle 7\ 11\ 7\rangle$  component, the retained S component, and the cube component. The recrystallisation texture of Ni-60% Co alloy consists mainly of rotated Goss component and the component  $\{011\}\langle 114\rangle$ . The frequency distribution of the grain boundary energy ratios correspond well with the volume fraction of the texture components in all the five alloys after 20 hours of annealing treatment.

# CHAPTER 1

## INTRODUCTION

---

The properties of a polycrystalline material are functions of both microstructure and grain orientation. By varying the processing parameters of a material we can get desired microstructure as well as grain orientation. If a correlation between the two can be found out we can get both desired microstructure and desired grain orientation together. There are different aspects of microstructure e.g. grain size, grain boundary roughness, dihedral angle. Amongst them dihedral angle is an important parameter as it gives an idea of the relative grain boundary energy.

The common materials of industrial practice are polycrystalline aggregates in which each of the individual grains may have an orientation that differs from those of its neighbors. In natural practice however, it is quite unusual for the grains in such materials to have a random distribution of orientations. These non-random distributions are called preferred orientations or texture.

Texture in material is developed by mainly four ways:

1. Solidification texture: It is the texture developed during the solidification of liquid material.
2. Deformation texture: A material which has undergone a severe amount of deformation as in rolling will develop a preferred orientation, or texture, in which certain crystallographic planes tend to orient themselves in a preferred manner with respect to the direction of maximum strain. In case of a single crystal the slip planes tend to rotate parallel to the axis of principal strain. The same situation exists in a polycrystalline aggregate, but the complex interactions between the multiple slip system makes analysis of the polycrystalline situation much more difficult. Since the individual grains in a polycrystalline aggregate cannot rotate freely, the lattice bending and fragmentation will occur [Ref. 1].
3. Annealing texture: The recrystallisation of a cold-worked material generally produces a preferred orientation which is different from that existing in the deformed material. This is called an annealing texture, or recrystallisation texture. An outstanding example is the cube texture in copper, where the {100} plane lies

parallel to the rolling plane with a  $\langle 001 \rangle$  direction parallel to the direction of rolling.

4. Transformation texture: It is the texture developed during the change of phase by heat treatment.

Deformation texture is an internal property of the material itself. It depends on the deformation mode of the material and the deformation mode depends on the stacking fault energy (SFE) of the material, which is a material property.

In FCC materials usually three different types of deformation textures are observed:

1. Brass or alloy type textures in low SFE materials.
2. Copper or pure metal type texture in medium SFE materials.
3. Aluminium type texture in very high SFE materials.

While in the brass type there is only the brass component  $\{110\}\langle 112 \rangle$  but in the copper type the Cu  $\{112\}\langle 111 \rangle$ , S  $\{123\}\langle 634 \rangle$  and brass components are nearly equally strong. The S component predominates in the aluminium type texture.

Pure nickel has high SFE ( $\sim 250 \text{ mJ m}^{-2}$ ). Addition of cobalt to nickel reduces the SFE of the alloy drastically. So, in the Ni-Co binary (FCC solid solution) a wide range of alloys with different values of SFE can be developed just by changing the composition (i.e. the cobalt content). Change of composition directly affects the deformation mode and thereby deformation texture. This is also going to be reflected in the primary recrystallisation textures in these alloys. The textural changes are found to persist even after primary recrystallisation, i.e. during the continuous grain growth stage. Since grain growth essentially consists of the growth of crystallographically favorably oriented grains at the expense of others, grain growth should be intimately related to the textural changes.

When a high or medium SFE FCC material is annealed after heavy cold working, a strong cube texture  $\{100\}\langle 001 \rangle$  forms. This is a familiar phenomenon for the pure FCC metals like Cu, Ni etc. Aluminium is an exception, where the rolling texture is dominated by S type texture, and on recrystallisation along with the cube texture, R texture (retained rolling texture)  $\{123\}\langle 41\bar{2} \rangle$  is obtained which is very close to S type texture. On the other hand, on annealing the Bs type rolling texture yields a series of texture components.

The properties of polycrystalline materials depend a lot on the grain boundary energy. The grain boundary energy state influences the strengthening properties of the

polycrystals significantly. True dihedral angle i.e., angle between grain boundary planes meeting at a triple edge in three-dimensional structure of polycrystals is indicator of the energy state of the grain boundaries. True dihedral angle distribution as a microstructural parameter has not been generally used because of the experimental difficulty in its measurement. However a recently developed technique [Ref. 2] makes it possible for the measurement of true dihedral angles rather simple. This technique measures the true dihedral angles from the plane dihedral angles, which can be determined comparatively easily. Plane dihedral angles are measured from the microstructure with the help of suitable computational technique involving digital data processing. The application of digital data processing has several advantages e.g., statistically adequate number of data can be processed in reasonable time, accuracy level is increased. From the true dihedral angle distribution relative energies of grain boundaries can be determined. Grain boundary energy ratios can be easily determined and this can be correlated with the textural aspects of the material.

## CHAPTER 2

### LITERATURE REVIEW

---

#### 2.1: THE NICKEL-COBALT SYSTEM

In the periodic classification of elements, Nickel and Cobalt both occur in the first long period (period 4) of the transition group VIII [Ref. 3]. The basic physical properties of Nickel and Cobalt are depicted in Table 2.1.

**TABLE 2.1: PHYSICAL PROPERTIES OF NICKEL AND COBALT**

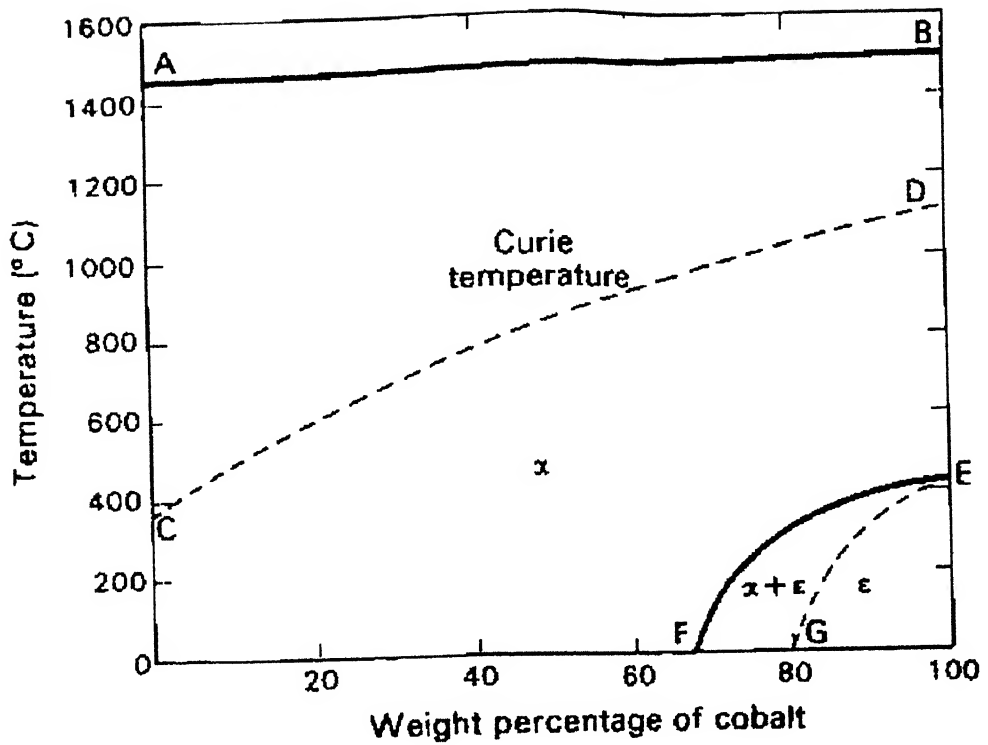
	Nickel	Cobalt
Symbol	Ni	Co
Atomic Number	28	27
Atomic Weight	58.71	58.93
Crystal Structure	FCC	HCP
Density	8908 kg m <sup>-3</sup>	8900 kg m <sup>-3</sup>
Melting Point	1453°C	1495°C
Boiling Point	2730°C	2927°C
Electronic Structure	[Ar]3d <sup>8</sup> 4s <sup>2</sup>	[Ar]3d <sup>7</sup> 4s <sup>2</sup>
Lattice Parameter	3.5238 Å	a=2.5071 Å b=2.5071 Å c=4.0695 Å

- [Ar]=1s<sup>2</sup> 2s<sup>2</sup>2p<sup>6</sup> 3s<sup>2</sup>3p<sup>6</sup>

Figure 2.1 shows the diagram of the nickel cobalt system [Ref. 4]. The effects of cobalt additions to nickel are to increase the Curie point and the magnetic saturation, and to slightly improve the mechanical properties. Nickel-cobalt alloys containing upto about 30% cobalt are formed by electrodeposition from mixed-salt electrolytes, and they have an exceptionally high hardness.

#### 2.2: THE COLD WORKED STATE

The cold worked state may be taken as any strained or damaged condition of a crystalline material brought about by processes such as plastic deformation, particle bombardment, quenching from a high temperature or phase transformations. [Ref. 5]



Point	A	B	C	D	E	F	G
°C	1453	1495	353	1121	417	0	0
%Co	0	100	0	100	100	68	80

**Figure 2.1:** Nickel-Cobalt equilibrium diagram.

The principal entities responsible for the cold worked state are point defects such as vacancies and interstitials as well as linear and planar defects like dislocations and stacking faults etc. If the deformation occurs at a sufficiently low temperature, many of these defects will be retained, leading to a thermodynamically metastable state.

### **2.2.1: MICROSTRUCTURAL FEATURES OF THE COLD WORKED STATE**

The regions inside the grains of deformed material are broken up into units of slightly misoriented “crystal domains”, which are called cells. The cell interiors are relatively free from dislocations, whereas the walls are regions of high dislocation density. The dislocation arrangements within the cell walls are complex and are often associated with small loops. The misorientations across the cell walls are found to be of the order of a degree. An increased amount of deformation results into the increase in misorientation even upto  $10^\circ$ .

### **2.2.2: THE STORED ENERGY PRODUCED BY COLD WORKING**

A small percentage (usually from 1% to 10%) of the energy expended in plastically deforming a material remains stored in the material causing an increase in the internal energy. The magnitude of the stored energy produced by cold working is affected by variables such as purity, method of deformation, temperature, grain size and composition. The energy of plastic deformation is stored in the following form:

1. Elastic strain energy
2. Energy of dislocation
3. Energy of point defects
4. Energy associated with stacking faults and twins
5. Energy associated with the destruction of ordered region

### **2.3: RECOVERY**

Recovery includes the migration of vacancies and of dislocations, leading to annihilation and rearrangement of certain portions of the grain. Recovery can be considered to be any modification of properties during annealing, which occurs before the appearance of the new strain free recrystallised grains.

#### **2.3.1: RECOVERY MECHANISM**

A cold worked metal has a cell structure. As annealing starts, the tangled dislocations in the cell wall are supposed to rearrange themselves. Some of the dislocations within

the cells are attracted to cell walls. As a result the dislocation density in the cell interior decreases gradually. The cell walls become more clearly defined and eventually form sub-grains of about the same size as the initial cells. At the later stage it starts increasing gradually.

## **2.4: PRIMARY RECRYSTALLISATION**

Recrystallisation of a deformed metal involves the nucleation and growth of new strain free grains, which may be widely different in orientation from the surrounding matrix. The new grains grow at the expense of the cold worked matrix by high angle boundary migration. The three principal models of nucleation are:

1. Classical nucleation model,
2. Sub-grain growth model,
3. Strain induced boundary migration model.

### **2.4.1: CLASSICAL NUCLEATION MODEL**

This is based on the assumption that the nucleus, which is stable and capable of growth, is formed as a result of thermal fluctuations in the sense of the classical nucleation theory of the phase transformation. This model requires the existence of an incubation period. It also predicts the preferential nucleation of recrystallised grains in the most severely deformed regions. But the main limitation of this theory is that it predicts the new grains should always be in close orientation with the adjacent cold worked matrix. Another drawback is that there is no consideration for purity of the material. However, in practical situations this theory is quite applicable.

### **2.4.2: SUBGRAIN GROWTH MODEL**

Small strain free cells can be formed in a deformed matrix by dislocation climb and rearrangement. Once a sufficiently large dislocation free cell or sub-grain has formed it can grow into its neighbourhood. The misorientation of a sub-grain relative to its immediate surrounding is more important than its size in controlling its growth.

### **2.4.3: STRAIN INDUCED BOUNDARY MIGRATION**

This is basically a model of growth since it assumes that the unstable cold worked state already has large angle boundaries of macroscopic or microscopic dimensions and that during recrystallisation these boundaries simply bow out leaving strain free materials behind. Sometimes recrystallisation does not involve any nucleation but



only growth of strain free regions brought about by grain boundary migration. This process which has been termed as strain induced boundary migration, consists of the irregular movement of an existing boundary with an irregular jagged front. According to this model there is no incubation period, since no nucleus of new orientation has to be formed. It is observed that the victim grain is the one which is more severely work hardened, as the stored energy of this grain provides the driving force for the entire process. The grain with larger cell size will have the lower energy, so that recrystallisation occurs by the movement of a portion of the boundary into the high energy grain having a smaller cell size.

## **2.5: GRAIN BOUNDARY MIGRATION**

Grain boundary migration plays an essential role in recrystallisation and subsequent grain growth. There is a marked orientation dependence of grain boundary migration. The highest migration rate in FCC metals has been obtained when the growing grain is crystallographically related to the matrix by a  $30^\circ - 40^\circ$  rotation about a common  $\langle 111 \rangle$  axis [Ref. 6].

The anisotropy of the boundary migration rate can be interpreted as due to the orientation dependence of either the driving force or the boundary mobility. In highly deformed materials, which show a complex dislocation structure, the anisotropy of driving force can be ruled out as a possibility and hence an orientation dependence of the boundary mobility is quite expected.

Recrystallisation was found to be easier in foils made from the transverse and longitudinal sections than from ones parallel to the rolling plane [Ref. 7]. This is due to the fact that the cells produced by deformation are pancake shaped with the cell boundaries lying parallel to the rolling plane. Foils, which were taken parallel to this plane, may not contain a sufficient number of cells through the thickness to allow formation of a recrystallisation nucleus with a high angle boundary. In such foils growth may also be inhibited.

The kinetics of secondary recrystallisation is affected by

1. The value and behavior of pinning force,
2. The magnitude of the driving force for grain growth [Ref. 8].

The former depends on the volume fraction, size, and the nature of the fine precipitates. The later is determined by initial grain size distribution and curvature of the moving boundaries. The two dimensional growth slows down the secondary recrystallisation when the initial average grain size exceeds one-tenth of the sheet thickness.

## **2.6: CONTINUOUS GRAIN GROWTH**

Continuous grain growth is a recrystallisation process, which proceeds without nucleation. Textures formed during this process are thus exclusively due to the orientation dependence of the grain boundary velocity which is the product of the driving force and grain boundary mobility. The mobility of a boundary depends among others, on the orientation difference  $\Delta g_0$  of the contiguous grains. The driving force in the grain coarsening is constituted by the deviation from equilibrium between the forces acting on the grain boundaries. These forces also depend on the orientation difference of the contiguous grains. In order to reduce deviation from the equilibrium state, the system lowers its free energy by enlarging the grains, thereby reducing the surface free energy. So, this is essentially a process, where a grain of a favoured orientation consumes other grains of unfavorable orientations.

## **2.7: MEASUREMENT OF TEXTURE**

Rolling plane of the material and rolling direction (crystallographic planes and direction) are needed for the determination of texture. For example, when a sheet is rolled in such a way that the (hkl) planes of most of the grains are parallel to the rolling plane, and the [uvw] direction of most of the grains is parallel to the rolling direction, then texture of the rolled sheet is represented as  $\{hkl\}\langle uvw \rangle$ , as shown in **Figure 2.2**. This is displayed by a pole figure, which is nothing but the stereographic projection on the (hkl) plane, taking (uvw) pole as the north pole. The experimental procedure of the pole figure construction is briefly shown in **Figure 2.3**. The material is first subjected to X-ray diffraction, and the intensity vs. angle data is recorded. Then these data is transformed from a linear scale to a polar plot (pole figure). Several contours shown on the pole figure account for the different orientations of different densities.

(100) poles for the orientation  $\{110\}\langle 001 \rangle$

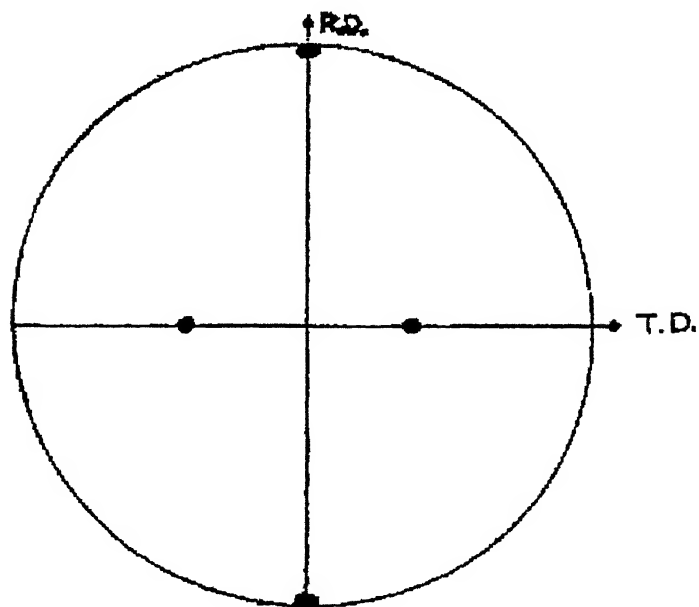
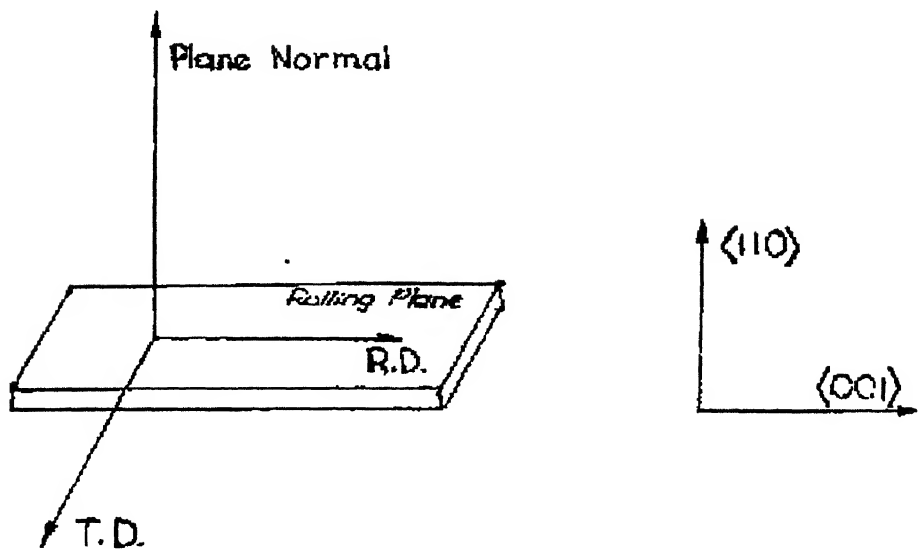
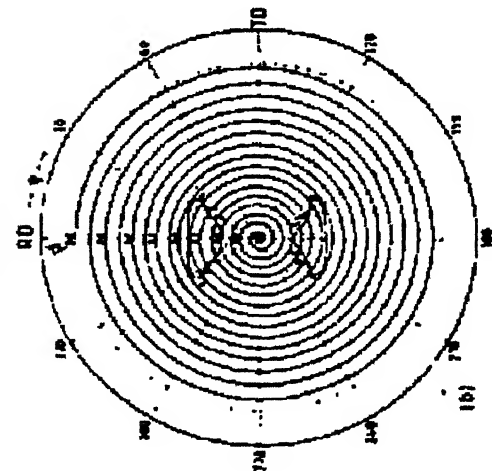
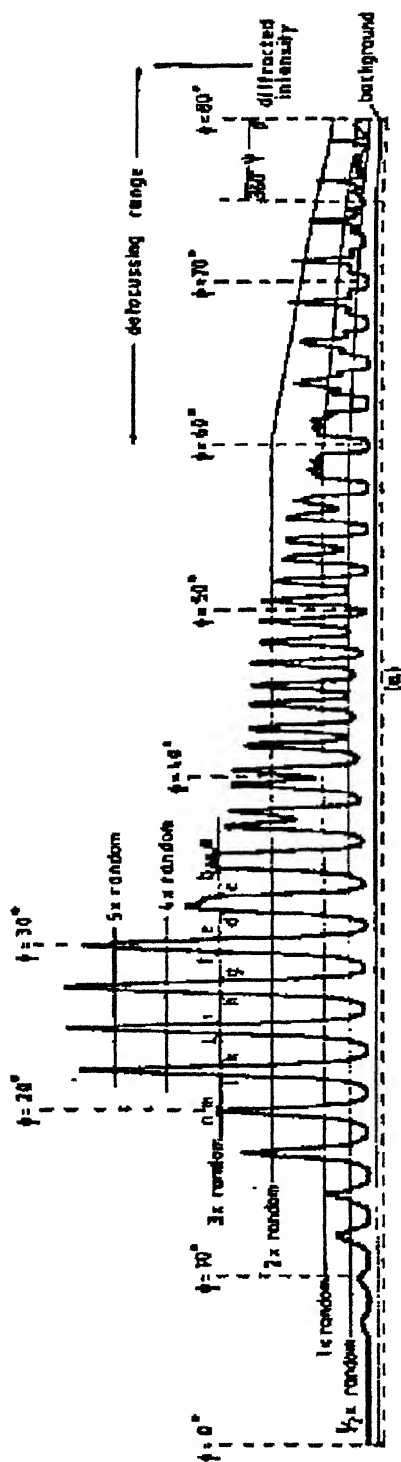


**Figure 2.2:** The rolling plane and rolling direction in a metal sheet subjected to rolling.



(a) chart recording for the (111) reflection of cold rolled aluminium (compressed steel), (b) partly plotted pole figure showing the 3 x random contour, (c) final (111) pole figure.

Figure 2.3. Schematic illustration of pole figure construction

There are few limitations of pole figure. Although exhibiting all the texture components of a material, in a pole figure, the pole of particular texture is not pinpointed, rather it is scattered throughout a zone and it becomes difficult to distinguish them perfectly. The resolution of pole figure is poor. Also, it gives only some qualitative idea about the strength of a particular texture component.

One-way of removing this difficulty is to use the crystallize orientation distribution function (CODF or ODF), which essentially describes the frequency of occurrence of particular orientations in three dimensional (Eular) orientation space. It is easily understood that a frame of three mutually perpendicular axes can be superimposed on another frame of three mutually perpendicular axes. The same principle is followed here, the specimen frame as shown in **Figure 2.4(a)** is superimposed on the crystallographic frame by means of three successive rotations (**Figure 2.4(b)**).

(a) A first rotation  $\Phi_1$  around ND transforms TD and RD into the new directions  $TD_1$  and respectively.  $\Phi_1$  has to have such a value that  $RD_1$  will be perpendicular to the plane formed by ND and [001].

(b) A second rotation  $\Phi$  around the new direction  $RD_1$  with  $\Phi$  having such a value that ND is transformed into [001] and TD into  $TD_2$ .

(c) The third rotation  $\Phi_2$  with  $\Phi_2$  having such a value that  $RD_1$  is transformed into [100] and  $TD_2$  into [010].

So,  $\Phi_1, \Phi, \Phi_2$ ; the set of these three angles completely represent an orientation of a crystal or grain. Immediately for every set of  $\{hkl\} \langle uvw \rangle$  values there is exactly one set of  $\Phi_1, \Phi, \Phi_2$  values. Now depending on this concept, a three dimensional space has been evaluated where three mutually perpendicular axes represent the values of  $\Phi_1, \Phi, \Phi_2$ ; from  $0^\circ$  to  $90^\circ$ . This is known as orientation space (**Figure 2.4(c)**), and widely used for universal texture notation [Ref. 9].

The ODF technique is not more correct process than the pole figure technique is, but of course, the resolution is much higher in this system, and also it allows the quantitative measurement of the strength of a particular texture component in volume fraction.

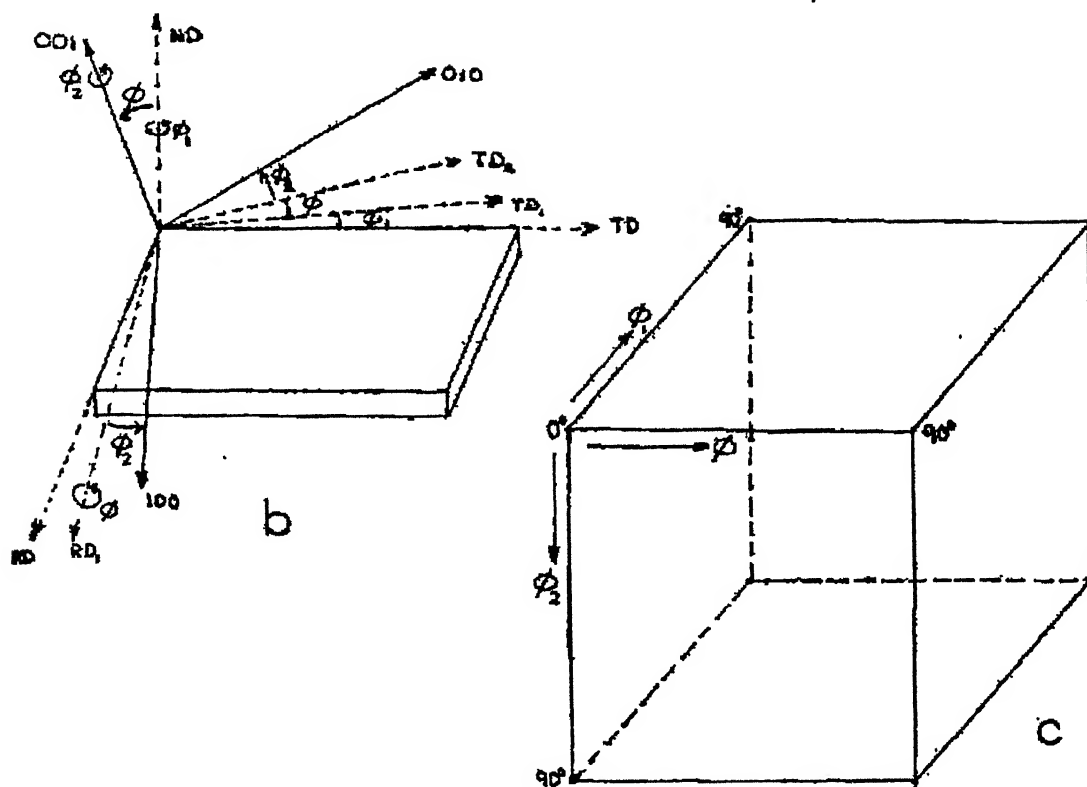
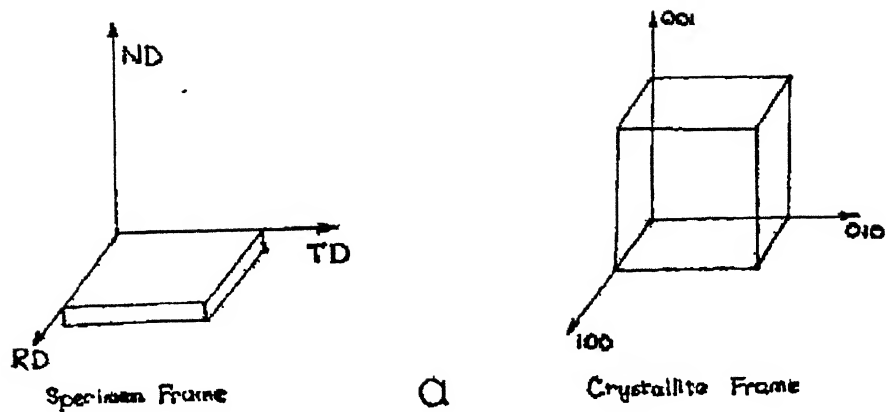


**Figure 2.4(a):** Specimen frame and crystallite frame.

**Figure 2.4(b):** The rotations for superimposing crystallite frame on reference frame.

**Figure 2.4(c):** Orientation space.

## 2.8: ROLLING TEXTURE OF Ni-Co ALLOYS

For higher stacking fault energy, the stacking fault width is very low, and the stacking faults are easily constricted. In that situation, the cross-slip becomes easier and the material undergoes slip deformation rather than twinning. When the deformation is governed by slip mode, the deformation texture is generally copper type  $\{112\}\langle 111 \rangle$ . Example, pure copper, pure nickel or nickel with low amount of cobalt, Ni-Fe alloy etc. Along with the copper components of texture other components like Bs component  $\{110\}\langle 112 \rangle$ , S component  $\{123\}\langle 634 \rangle$ , Goss component  $\{110\}\langle 001 \rangle$  etc. are present in very small percentage.

For lower SFE, the stacking fault width is much greater, which makes difficult to create any constriction within the stacking fault region and the cross-slip becomes difficult. As a result of it, the critical resolved shear stress (CRSS) for twin becomes lower than that of slip and the plastic deformation is essentially governed by the twinning process.

In Ni-Co system, the SFE significantly decreases on increasing the Co percentage (**Figure 2.5**). Accordingly it is observed that the Cu component of rolling texture gradually decreases from pure nickel to Ni-30% Co (**Figure 2.6**). Ni-40 Co shows a transition from Cu type to Bs type rolling texture, and Ni-60 Co alloy predominantly exhibits Bs type texture [**Ref. 10**].

This is also observed that Cu type texture decreases with increasing the amount of deformation. In case of Ni-40% Co alloy, the intensity of Cu type texture remarkably decreased from 40% cold rolling to 95% cold rolling.

Wassermann has shown that if mechanical twinning is an available mode of deformation in addition to normal slip, the Cu component of the rolling texture  $\{112\}\langle 111 \rangle$  will be transformed to  $\{552\}\langle 115 \rangle$  by twinning. Further deformation of the twin orientation will then take place on the favorable slip systems which will rotate this twin orientation into the Goss position  $\{011\}\langle 100 \rangle$  and finally into the Bs position  $\{011\}\langle 112 \rangle$  by further rotation. In contrast, the major component of the alloy type texture will not be affected by twinning and retain its orientation during deformation. **Figure 2.7** clearly indicates

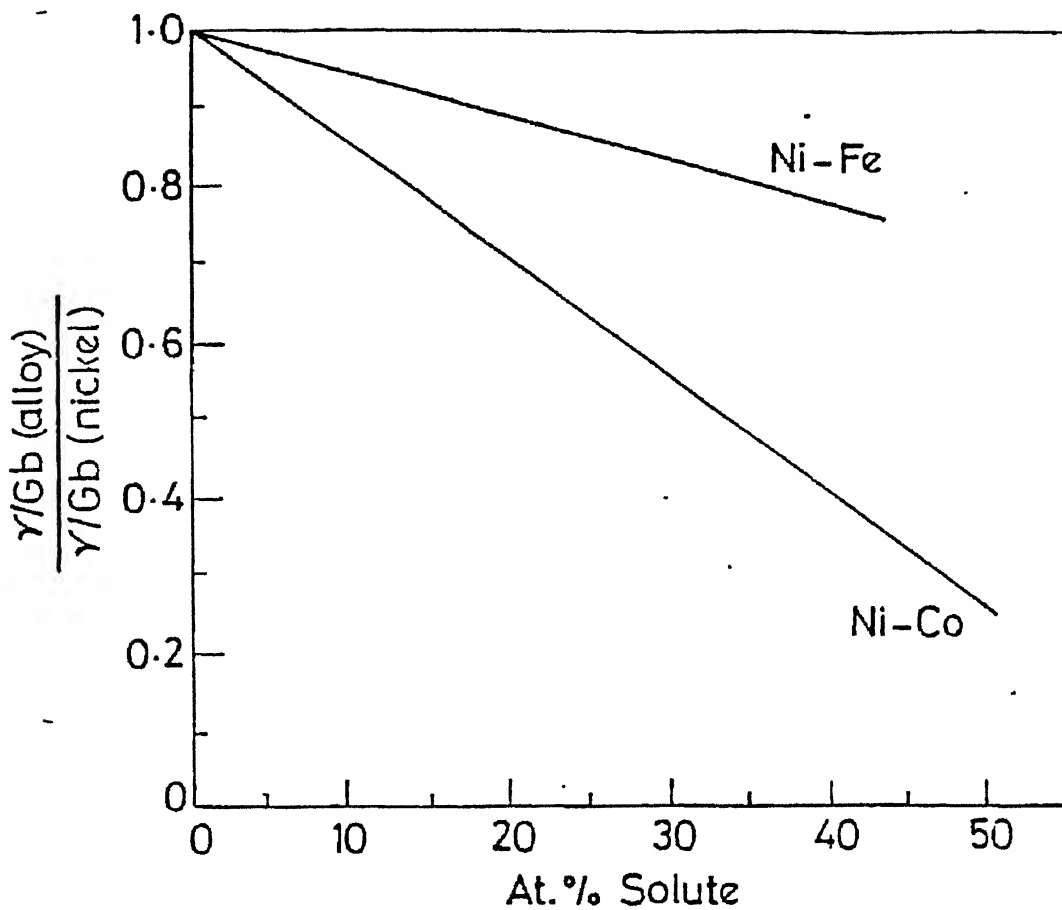


**Figure 2.5:** Effect of Composition on Stacking Fault Energy  
( $\gamma$  = Stacking Fault Energy,  $G$  = Shear Modulus,  $b$  = Burger's Vector)



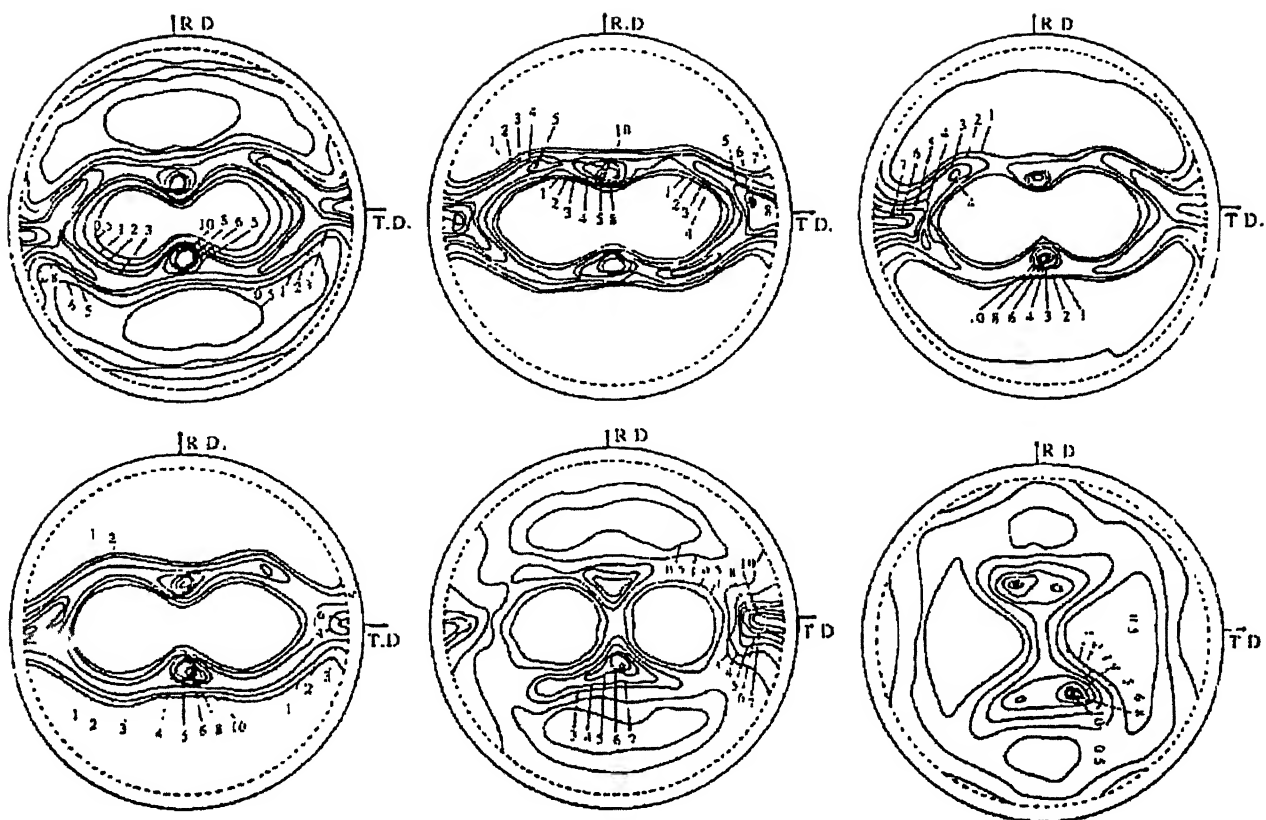


**Figure 2.6:** {111} Pole figures showing the rolling textures of: (a) pure Ni; (b) Ni-10% Co; (c) Ni-20% Co; (d) Ni-30% Co; (e) Ni-40% Co; and (f) Ni-60% Co.

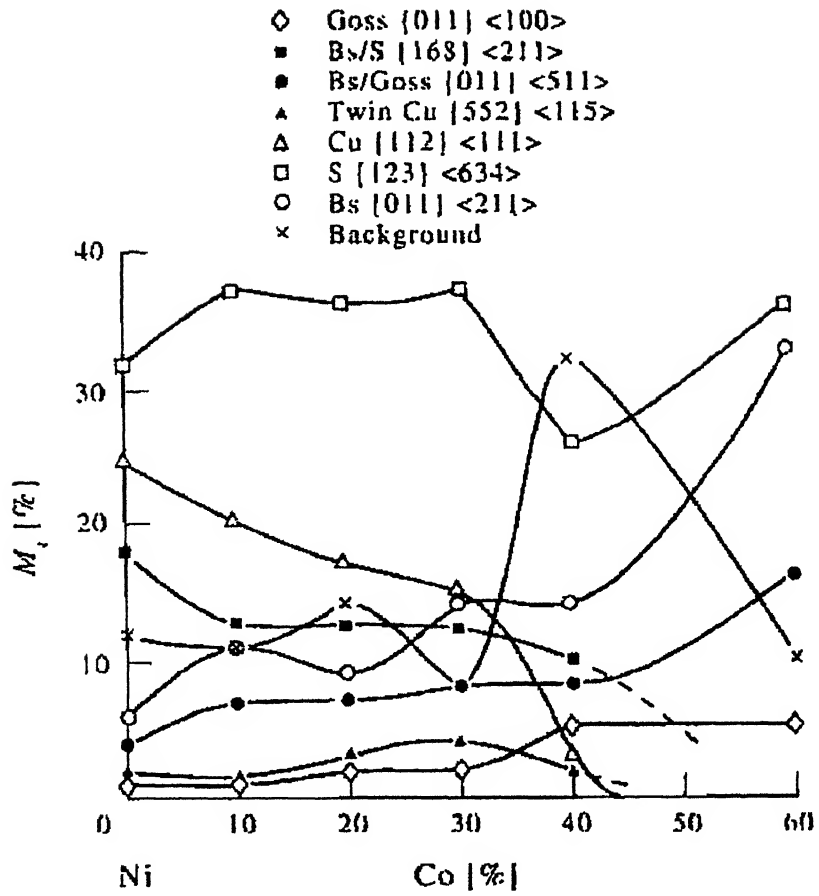


**Figure 2.7:** Plot Showing the Variation of  $M_i$  (Volume Fraction) with % Co in Ni-Co alloys

the phenomenon of dominating Cu type texture in lower Co content alloys and that Bs texture in higher Co content alloys.

Temperature plays an important role for determining the rolling texture. The slip systems are activated in larger extent at high temperature. So, at high temperature, slip deformation is more probable than twinning. Exactly, the reverse effect is expected at lower temperatures.

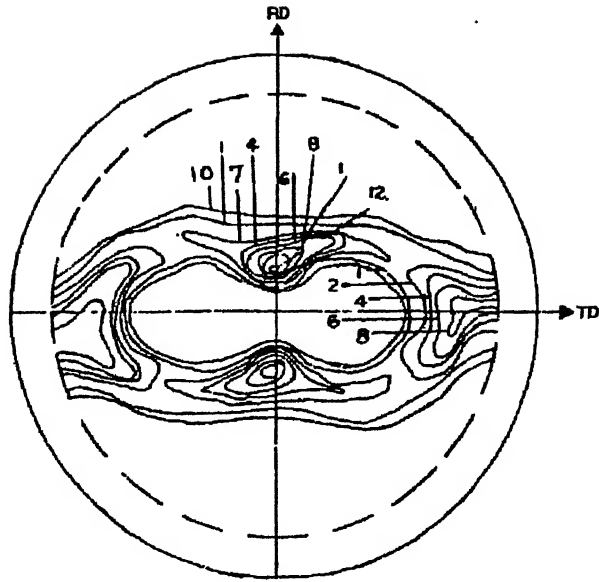
On annealing a deformed material, the rolling texture completely or partially changes to a new texture, which is the recrystallisation or annealing texture. It is also observed, that there is a one to one correspondence between the rolling texture and the annealing texture. So it can be inferred that the ultimate annealing texture of the material is dependent on the following factors:

1. Deformation mode,
2. Degree of deformation,
3. Temperature at which rolling is carried out,
4. Stacking fault energy,
5. Critical resolved shear stress for slip and twinning.

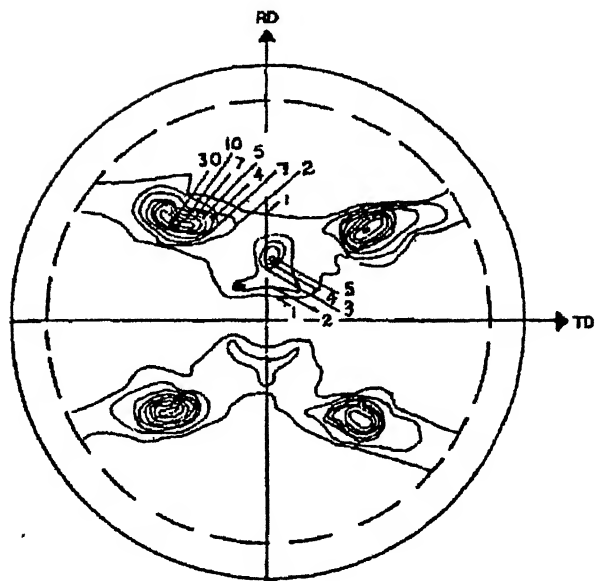
## **2.9: RECRYSTALLISATION TEXTURE**

When the cold worked material is annealed, the Cu type texture essentially changes to cube texture  $\{100\}\langle 001\rangle$ . This is a familiar phenomenon for the pure FCC metals like Cu, Ni etc. The reverse effect is observed in Bs type rolling texture. On recrystallisation it does not yield Cu type texture. The Bs texture transforms to  $\{332\}\langle 113\rangle$  type texture.

The formation of cube texture is not a desirable one so far as the material property is concerned. The formation of cube texture is a very fast process, and just after the starting of recrystallisation the complete material immediately becomes highly anisotropic. But the reason for the dominating characteristic of cube texture and its actual origin is still not very clearly known. The pole figures of 95% cold rolled pure copper and the recrystallised texture of the same have been juxtaposed in the **Figure 2.8** from which it is clearly observed that in the cold deformed alloy, a high density of material is oriented within a range of orientations near  $(211)[\bar{1}\bar{1}\bar{1}]$ . In addition, substantial amount of material is also oriented near  $(110)[\bar{1}\bar{1}\bar{2}]$  to  $(110)[00\bar{1}]$ . One of



(a)



(b)

**Figure 2.8:** Texture of pure Copper (a) Cu type rolling texture, (b) Cube type annealing texture.

the theories of recrystallisation says that the nucleus of recrystallisation texture remains in the cold rolled structure itself as small crystallites, and during the course of recrystallisation they just grow by consuming the highly strained region. This is the strain induced boundary migration theory (Block theory), which says that the nucleus of the cube texture should be present in the deformed structure itself, and it is observed that a small amount of material having orientations very near to the cube (100)[001] is also present. **Figure 2.8(b)** shows that most of the material has cube orientation for fully recrystallised alloy. The twin related component of the cube texture also appeared, around  $(221)[2\bar{1}2]$ . In addition small amounts of materials are also found having orientation spread over from  $(531)[2\bar{3}1]$  to  $(553)[5\bar{2}5]$ .

Previous experiments already proved, that among all the criteria, the presence of a cube oriented region in the deformed matrix is the most important one. Cube grains start growing from the cube oriented regions. The cube grains grow disproportionately larger than the grains of other orientation, because of:

1. Early formation, and
2. Very high boundary migration rate.

The grain boundary migration gives rise to bulging out of grain boundary, which is a very important mechanism for recrystallisation. During the recovery process, dislocation polygonisation gives rise to strain free subgrains, which in the later stage consumes the highly strained matrix in order to reduce the total free energy in the form of strain energy associated with dislocation and other crystal defects.

During the experiment carried out with pure copper, a well formed subgrain having an orientation about  $15^\circ$  from the exact (001)[100] orientation has been observed to grow very fast consuming the neighbouring regions of other orientation (**Figure 2.9**).

The extraordinary sharpness of the cube texture has been explained on the basis of oriented growth mechanism of recrystallisation. It is also observed that mobility of the grain boundary depends on the angle of the grain boundary. Low angle boundary shows lower mobility whereas higher angle grain boundaries exhibit higher mobility. In the FCC metals the fastest growing grains bear a particular orientation relationship to the deformed matrix. This is approximately  $40^\circ$  around a common  $\langle 111 \rangle$  axis. For

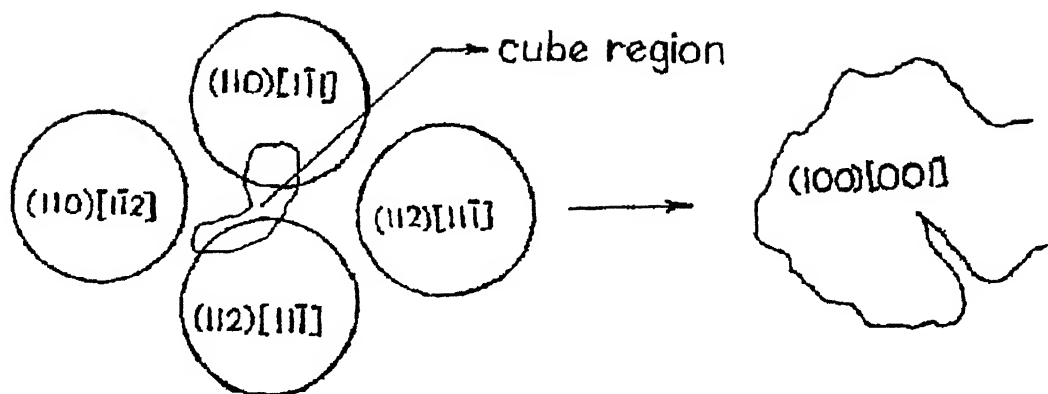


**Figure 2.9:** Schematic representation of growth of Cube Texture region during annealing.

pure copper this is around 30°. Also it maintains optimum angles with Cu, Bs textures. Grain growth is mainly a grain boundary migration and rotation process. Due to the optimum angle with the neighbouring orientations, grain rotation required for cube orientation is low, and probably this leads to the extremely low magnitude of activation energy for the growth of cube region, and the cube texture dominates over the other orientations.

## 2.10: ESTIMATION OF GRAIN BOUNDARY ENERGY DISTRIBUTION

The properties of polycrystalline materials depend a lot on the grain boundary energy. The grain boundary energy state influence the strengthening properties of the polycrystals significantly. Several methods have been developed for the estimation of energy or the relative energy state of grain boundaries. Pumphery and Gleiter [Ref. 11] have measured grain boundary energy by studying the spreading and disappearance kinetics of extrinsic grain boundary dislocations (EGBDs) in TEM during in-situ annealing. However, the technique is cumbersome as well as prone to error in the estimation of temperature and time of disappearance of EGBDs. In the traditional thermal groove method [Ref. 12], the original structure of the boundaries may undergo change. Also, the technique is limited to surface grain boundaries and may not be representative of the bulk material.

Grain boundary energy may also be related to the angles between intersecting grain boundary planes in the bulk material. Figure 2.10 shows three grain boundaries, with energies  $\gamma_1$ ,  $\gamma_2$  and  $\gamma_3$ , meeting at a triple edge. The angles (denoted as true dihedral angles),  $\alpha_1$ ,  $\alpha_2$  and  $\alpha_3$ , are the angles between the grain boundary planes in the 3-dimensional structure of polycrystals. The true dihedral angles and the energies are related by the well-known Newton equation:

$$\frac{\gamma_1}{\sin \alpha_1} = \frac{\gamma_2}{\sin \alpha_2} = \frac{\gamma_3}{\sin \alpha_3} \quad (1)$$

Previously true dihedral angle was measured directly from the TEM images in which the three dimensional structure of the grain boundary planes meeting at a triple edge can be observed. This method of measurement is tedious and therefore it is generally not feasible to obtain a good statistical estimate of the distribution of true dihedral angles. In view of the above mentioned methods, the technique developed by Sangal

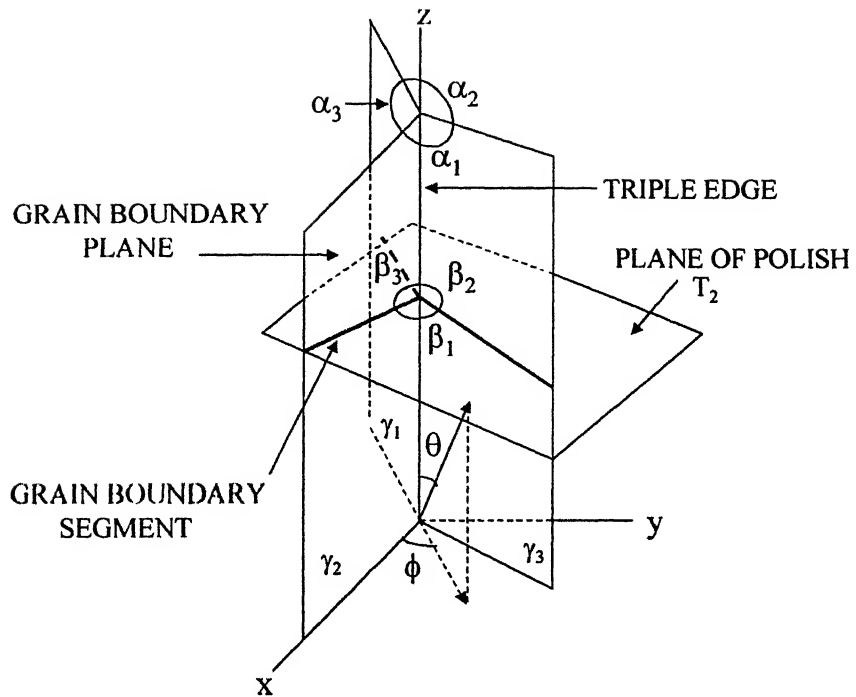


**Figure 2.10:** Sectioning of a triple edge by a plane of polish randomly oriented at  $(\theta, \phi)$ .  $\alpha_1$ ,  $\alpha_2$ , and  $\alpha_3$  are the true dihedral angles and  $\beta_1$ ,  $\beta_2$  and  $\beta_3$  are the corresponding plane dihedral angles;  $\gamma_1$ ,  $\gamma_2$  and  $\gamma_3$  are the energy per unit area of the grain boundary planes.



[Ref. 13] provides an alternative approach which involves the estimation of the distribution of true dihedral angles from a rigorous stereological analysis of angles,  $\beta_1$ ,  $\beta_2$  and  $\beta_3$ , between grain boundary segments (i.e., lines of intersection between the grain boundary planes and the sectioning plane, as shown in **Figure 2.10**). These angles are denoted as the plane dihedral angles. In a polycrystalline microstructure, the plane dihedral angles are the angles at the triple points, as indicated in **Figure 2.11**.

**Figure 2.10** shows a triple edge that is sectioned by the plane of polish P. The resulting linear grain boundary segments meeting at a triple point make plane dihedral angles,  $\beta_1$ ,  $\beta_2$  and  $\beta_3$ , corresponding to the true dihedral angles,  $\alpha_1$ ,  $\alpha_2$  and  $\alpha_3$  respectively. It is clear from the figure that the plane dihedral angles are not only a function of the true dihedral angles but also depend on the orientation of the sectioning plane which is defined by the orientation ( $\theta$ ,  $\phi$ ) of the plane normal with respect to the triple edge. **Figure 2.12** shows that in an ideal polycrystal structure the triple edges are randomly oriented in 3D space and consequently the sectioning plane has different orientations with respect to individual triple edges. Therefore, the distribution of plane dihedral angles will have two components:

- (1) variation in the true dihedral angles at various triple edges, and
- (2) statistical variation due to the random orientation of the triple edges distributed in the polycrystalline structure.

The statistical variation (like random noise) tends to overshadow or hide the actual distribution of true dihedral angles. Hence, such a distribution cannot be directly used in the estimation of grain boundary energies. However, the measurements of plane dihedral angles are relatively easy and it is possible to make a large number of such measurements in a short time. In the following section transformation procedures are discussed which can be used to unfold the distribution of true dihedral angles from the measured distribution of plane dihedral angles.

### **2.11: RELATION BETWEEN PDA AND TDA:**

**Figure 2.13** shows the random section of a triple edge by the plane of polish, P. The true dihedral angle between the grain boundary planes A and B is  $\alpha$  and the

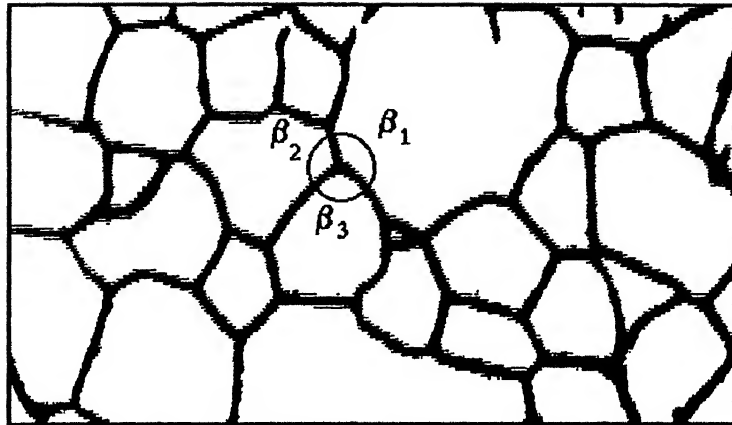


**Figure 2.11:** An optical microstructure of a polycrystalline material.  $\beta_1$ ,  $\beta_2$  and  $\beta_3$  are the plane dihedral angles at a triple point.

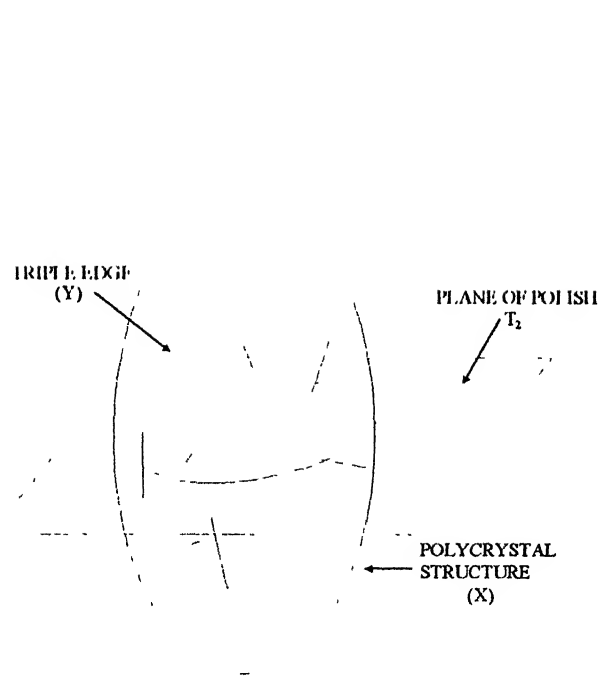


**Figure 2.12:** A polycrystalline structure (X) consisting of randomly oriented triple edges being sectioned by the plane of polish ( $T_2$ ).

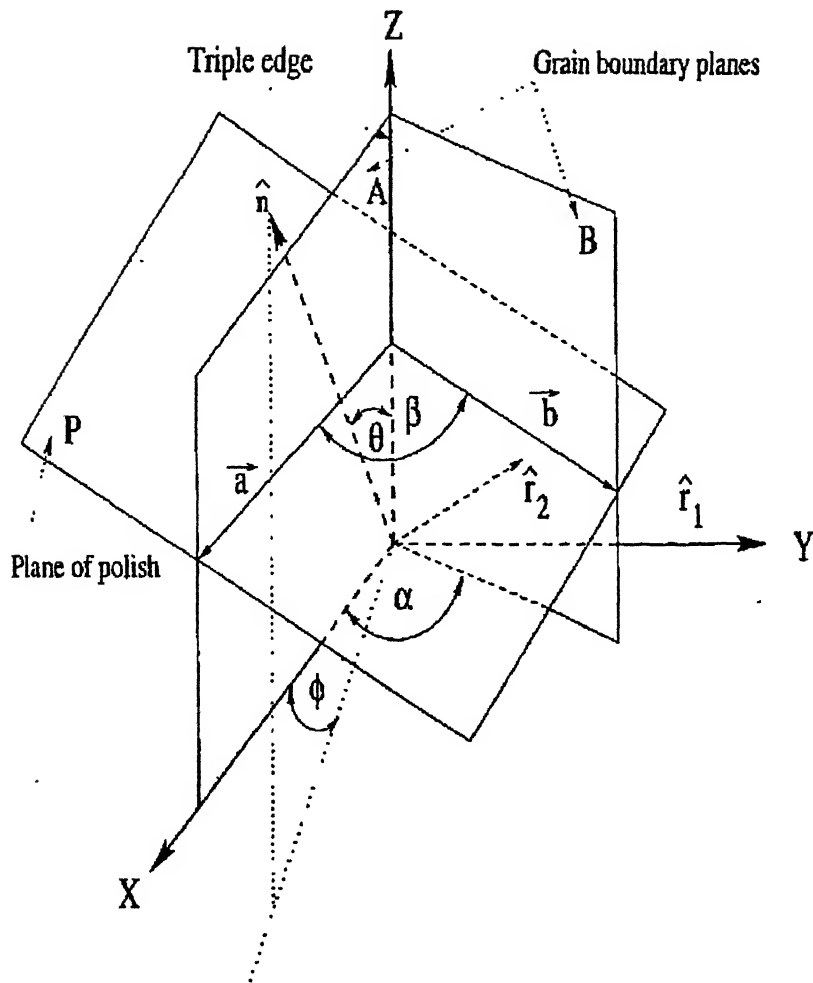


**Figure 2.13:** A random section through two grain boundary planes meeting at an angle of  $\alpha$ . The normal to the plane of section makes an angle  $\theta$  with the  $z$  axis and the projection of the normal on the  $XY$  plane makes an angle  $\phi$  with the  $X$  axis. The line of intersection of grain boundaries on plane of polish makes an angle  $\beta$ .

corresponding grain boundary segments a and b make a plane dihedral angle of  $\beta$  on the plane of polish as shown in **Figure 2.13**. The triple edge is parallel to the z-axis and the grain boundary plane A is in the XZ plane. The orientation of the plane of polish is described by the orientation of the plane normal (denoted by  $\hat{n}$ ) in terms of angle  $\phi$  and  $\theta$  in spherical coordinates. The unit vectors  $\hat{r}_1$  and  $\hat{r}_2$  are normal to the grain boundary planes A and B respectively. Let  $\vec{a}$  and  $\vec{b}$  be the vectors parallel to the grain boundary segments 'a' and 'b' respectively.

From **Figure 2.13**, the vectors  $\hat{r}_1$ ,  $\hat{r}_2$ , and  $\hat{n}$  can be expressed as follows:

$$\hat{r}_1 = \hat{j} \quad (2)$$

$$\hat{r}_2 = -\sin \alpha \hat{i} + \cos \alpha \hat{j} \quad (3)$$

$$\hat{n} = \sin \theta \cos \phi \hat{i} + \sin \theta \sin \phi \hat{j} + \cos \theta \hat{k} \quad (4)$$

Since  $\vec{a}$  is the line of intersection of planes A and P, while  $\vec{b}$  is the line of intersection of planes B and P,  $\vec{a}$  and  $\vec{b}$  can be represented by the following cross-products:

$$\vec{a} = \hat{r}_1 \times \hat{n} \quad (5)$$

and

$$\vec{b} = \hat{r}_2 \times \hat{n} \quad (6)$$

From the equations (5) to (6), and  $\vec{a}$  and  $\vec{b}$  can be expressed in the following form,

$$\vec{a} = \cos \theta \hat{i} - \sin \theta \cos \phi \hat{k} \quad (7)$$

$$\vec{b} = \cos \alpha \cos \theta \hat{i} + \sin \alpha \cos \theta \hat{j} - \sin \theta \cos(\phi - \alpha) \hat{k} \quad (8)$$

$\beta$ , the plane dihedral angle, can be expressed as:

$$\cos \beta = \frac{\vec{a} \cdot \vec{b}}{|\vec{a}| |\vec{b}|} \quad (9)$$

From equations (7) and (8) we get:

$$\begin{aligned} \vec{a} \cdot \vec{b} &= (\cos \theta \hat{i} - \sin \theta \cos \phi \hat{k}) (\cos \alpha \cos \theta \hat{i} + \sin \alpha \cos \theta \hat{j} - \sin \theta \cos(\phi - \alpha) \hat{k}) \\ \Rightarrow \vec{a} \cdot \vec{b} &= \cos^2 \theta \cos \alpha + \sin^2 \theta \cos \phi \cos(\phi - \alpha) \end{aligned} \quad (10)$$

$$|\vec{a}| = \sqrt{\cos^2 \theta + \sin^2 \theta \cos^2 \phi} = \sqrt{1 - \sin^2 \theta \sin^2 \phi} \quad (11)$$

$$|\vec{b}| = \sqrt{\cos^2 \alpha \cos^2 \theta + \sin^2 \alpha \cos^2 \theta + \sin^2 \theta \cos^2 (\phi - \alpha)} = \sqrt{1 - \sin^2 \theta \sin^2 (\phi - \alpha)} \quad (12)$$

Thus from equations 2.19 to 2.22, the following expression can be obtained

$$\cos \beta = \frac{\cos^2 \theta \cos \alpha + \sin^2 \theta \cos \phi \cos(\phi - \alpha)}{\sqrt{(1 - \sin^2 \theta \sin^2 \phi)(1 - \sin^2 \theta \sin^2 (\phi - \alpha))}} \quad (13)$$

It is seen from equation 2.23 that if  $\theta = 0$  then  $\beta = \alpha$ , as would be expected. However, for any given value of  $\alpha$ ,  $\beta$  can vary from  $0^\circ$  to  $180^\circ$  depending upon the orientation of the plane of polish.

On sectioning the polycrystalline structure (denoted as set X), the probability of an intersection of a triple edge (denoted as set Y) with the sectioning plane (denoted as set  $T_2$ ) is given by:

$$P_1(T_2 \cap Y | T_2 \uparrow X) = \frac{2l}{\pi} / H(X) \quad (14)$$

where,  $l$  is the mean length of a triple edge,  $H(X)$  is the mean tangent diameter of X. Using the above, the method has been evolved for the transformation of plane dihedral angle distribution to true dihedral angle distribution. In this method individual angles at a triple edge are considered to be independent of each other.

Consider a set  $Y_\alpha$  consisting of pairs of intersecting planes making equal angles  $\alpha$  distributed in the polycrystalline space. The intersection of  $Y_\alpha$  with the sectioning plane,  $T_2$ , will give rise to a probability distribution of plane dihedral angles given by  $p(\beta | \alpha)d\beta$ . Let the numerical density of the set  $Y_\alpha$  be  $N_V(\alpha)d\alpha$ , i.e., number of plane pairs making an angle of  $\alpha$  per unit volume. The probability density,  $g(\beta)$ , of plane dihedral angles is given by

$$g(\beta) = \frac{\int_{\alpha} P(T_2 \cap Y_\alpha | T_2 \uparrow X) p(\beta | \alpha) N_V(\alpha) d\alpha}{\int_{\alpha} P(T_2 \cap Y_\alpha | T_2 \uparrow X) N_V(\alpha) d\alpha} \quad (15)$$

Substituting  $P(T_2 \cap Y_\alpha | T_2 \uparrow X)$  from equation 14, the probability density,  $g(\beta)$  reduces to:

$$g(\beta) = \int_{\alpha} p(\beta | \alpha) f(\alpha) d\alpha \quad (16)$$

where,  $f(\alpha) = N_V(\alpha) / \int_x N_V(\alpha) d\alpha$  is the probability density of true dihedral angles.

Equation 16, which is an integral equation, relates the plane dihedral angle distribution to the true dihedral angles distribution. In order to solve equation 16, a numerical procedure is briefly outlined below.

The integral equation 16, can be discretized by considering discrete distributions of plane as well as true dihedral angles. Let both the distributions be divided into several classes. The integral equation 16 is converted into a set of simultaneous equations:

$$\begin{vmatrix} g_1 \\ g_2 \\ \vdots \\ g_j \\ \vdots \end{vmatrix} = \begin{vmatrix} p_{11} & p_{21} & \cdots & p_{i1} & \cdots \\ p_{12} & p_{22} & \cdots & p_{i2} & \cdots \\ \vdots & \vdots & & \vdots & \\ p_{1j} & p_{2j} & \cdots & p_{ij} & \cdots \\ \vdots & \vdots & & \vdots & \end{vmatrix} \begin{vmatrix} f_1 \\ f_2 \\ \vdots \\ f_i \\ \vdots \end{vmatrix} \quad (17)$$

where,  $g_j$  is the frequency of the  $j^{\text{th}}$  class of plane dihedral angles;  $f_i$  is the frequency of the  $i^{\text{th}}$  class of true dihedral angles; and  $p_{ij}$  is the probability of generating a plane dihedral angle in the  $j^{\text{th}}$  class from a true dihedral angle in the  $i^{\text{th}}$  class. A Monte-Carlo procedure has been developed for the estimation of the coefficients  $p_{ij}$ . Table 2.2 shows the values of the coefficients  $p_{ij}$  for various classes of  $\alpha$ . The first and last class intervals have been fixed to  $15^\circ$  and rests all were  $10^\circ$ . For different class widths, a new set of values for these coefficients has to be calculated. The frequency  $g_j$  can be determined by the measurement of plane dihedral angles on the polycrystalline microstructures. Now the frequency distribution of true dihedral angles can be calculated by solving the simultaneous equations given in relation 17 [Ref. 14].

**Table 2.2.** Computed values of the coefficients  $a_{ij}$ .

PDA	PDA distribution ( $a_{ij}$ ) for different value of TDA																
	7.5	20	30	40	50	60	70	80	90	100	110	120	130	140	150	160	172.5
0-15	0.91	0.26	0.09	0.05	0.02	0.01	0.01	0.01	0	0	0	0	0	0	0	0	0
15-25	0.08	0.55	0.25	0.11	0.05	0.03	0.02	0.01	0.01	0.01	0	0	0	0	0	0	0
25-35	0.01	0.13	0.42	0.2	0.1	0.07	0.03	0.03	0.01	0.01	0	0.01	0	0	0	0	0
35-45	0	0.03	0.14	0.37	0.2	0.1	0.06	0.03	0.02	0.01	0.01	0	0	0	0	0	0
45-55	0	0.01	0.05	0.14	0.35	0.18	0.08	0.05	0.03	0.02	0.01	0	0	0	0	0	0
55-65	0	0.01	0.02	0.06	0.14	0.32	0.15	0.08	0.04	0.03	0.01	0.01	0.01	0	0	0	0
65-75	0	0	0.01	0.03	0.05	0.13	0.32	0.16	0.09	0.05	0.03	0.01	0.01	0	0	0	0
75-85	0	0	0.01	0.01	0.03	0.06	0.14	0.31	0.14	0.07	0.05	0.02	0.01	0.01	0	0	0
85-95	0	0	0	0.01	0.01	0.04	0.07	0.14	0.29	0.14	0.06	0.04	0.02	0.01	0	0	0
95-105	0	0	0	0.01	0.01	0.03	0.03	0.07	0.15	0.29	0.15	0.06	0.03	0.02	0.01	0	0
105-115	0	0	0	0	0.01	0.01	0.03	0.04	0.08	0.15	0.31	0.13	0.05	0.02	0.01	0	0
115-125	0	0	0	0	0	0.01	0.02	0.03	0.04	0.09	0.16	0.33	0.14	0.06	0.02	0	0
125-135	0	0	0	0	0.01	0.01	0.01	0.02	0.03	0.05	0.09	0.18	0.36	0.14	0.05	0.01	0
135-145	0	0	0	0	0	0.01	0.01	0.01	0.03	0.04	0.06	0.08	0.18	0.4	0.13	0.03	0
145-155	0	0	0	0	0	0	0.01	0.01	0.01	0.02	0.03	0.06	0.1	0.21	0.45	0.13	0.01
155-165	0	0	0	0	0	0	0	0	0.01	0.01	0.02	0.03	0.05	0.09	0.21	0.56	0.06
165-180	0	0	0	0	0	0	0	0	0	0.01	0.01	0.01	0.03	0.04	0.1	0.26	0.92



## CHAPTER 3

# MATERIAL, MICROSCOPY AND IMAGE ANALYSIS

---

### 3.1: MATERIAL AND INITIAL TREATMENT

The chemical composition (both nominal as well as the detailed compositions) of the alloys (wt%) used in the present study are shown in **Table 3.1**.

**Table 3.1:** Chemical Composition of the Alloys

Alloy Nominal Composition	Detailed Weight Percent of the Alloying Elements						
	C	Si	Mn	P	S	Ni	Co
Ni-10% Co	0.006	<0.03	<0.03	0.005	0.003	88.40	11.15
Ni-20% Co	0.007	0.060	<0.03	0.005	0.003	76.90	22.85
Ni-30% Co	0.006	<0.03	<0.03	0.004	0.003	68.85	30.90
Ni-40% Co	0.006	0.030	<0.03	0.003	0.004	58.70	41.05
Ni-60% Co	0.006	0.060	<0.03	0.003	0.004	39.20	60.50

All the alloys were induction melted and cast under an argon atmosphere using virgin metals of purity greater than 99.99%. The ingots were cylindrical in shape having a height of about 20 mm. These ingots were cold rolled 50% to a thickness of 10 mm and then homogenisation annealed in vacuum at 1150°C for 24 hours. These were then again cold rolled 50% and annealed at 1150°C for a period of three hours to yield the starting material of almost random texture and a grain size of ~ 0.1 mm.

### 3.2: COLD ROLLING

Strips cut from the thick sheets were cold rolled in 2-high laboratory rolling mill where paraffin oil was used as lubricant. The ratio of the length of contact with the rolls to specimen thickness was maintained at a value greater than unity in order to get homogeneous deformation throughout the specimens. During rolling the strips were reversed after each pass and between two successive passes the strips were immersed in cold water to reduce the temperature rise due to deformation. Each alloy was rolled to 95% final reduction in thickness.

### 3.3: ANNEALING

After cold rolling the samples were annealed. Annealing was carried out in a Laboratory Tube type furnace. Each of the five samples of square shape was suspended with the help of wires inside the furnace. All samples were annealed at

800°C for seven different timings of 15 mins, 30 mins, 1 hour, 3 hour, 10 hours, 20 hours and 50 hours respectively in an Argon atmosphere. Gas was continuously passed through the furnace, and finally the samples were quenched in normal water.

### **3.4: TEXTURE MEASUREMENT**

Texture measurements were made on specimens taken from all the recrystallised samples. Specimens of the size (25 mm x 15 mm) were cut from the recrystallised material for this purpose. All the texture specimens were lacquered on one face and half of the thickness was removed from each of them chemically in a solution of 11% HF and 89% HNO<sub>3</sub>. All measurements were done on the mid-thickness plane of each sample. Four pole figures {111}, {200}, {220} and {311} were measured by the Schultz reflection method [Ref. 15] for each sample. From these data the ODF (Orientation distribution function) was determined, using the method of Bunge [Ref. 9]. Finally, modelling of each ODF was carried out using Gauss type functions for the different components and the volume fraction of each component was determined there from. [Ref. 16].

The texture measurements were carried out in the Institut für Metallkunde, Aachen in Germany.

### **3.5: OPTICAL MICROSCOPY**

The cold rolled samples were cold mounted for examination under the optical microscope. The samples for optical microscopy were ground and polished on emery papers (0 to 4 grades) followed by wet polish with alumina suspension of particle size 1µm and 0.03µm respectively. These were subsequently etched before examining the microstructure. The etching reagents used are:

- (a) 5 gm Ammonium Persulphate, 25 ml H<sub>2</sub>O.
- (b) 83 gm FeCl<sub>3</sub>, 33 ml. HCl.
- (c) 10 ml. HNO<sub>3</sub>.

Microstructures were observed on Lieca Optical Microscope for all the samples.

### **3.6: IMAGE PROCESSING ALGORITHM**

24 bit RGB digital images were acquired through a CCD camera mounted on Lieca Optical Microscope. These images were subsequently converted to 8-bit grayscale images. The size of the acquired image was 640X480 picture elements. A micro-scale was used to perform calibration of the image. At a magnification of 100X, dimension

of one pixel was calculated to be  $0.6041\ \mu\text{m}$ . The software used was Image-Pro Plus ver 4.1 for capturing as well as processing the images.

### **3.6.1: BINARIZATION/ THRESHOLDING**

A typical grayscale image of the microstructure of Ni-20%Co and the corresponding bimodal gray level distribution are shown in **Figure 3.1(a)** and **3.1(b)** respectively. For the binarization of such images, automatic thresholding was applied, which involved fixing the threshold limit at a minimum between two maxima of gray level distribution. All pixel values below the threshold limit were set to '0' value and those pixels whose value was above this limit were fixed to '255' value. This type of binarisation gave consistent results independent of image contrast and brightness [Ref. 17]. **Figure 3.2** shows the resulting binary image in which all the sensor noise and background illumination variation have been abstracted.

### **3.6.2: DILATION FILTERING**

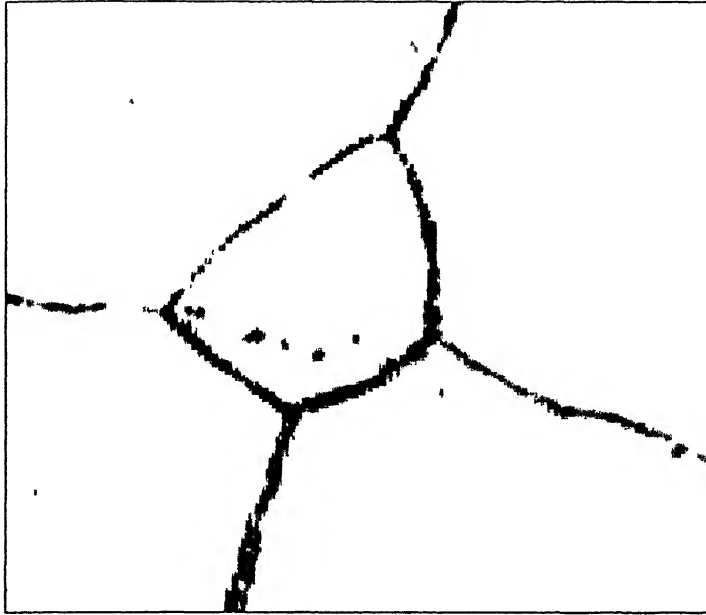
The dilation filter is a morphological filter that changes the size of an object in an image by dilating the specified objects. Actually it dilates bright objects, and erodes dark ones. The areas, which had to clean up, were selected as shown in **Figure 3.2** and then dilation filter was applied. Some narrow peninsulas or small particles are disappeared after dilation. This filter remove noise/artifacts created by etch pits, inhomogeneous etching/polishing etc. in the image as shown in **Figure 3.3**.

### **3.6.3: EROSION FILTERING**

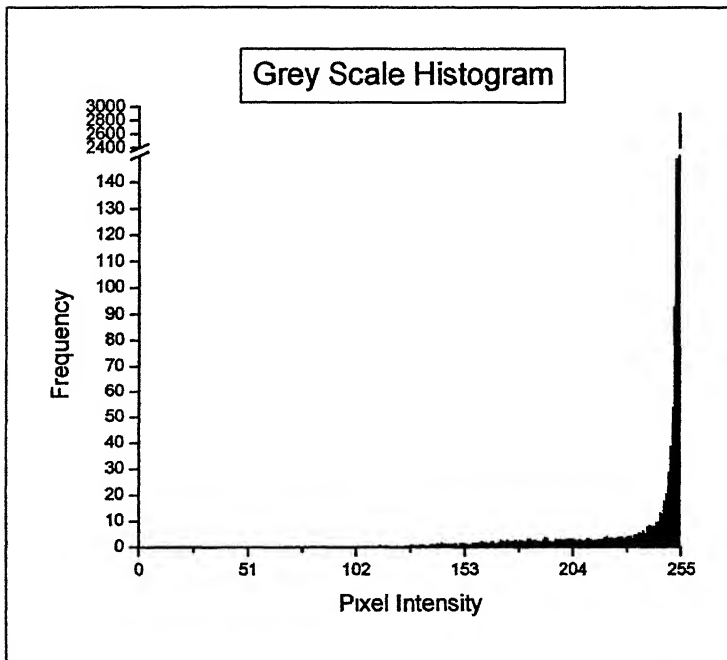
The erosion filter is also morphological filter that changes the size and shape of an object in an image by eroding or reducing the boundaries of the specified objects. It is a shrinking filter therefore eroded objects are smaller than the initial one. Basically the erosion filter erodes the edges of bright objects, and enlarges dark ones. After using this filter the discontinuity of the grain boundary is removed. This operation also resulted in the removal of some narrow peninsulas and small artifacts as shown in **Figure 3.4**.

### **3.6.4: THINNING MORPHOLOGICAL FILTER**

The eroded image is transformed by a thinning morphological operation to reduce the grain boundaries to only one pixel thick line. The thinning filter was applied iteratively till further operations of the filter had no effect on the image. The resulting thinned image is shown in **Figure 3.5**.



(a)



(b)

**Figure 3.1:** (a) A typical grayscale image of a polycrystalline microstructure, (b) Bimodal gray level histogram of the image (a).

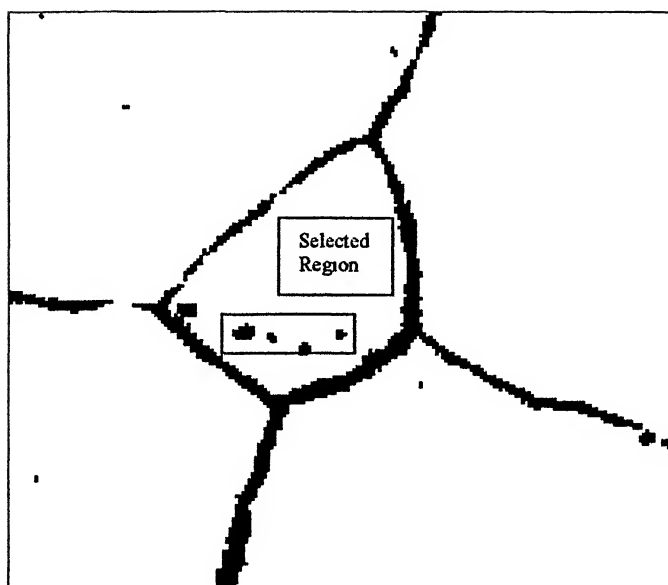


**Figure 3.2:** Transformed binary image (after applying thresholding algorithm) showing polishing/etching artifacts.

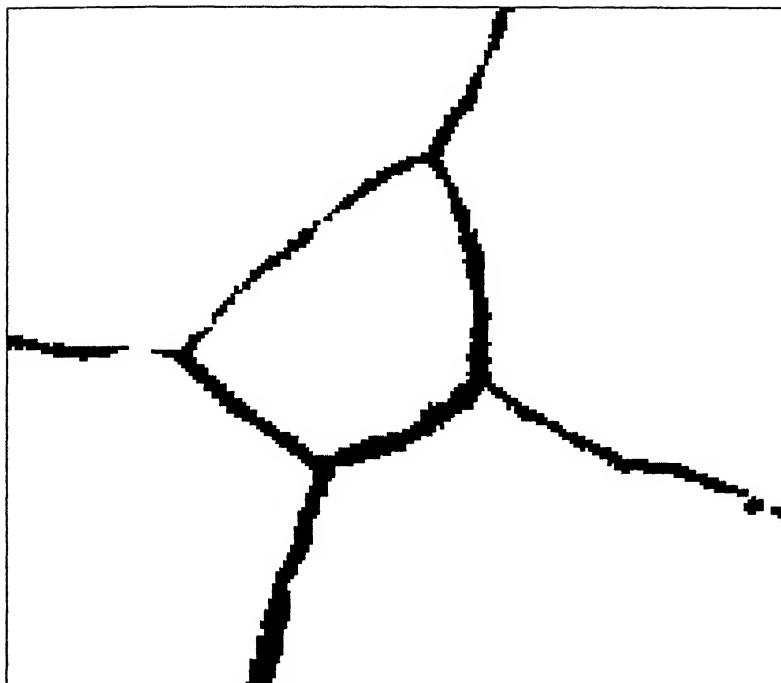


**Figure 3.3:** Result of applying dilation filter on Figure 3.2. The disappearance of peninsulas and etching artifacts is noticeable.

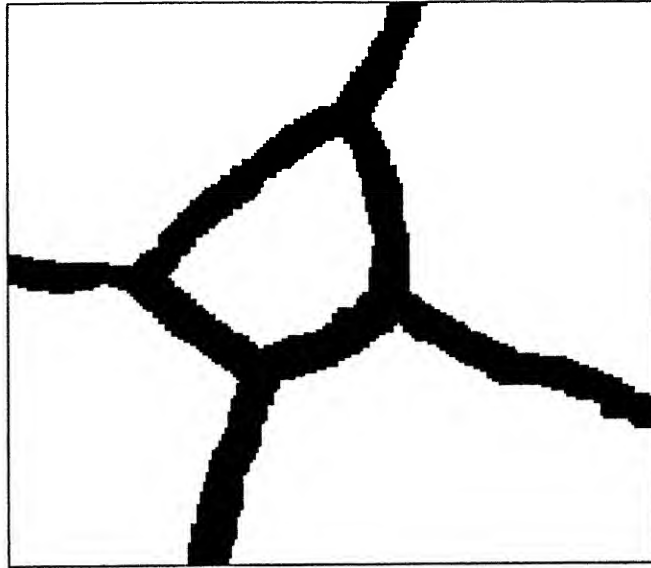


**Figure 3.4:** Image of microstructure obtained after erosion filter was applied on the image shown in Figure 3.3. It is noticeable here that the grain boundary has become continuous.

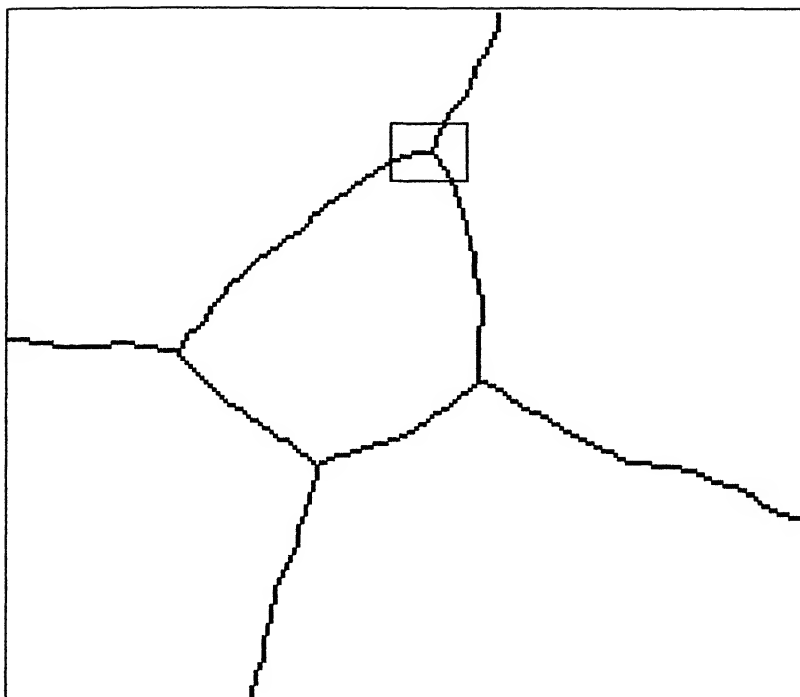


**Figure 3.5:** Image of the resultant microstructure after application of thinning filter on the image shown in Figure 3.4. The grain boundaries are now only one pixel thick.



### 3.6.5: BITMAPS

The final image was converted into a bitmap. **Figure 3.6** shows a bitmap of the rectangular region marked in **Figure 3.5**. As can be seen from this figure, the grain boundary pixels are represented by 0's and the matrix pixels are represented by 1's (these pixels uniquely had a value of 255 in the binary image). The bitmap was used as input to the algorithm developed to detect triple junctions and determine their geometry, as discussed below.

### 3.7: TRIPLE POINT DETECTION

Refer to the bitmap of the rectangular section of the image (**Figure 3.5**) of microstructure as seen in **Figure 3.6**. Each grain boundary pixel (pixel value of '0') was considered at the center of a 3x3 matrix. If a grain boundary pixel had exactly three other boundary pixels in its neighborhood then the pixel was marked as a possible triple point, and subjected to further evaluation by comparing it with a pre-generated list of valid triple point configurations. Partial lists of valid configurations in the form of 3x3 matrices are shown in **Figure 3.7**. The remaining configurations can be generated by rotating the individual matrices through  $\pi/2$ ,  $\pi$  and  $3\pi/2$  thereby generating a total of 12 valid configurations. However there are many other configurations possible in which the central '0' pixel has three neighboring pixels, but are not included in the above list. The reason for this becomes evident from **Figure 3.8**. The (row, column) coordinates of each pixel in the bitmap can be referred relative to the left-top pixel, whose coordinate is assigned (1,1), as shown in **Figure 3.8**. On examining this figure, it is clear that grain boundary pixels at coordinates (3,6), (3,7), (4,7) and (4,8) are not triple points even though each of these pixels have exactly three neighboring grain boundary pixels, such triple points have been termed as pseudo triple points [Ref. 18]. Similarly the grain boundary pixels at coordinates (3,4) and (4,3) are also pseudo triple points. However the triple point at coordinate (3,3) is an actual triple point, which matches with the configuration shown in **Figure 3.7a** rotated through  $\pi$ . Thus, the pseudo triple points can be classified according to the following general rule: If any two of the three neighboring pixels share a boundary among themselves, which means that if any two neighboring pixels have same 'x' coordinate and the 'y' coordinate differs by one and vice-versa then the triple point is classified as a pseudo triple point. This rule was found to be appropriate by comparing the results of the automated detection of triple points with manual detection.

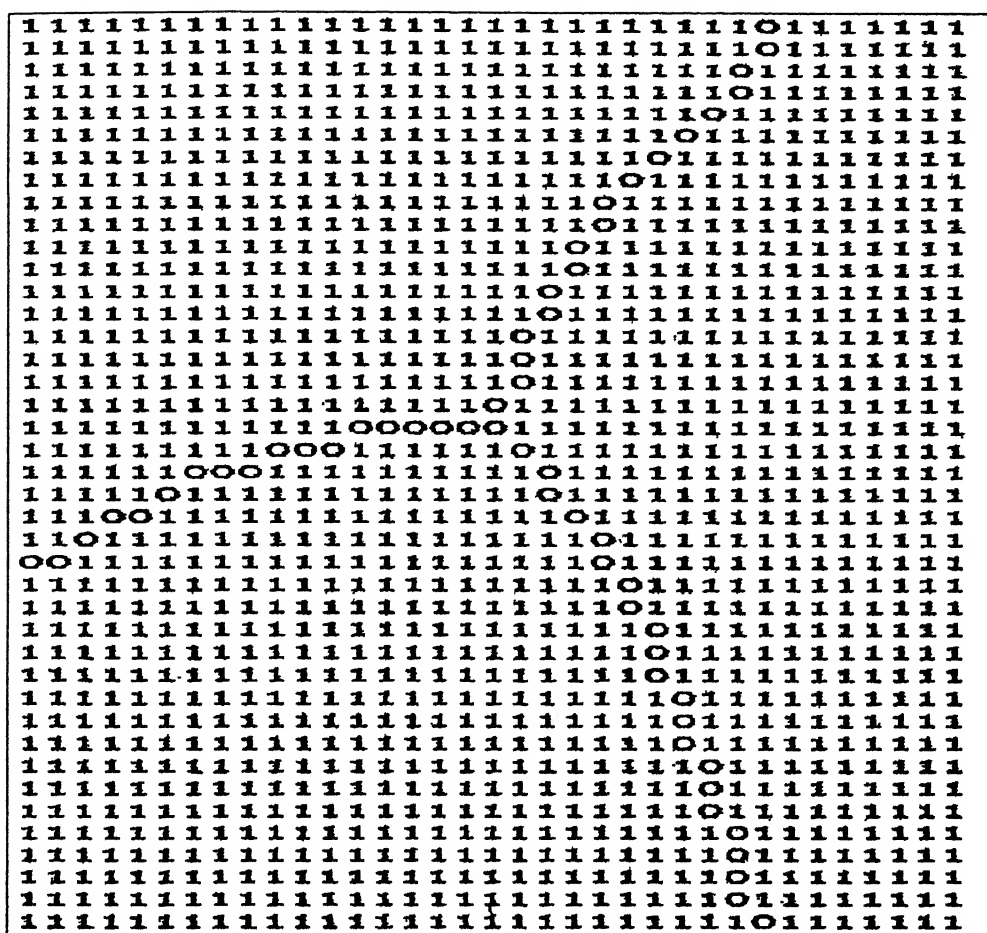


**Figure 3.6:** Bitmap of the marked rectangular region in Figure 3.5. '0' refers to grain boundary pixels and '1' refers to matrix pixels.

1	0	1
0	0	1
1	1	0

(a)

1	1	0
0	0	1
1	1	0

(b)

1	1	0
1	0	1
0	1	0

(c)

**Figure 3.7:** A partial configurations of valid triple points. Remaining configurations can be generated rotating the matrices through  $\pi/2$ ,  $\pi$  and  $3\pi/2$ .

	1	2	3	4	5	6	7	8	9	10
1	0	1	1	1	1	1	1	1	1	1
2	1	0	1	1	1	1	1	1	1	1
3	1	1	0	0	0	0	0	1	1	1
4	1	1	0	1	1	1	0	0	0	1
5	1	0	1	1	1	1	1	1	1	0
6	0	1	1	1	1	1	1	1	1	1

**Figure 3.8:** Illustration of pseudo triple points.

### 3.8: EVALUATION OF PLANE DIHEDRAL ANGLES (PDA)

After detecting triple points, as described in section 3.7, the coordinates of the pixels of the grain boundary segments were traced till the segment terminated into another triple point or till no further touching pixels could be found. The algorithm developed for the same is at appendix A.1. At this stage, if a particular segment was found to be very short (less than four pixel length) then the associated triple point was considered as a pseudo-triple point and therefore eliminated from the analysis. Manual examination of the microstructure confirmed the validity of this procedure.

A least square procedure was employed to fit polynomials on the pixels of the grain boundary segments at each triple point. The form of the polynomial chosen for the purpose is given as:

$$y = a_0 + a_1x + a_2x^2 + \dots + a_mx^m \quad (3.1)$$

where 'm' is the polynomial order,  $a_1, a_2, \dots, a_m$  are the coefficients. This form of the polynomial was modified to ensure that the fitted curve is constrained to pass through the triple point.

A least square procedure was adopted to determine the values of the polynomial coefficients. This involved minimization of the sum of square ( $R^2$ ) of the following equation:

$$R^2 = \sum_{i=1}^n [y_i - y]^2 \quad (3.2)$$

where,  $y_i$  is the measured value and  $y$  is given by equation (3.1) for the  $i$ th pixel. Derivative of equation (3.2) with respect to each of the unknown coefficients of the polynomial is performed and equated to zero to develop a set of equations, which was solved by gauss-elimination technique.

Each grain boundary segment was fitted with polynomial of increasing degree of order, starting with the order of 1. In order to select the best polynomial order, a ratio  $F$  was evaluated to compare the goodness-of-fit (quantified by sum of squares,  $R^2$ ) of two polynomials of orders  $m$  and  $m+1$

$$F = \frac{(R_1^2 - R_2^2) / R_1^2}{(\gamma_1 - \gamma_2) / \gamma_1} \quad (3.3a)$$

and

$$\gamma_1 = n - (m + 1) \quad \text{and} \quad \gamma_2 = n - (m + 2) \quad (3.3b)$$

where,  $\gamma$  = degree of freedom,  $n$  = number of data points and the subscripts 1 and 2 refer to the polynomials of orders  $m$  and  $m+1$  respectively.

If the fit of the higher order polynomial (order =  $m+1$ ) has a larger sum of squares, i.e.,  $R_2^2 > R_1^2$ , then clearly the fit becomes worse on increasing the order and therefore, the lower order polynomial (order =  $m$ ) is chosen as the best order. In terms of the F-ratio (equation 3.3a), the value of  $F$  will be negative. However, in general with increasing polynomial order the sum of square value is expected to reduce because the higher order equation has more adjustable parameters. Thus, a further analysis of the F-ratio was done.

In going from lower order to the higher order polynomial, if the relative decrease in the sum-of-squares was less than the relative decrease in the degree of freedom (i.e.,  $F \leq 1$ ), then the polynomial with the lower order was selected as the best polynomial order. On the other hand, if the value of  $F$  was greater than 1, i.e., the relative decrease in the sum of squares was larger than the relative decrease in the degree of freedom, then the higher polynomial order was accepted and the above analysis was repeated by further incrementing the polynomial order.

The correlation coefficient,  $r$ , for each polynomial fit was determined by using the following equation:

$$r^2 = \frac{S^2 - R^2}{S^2} \quad (3.4)$$

$$\text{where, } S^2 = \sum_{i=1}^n (y_i - \bar{y})^2 .$$

For a perfect fit  $R^2 = 0$  and  $r^2 = 1$ , signifying that the polynomial fit truly fits all the coordinates of each grain boundary. While  $r^2$  close to zero signifies a poor fit. The correlation coefficient was used to decide whether to accept or reject a particular fit, as discussed in the section.

The plane dihedral angles were determined as the angles between the tangents to the grain boundary segments at the triple points. Figure 3.9 illustrates a typical example of three tangent lines (calculated by differentiating the fitted curves) at a triple point. Plane dihedral angle,  $\beta$ , is given by

$$\cos \beta = \frac{(OA)^2 + (OB)^2 - (AB)^2}{2(OA)(OB)} \quad (3.5)$$

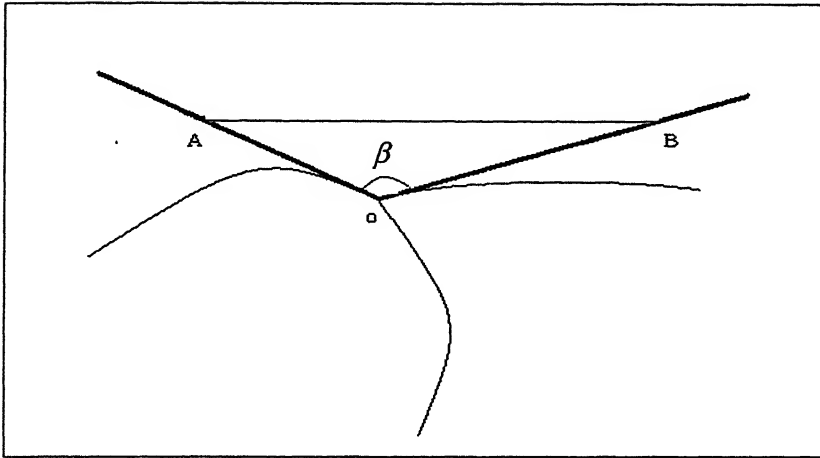


**Figure 3.9:** Tangents (thick lines) drawn to the fitted grain boundary segments (thin lines) at a triple point 'O'. 'A' and 'B' are arbitrary points on the segments.

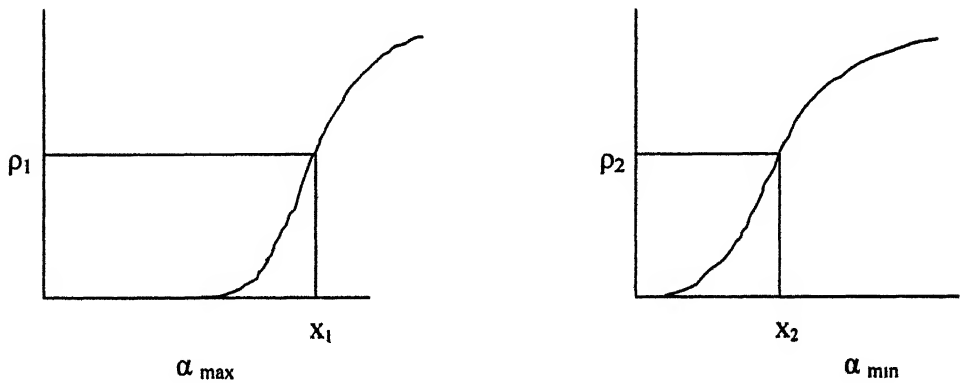


**Figure 3.10:** Schematic of cumulative distribution for true dihedral angles:

(a)  $\alpha_{\max}$ , (b)  $\alpha_{\min}$ .  $\rho_1$  and  $\rho_2$  are randomly generated number.  $x_1$  and  $x_2$  are corresponding  $\alpha_{\max}$  and  $\alpha_{\min}$

Similarly, the other two plane dihedral angles can also be determined.

After calculating the plane dihedral angles of each triple point the maximum and minimum plane dihedral angles of each triple points were evaluated. To find out the distribution of plane dihedral angles 17 small classes were considered over an angular range of 0° to 180°. The first and last class intervals were 15° and rests all were 10°. Then the frequency of each class was calculated for both maximum and minimum plane dihedral angles. Subsequently the relative frequencies were computed for both.

### 3.9: TRANSFORMATION OF PDA DISTRIBUTION TO TDA DISTRIBUTION

The relative frequencies of plane dihedral angles (both maximum and minimum) were transformed to true dihedral angles by the methods as described in section 2.11 with the help of computer program. The minimum and maximum relative frequencies of true dihedral angles were denoted as  $\alpha_{\min}$  and  $\alpha_{\max}$  respectively. For transformation the values of coefficients  $a_{ij}$  were used as mentioned in Table 2.2.

### 3.10: RELATIVE GRAIN BOUNDARY ENERGIES

The relative grain boundary energy was calculated in terms of two parameters:

$$\frac{\gamma_1}{\gamma_3} = \frac{\sin \alpha_1}{\sin \alpha_3} \quad (3.6)$$

$$\frac{\gamma_2}{\gamma_3} = \frac{\sin \alpha_2}{\sin \alpha_3} \quad (3.7)$$

where  $\gamma_1 < \gamma_2 < \gamma_3$  are the energies of grain boundary planes meeting at a triple edge. In order to calculate above, joint distribution of  $\alpha_{\min}$ ,  $\alpha_{\max}$  was computed using a Monte-

Carlo procedure. For this the calculated cumulative distributions of  $\alpha_{\min}$ ,  $\alpha_{\max}$  were taken, as schematically shown in Figure 3.10(a) and (b).

The Monte-Carlo procedure involved generation of a pair of uniformly distributed random numbers (in the range: 0 to 1) at each iteration. Let a pair of such numbers be  $\rho_1$  and  $\rho_2$ . For each  $\rho_1$  and  $\rho_2$  the corresponding  $x_1$  and  $x_2$  could easily be found out.  $\gamma_1$ ,  $\gamma_2$  and  $\gamma_3$  were then computed from equation 3.6 and 3.7. 5000 iteration was done from which we obtained the distribution of both  $\gamma_1/\gamma_3$  and  $\gamma_2/\gamma_3$ . The relative frequencies of  $\gamma_1/\gamma_3$  and  $\gamma_2/\gamma_3$  were evaluated subsequently. The whole process was done with the help of computer program as mention in appendix A.7.

### RESULTS AND ANALYSIS

---

As mentioned in chapter 3, the five Ni-Co alloys i.e. Ni-10%Co, Ni-20%Co, Ni-30%Co, Ni-40% Co and Ni-60%Co were cold rolled by an amount of 95% reduction to approximately 0.25 mm thickness. In order that homogeneous deformation throughout the specimens might be achieved, the ratio of the length of contact with rolls to specimen thickness was maintained at a value greater than unity. To produce recrystallisation texture the cold rolled samples were annealed at 800°C for seven different times of 15 minutes, 30 minutes, 1 hour, 3 hours, 10 hours, 20 hours and 50 hours respectively.

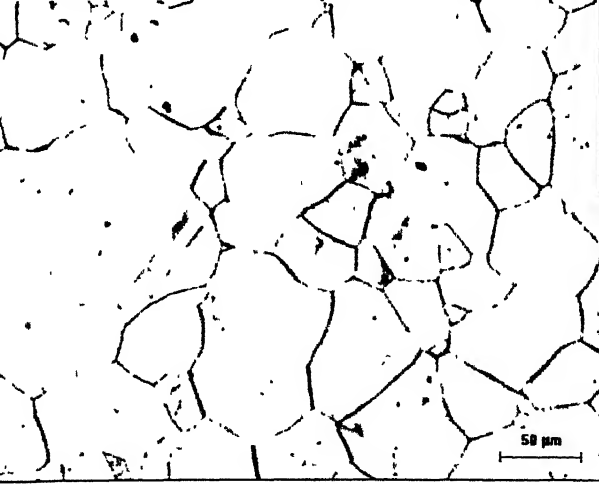
#### 4.1: OPTICAL MICROSCOPY

The optical microstructures of annealed samples of all the five alloys are shown in **Figure 4.1 to Figure 4.7**. In general all the samples showed almost full recrystallisation from the shortest annealing time of 15 minutes. Grain growth was also observed in the samples. Annealing twins can also be observed in almost all the samples. Each microstructure as developed in the normal manner was further processed with the help of an Image Analyser as discussed in chapter 3. Some typical processed microstructures are shown in **Figure 4.8 and 4.9**. The processed microstructures appear far more clear as compared to the unprocessed microstructures indicating very clearly the grain boundaries and triple points. The important thing to be noticed is that the twin boundary areas were eliminated from the processed structure. The polishing/etching artefacts were also removed. After processing the grain boundary regions were one pixel thick which made it easier to determine the plane dihedral angles. For each sample nearly 150 triple points were considered from which plane dihedral angles were determined. The plane dihedral angle distributions were converted to true dihedral angle distributions and subsequently relative grain boundary energy ratios were evaluated, in the manner described in chapter 3.

#### 4.2: RELATIVE GRAIN BOUNDARY ENERGY

The relative grain boundary energy ratios, both  $\gamma_1/\gamma_3$  and  $\gamma_2/\gamma_3$  were calculated by the method described in chapter 3 where  $\gamma_1 < \gamma_2 < \gamma_3$ . The frequency distributions of these values have been plotted against the values of these ratios for all the samples concerned, in different manners to arrive at meaningful conclusions.

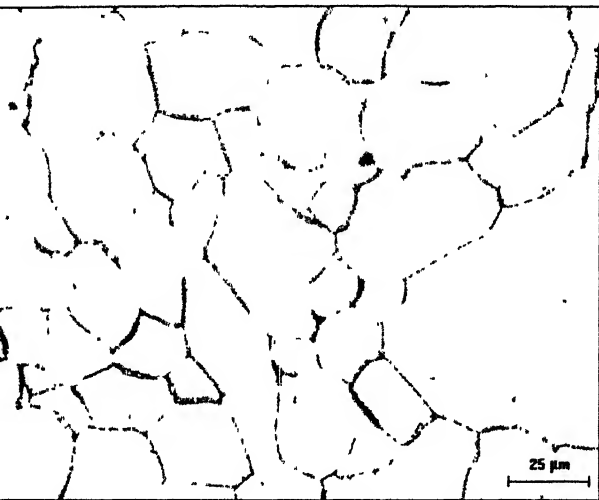




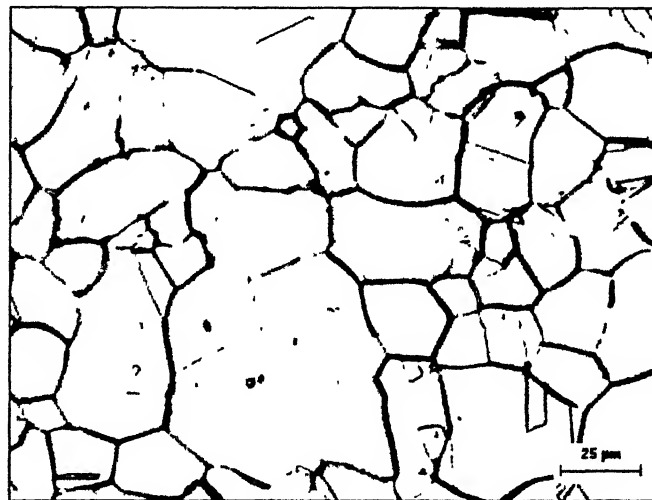
(a) Ni-10% Co



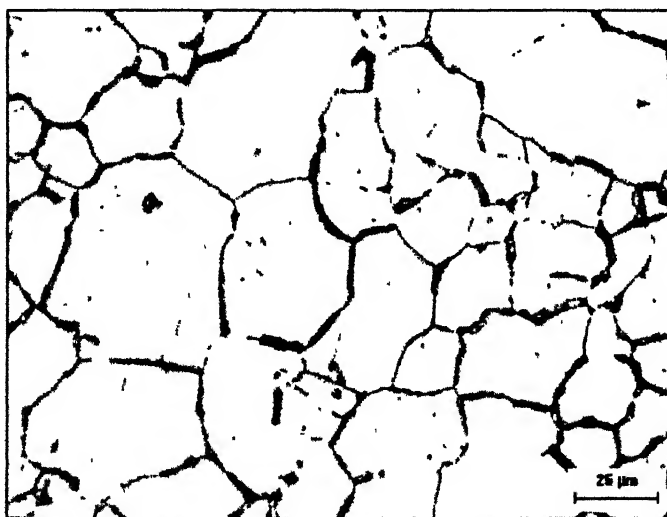
(b) Ni-20% Co



(c) Ni-30% Co

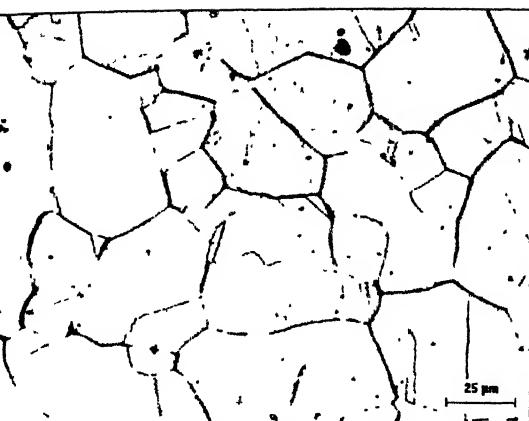


(d) Ni-40% Co

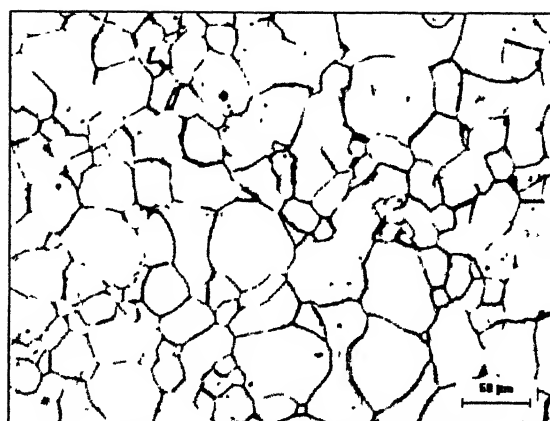


(e) Ni-60% Co

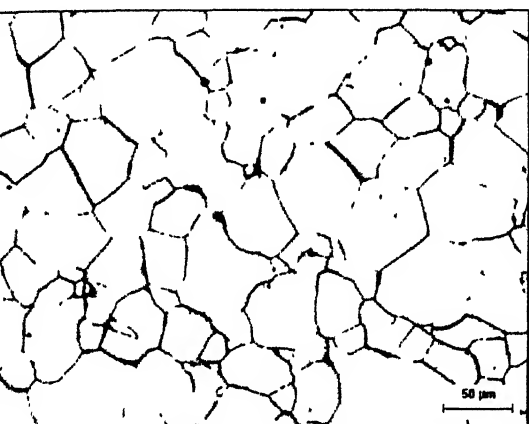
**Figure 4.1:** Micrographs of different Ni-Co alloys annealed for 15 minutes.



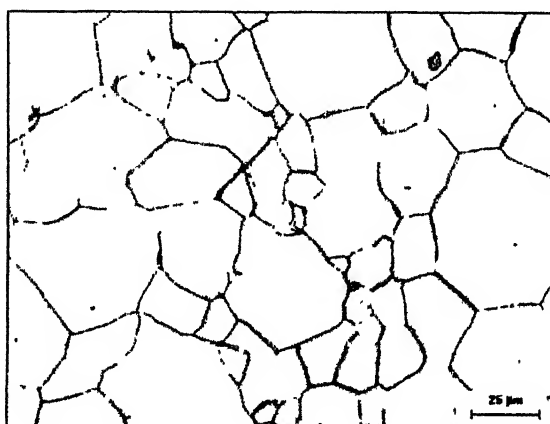
(a) Ni-10% Co



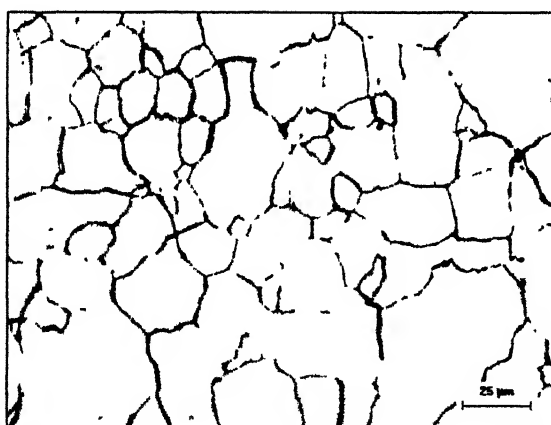
(b) Ni-20% Co



(c) Ni-30% Co

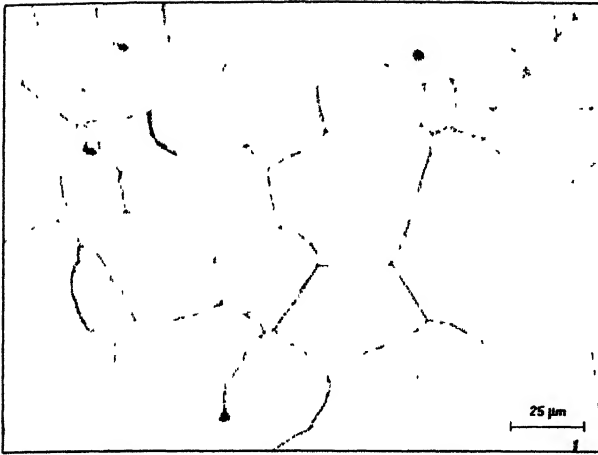


(d) Ni-40% Co

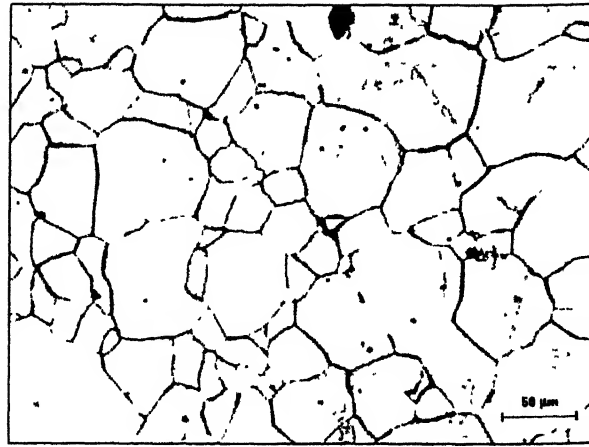


(e) Ni-60% Co

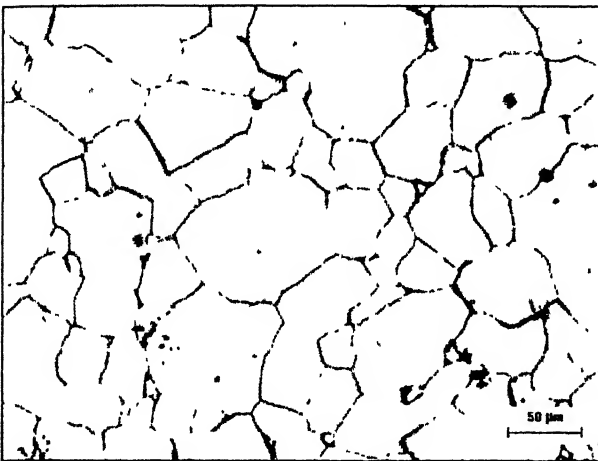
**Figure 4.2:** Micrographs of different Ni-Co alloys annealed for 30 minutes.



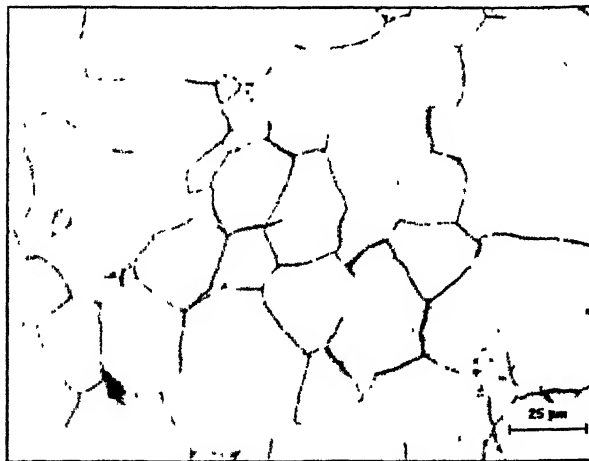
(a) Ni-10% Co



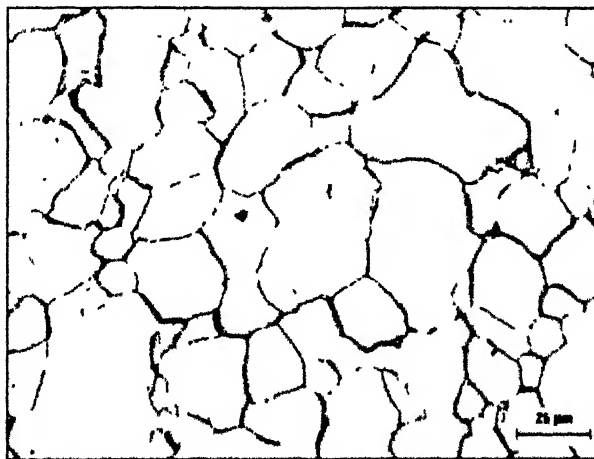
(b) Ni-20% Co



(c) Ni-30% Co



(d) Ni-40% Co

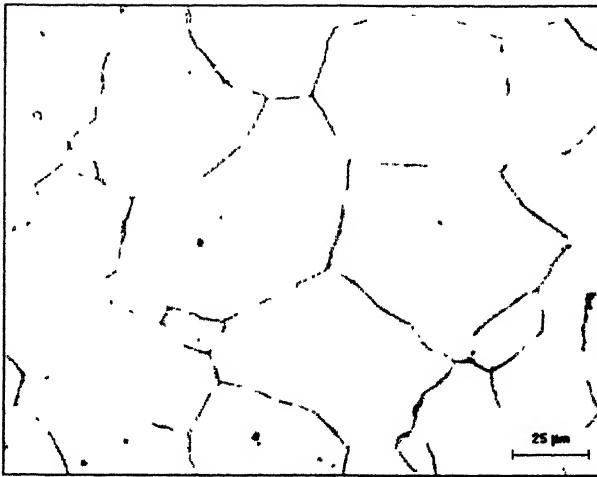


(e) Ni-60% Co

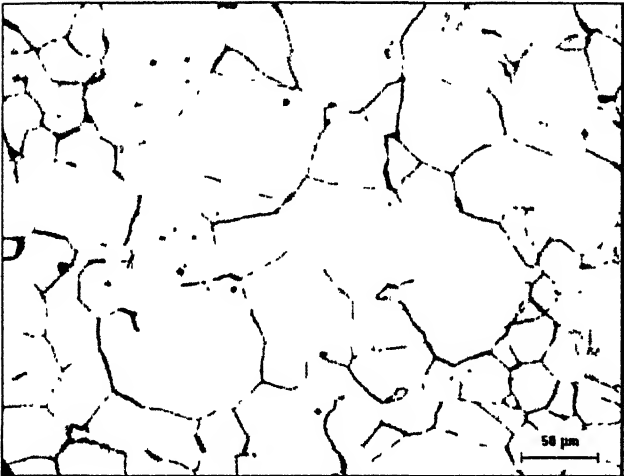
**Figure 4.3:** Micrographs of different Ni-Co alloys annealed for 1 hour.



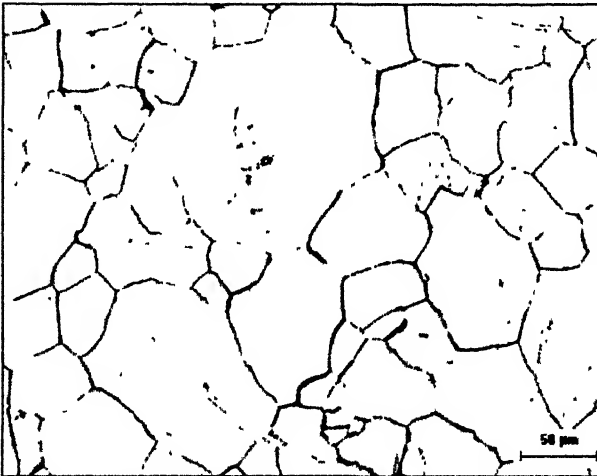
(a) Ni-10% Co



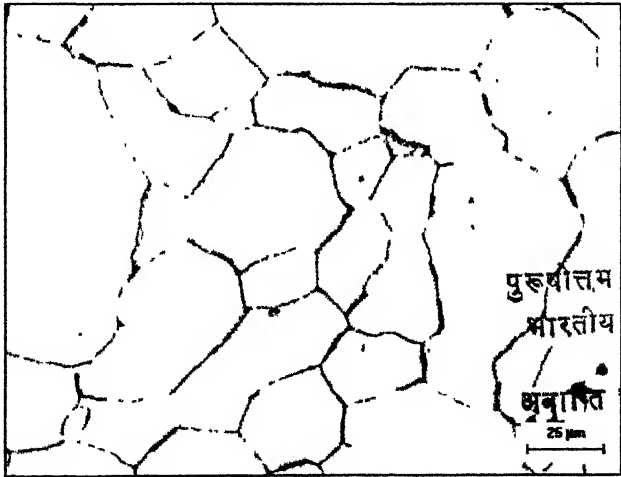
(b) Ni-20% Co



(c) Ni-30% Co

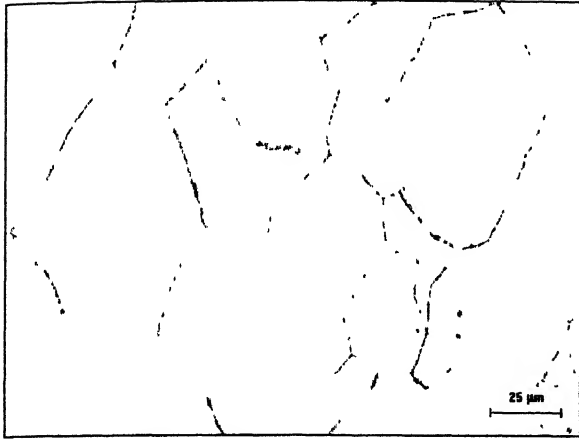


(d) Ni-40% Co

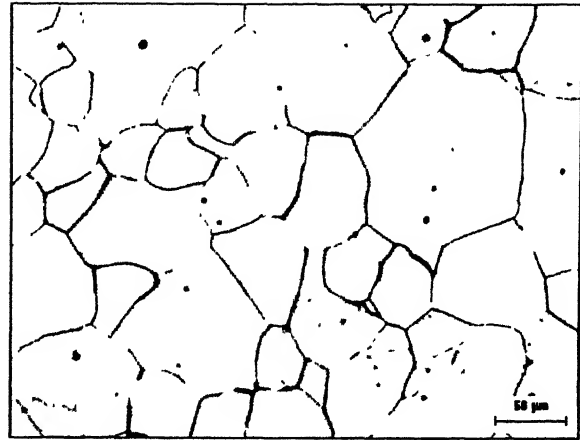


(e) Ni-60% Co

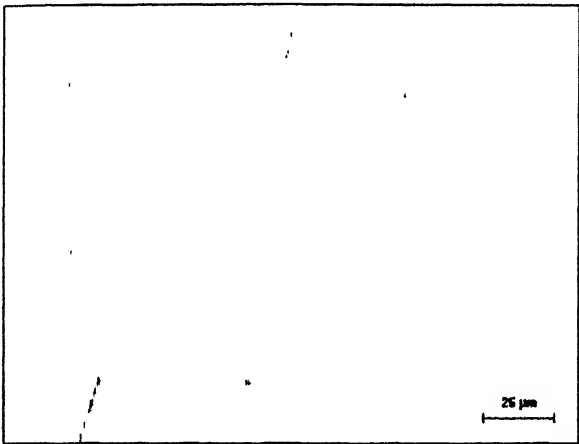
**Figure 4.4:** Micrographs of different Ni-Co alloys annealed for 3 hours.



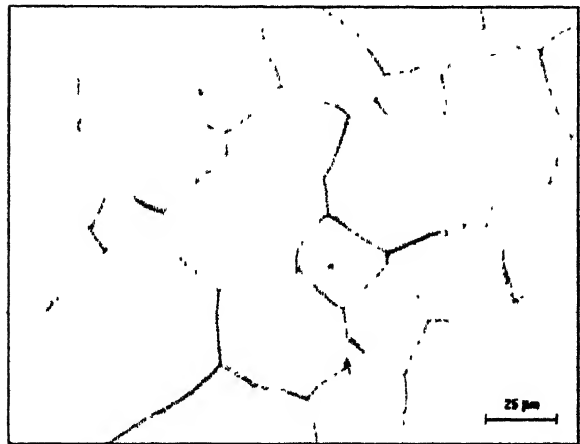
(a) Ni-10% Co



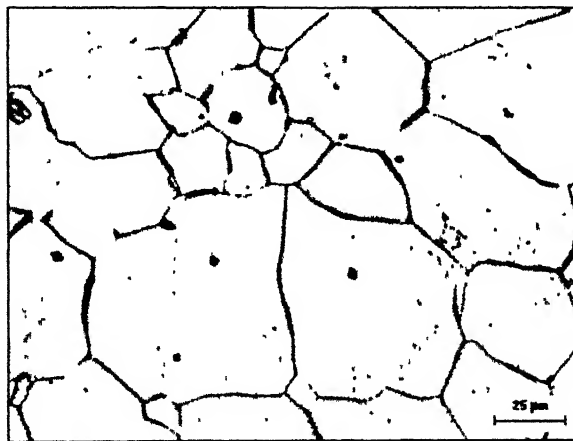
(b) Ni-20% Co



(c) Ni-30% Co

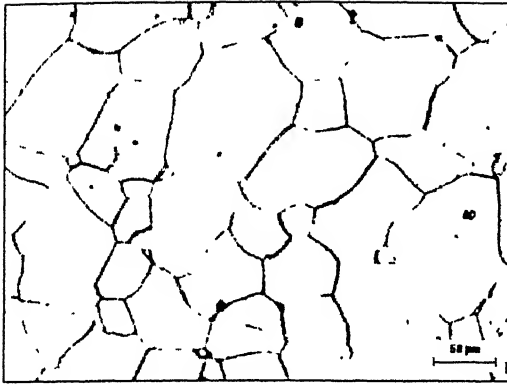


(d) Ni-40% Co

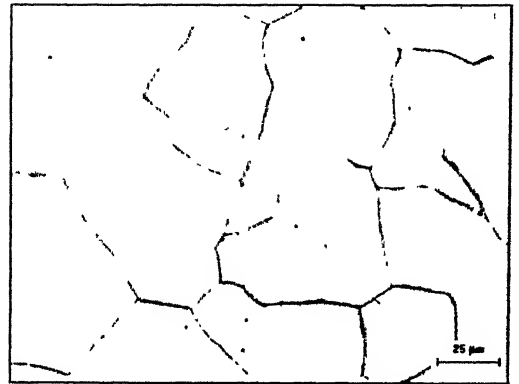


(e) Ni-60% Co

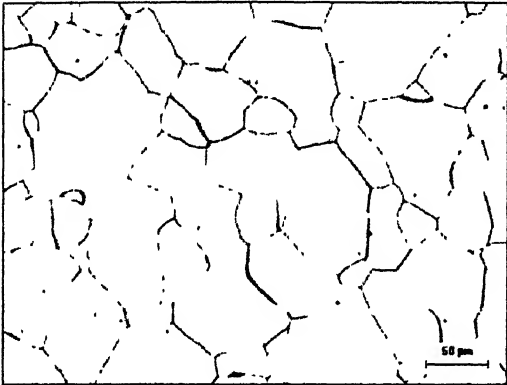
**Figure 4.5:** Micrographs of different Ni-Co alloys annealed for 10 hours.



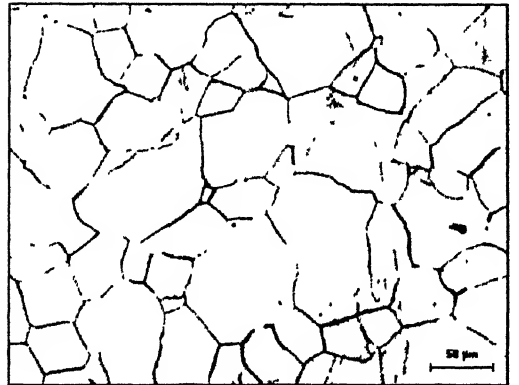
(a) Ni-10% Co



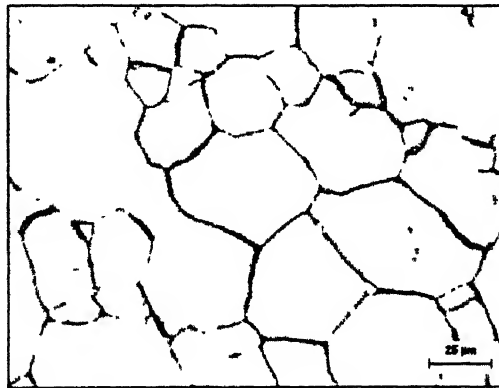
(b) Ni-20% Co



(c) Ni-30% Co

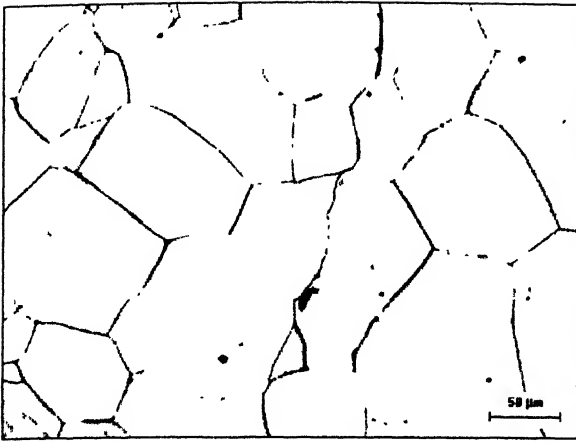


(d) Ni-40% Co

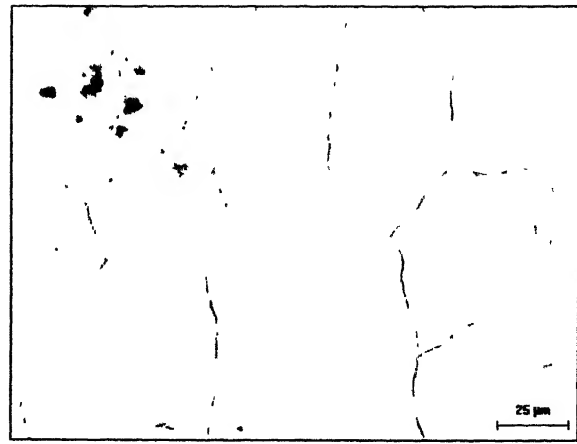


(e) Ni-60% Co

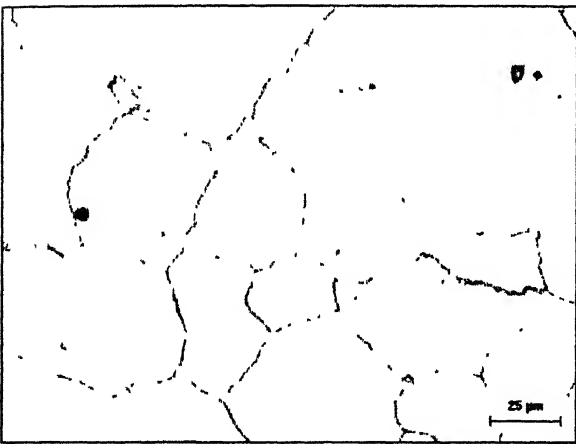
**Figure 4.6:** Micrographs of different Ni-Co alloys annealed for 20 hours.



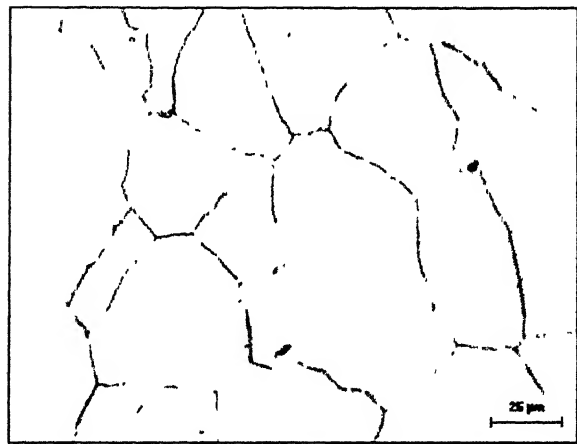
(a) Ni-10% Co



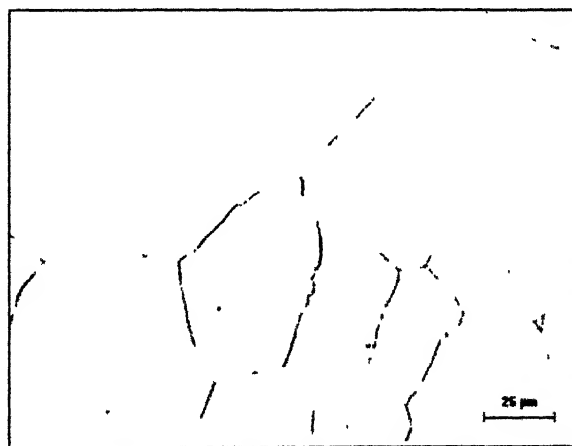
(b) Ni-20% Co



(c) Ni-30% Co

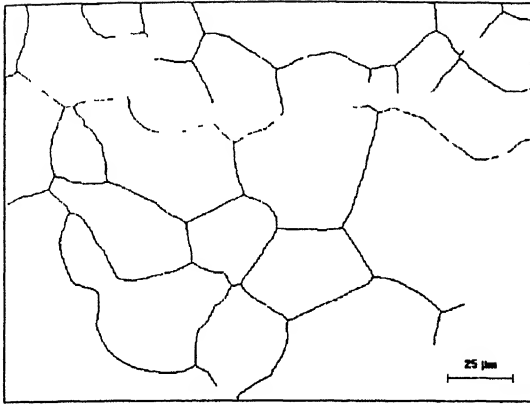


(d) Ni-40% Co

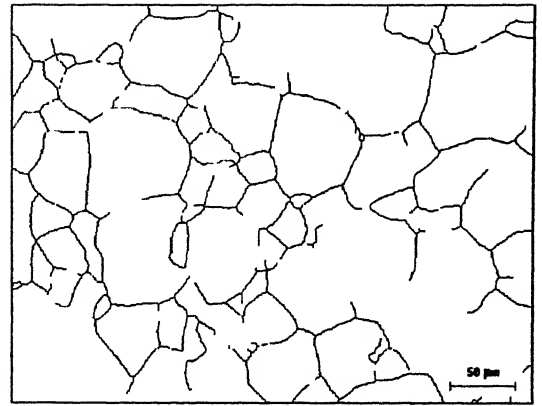


(e) Ni-60% Co

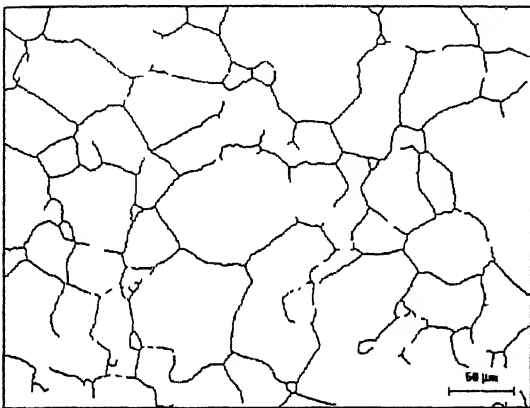
**Figure 4.7:** Micrographs of different Ni-Co alloys annealed for 50 hours.



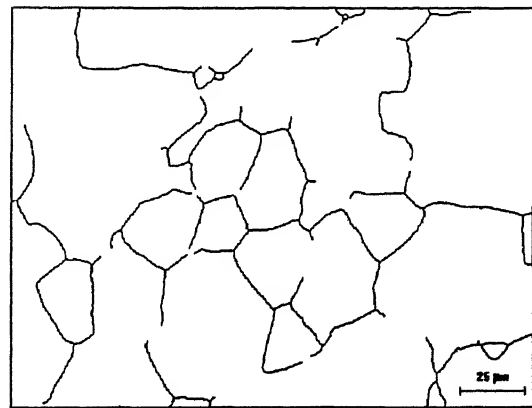
(a) Ni-10% Co



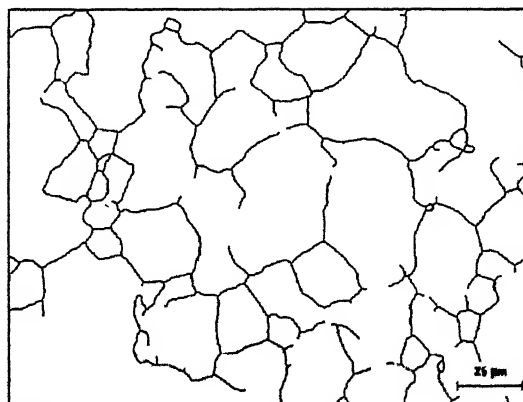
(b) Ni-20% Co



(c) Ni-30% Co



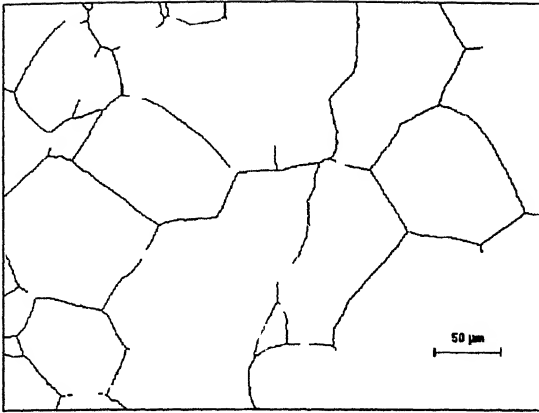
(d) Ni-40% Co



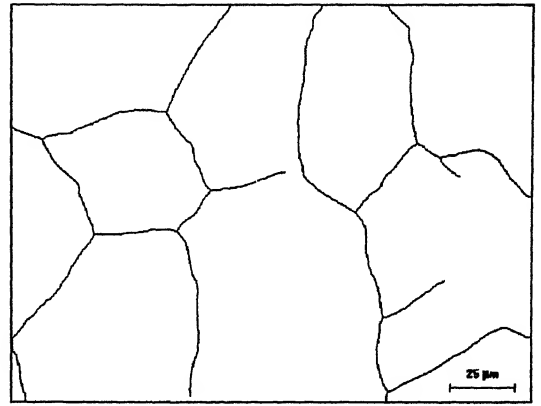
(e) Ni-60% Co

**Figure 4.8:** Micrographs showing processed structure of different Ni-Co alloys annealed for 1 hour.

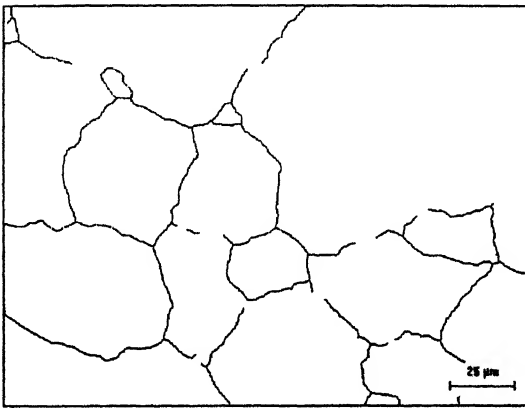




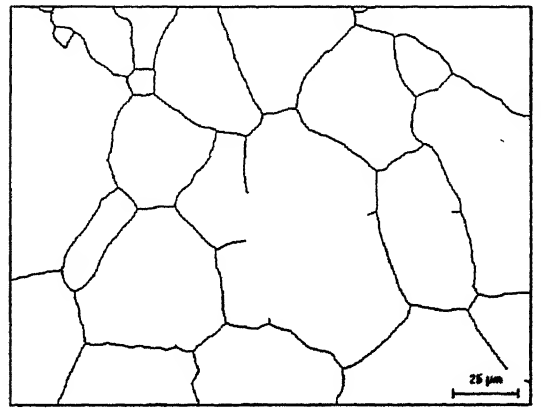
(a) Ni-10% Co



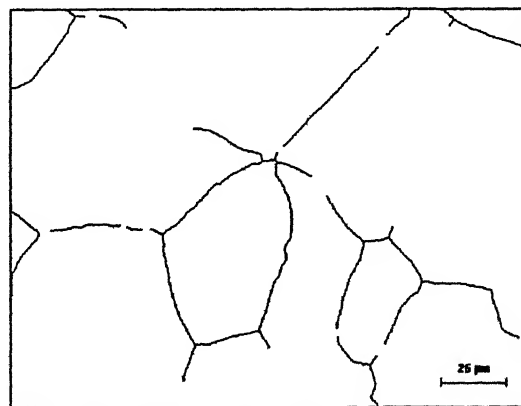
(b) Ni-20% Co



(c) Ni-30% Co



(d) Ni-40% Co



(e) Ni-60% Co

**Figure 4.9:** Micrographs showing processed structure of different Ni-Co alloy annealed for 50 hours.

## 4.2.1: HISTOGRAMS

### 4.2.1.1: HISTOGRAMS OF FREQUENCY vs. $\gamma_1/\gamma_3$

The histograms of frequency vs. relative grain boundary energy ratio  $\gamma_1/\gamma_3$  are shown in **Figures 4.10 to 4.16**. It is observed from the histograms that the relative grain boundary energy ratio with a class width of 0.6 to 0.7 and 0.7 to 0.8 always possess higher frequency compared to others. Relative grain boundary energy ratios with a value greater than 0.9 are never obtained in any of the samples.

### 4.2.1.2: HISTOGRAMS OF FREQUENCY vs. $\gamma_2/\gamma_3$

The histograms of frequency vs. relative grain boundary energy ratio  $\gamma_2/\gamma_3$  are shown in **Figure 4.17 to 4.23**. In contrast to the histograms of frequency vs.  $\gamma_1/\gamma_3$ , in this case the  $\gamma_2/\gamma_3$  ratios always possess values higher than 0.6. The frequency of  $\gamma_2/\gamma_3$  ratios with a value less than 0.6 is practically zero. This has been observed in all the samples. To be precise, the  $\gamma_2/\gamma_3$  ratios have minimum frequencies in the class width of 0.6 to 0.7. That means  $\gamma_2/\gamma_3$  ratios of values higher than 0.7 have higher frequencies compared to others. The frequency of  $\gamma_2/\gamma_3$  ratio with a class width of 0.9 to 1 is maximum for majority of the cases.

## 4.2.2: FREQUENCY DISTRIBUTION OF RELATIVE GRAIN BOUNDARY ENERGY RATIO

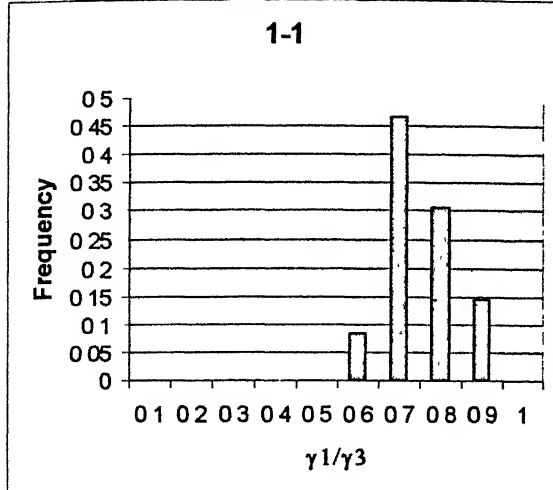
All the relevant data that were used to determine the histograms were plotted in a graphical form for simplicity and for ease in comparison.

### 4.2.2.1: FREQUENCY DISTRIBUTION OF $\gamma_1/\gamma_3$

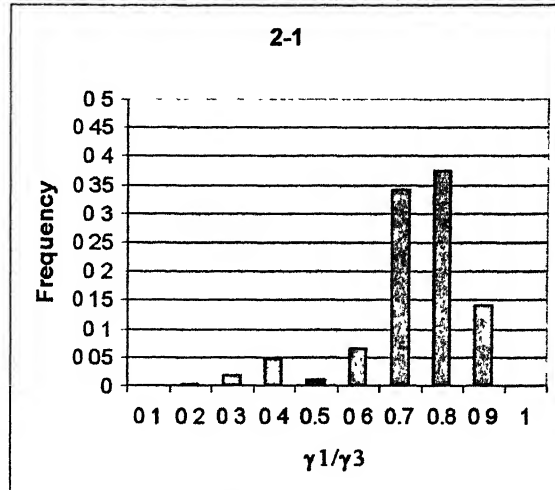
The frequency distribution of  $\gamma_1/\gamma_3$  ratio for various annealing times are shown in **Figure 4.24 to 4.28**. Upto certain value of  $\gamma_1/\gamma_3$  ratio, there is no significant difference in frequency. This trend changes from around 0.2 (value of  $\gamma_1/\gamma_3$  ratio), after which there is a continuous increase in frequency. The peaks are distributed in the region 0.6 to 0.8. After attaining the peak value there is a drastic decrease in frequency and at  $\gamma_1/\gamma_3$  ratio of 1 the frequency is zero. This is quite obvious because  $\gamma_1$  and  $\gamma_3$  will never have the same value except under perfect equilibrium condition.

### 4.2.2.2: FREQUENCY DISTRIBUTION OF $\gamma_2/\gamma_3$

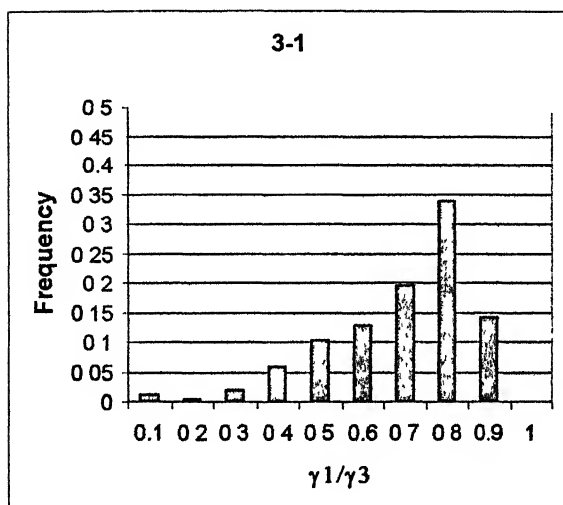
The frequency distribution of  $\gamma_2/\gamma_3$  ratio for various annealing time are shown in **Figure 4.29 to 4.33**. For all the alloys the graphs show similar trends. Upto the  $\gamma_2/\gamma_3$  ratio of 0.6 the frequency is zero irrespective of different alloys and annealing times.



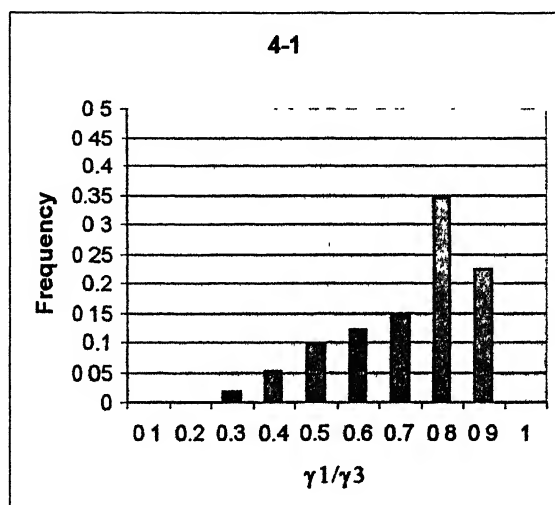
(a) Ni-10% Co



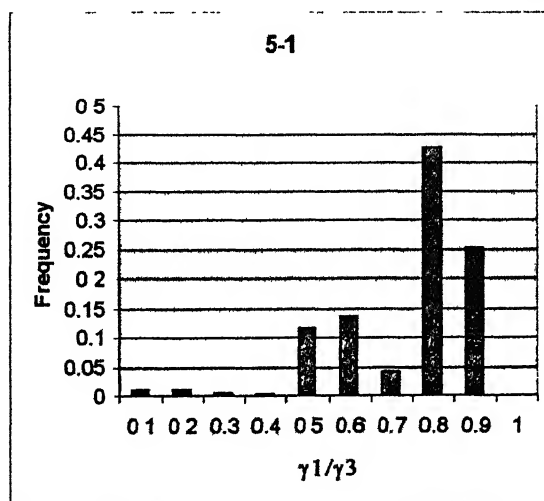
(b) Ni-20% Co



(c) Ni-30% Co

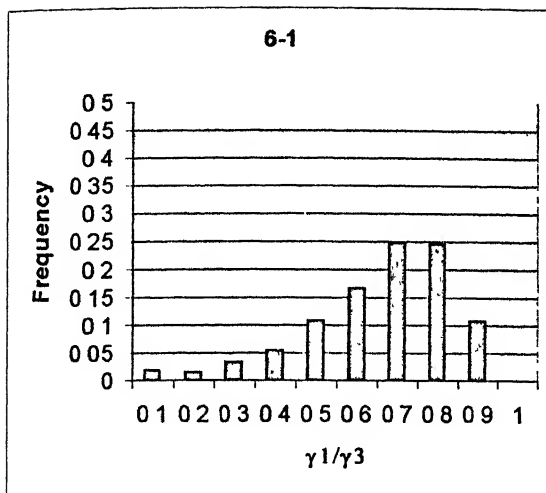


(d) Ni-40% Co

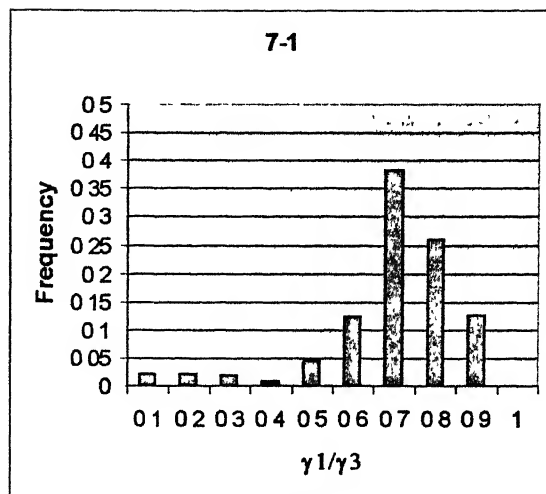


(e) Ni-60% Co

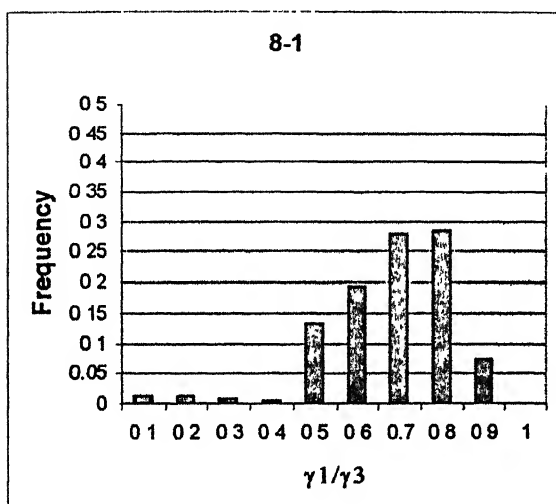
**Figure 4.10:** Frequency distribution of relative energy ratio  $\gamma_1/\gamma_3$  of different Ni-Co alloys annealed for 15 minutes.



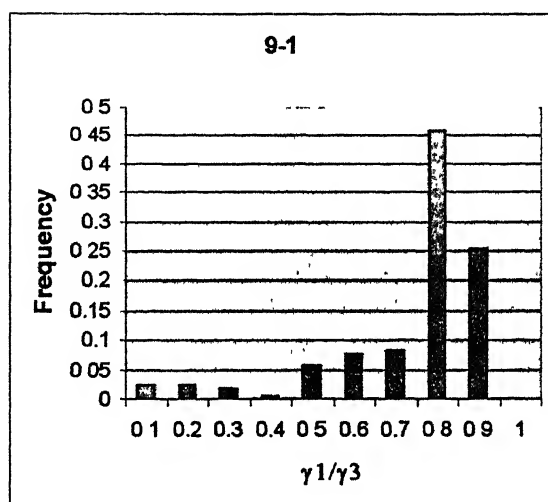
(a) Ni-10% Co



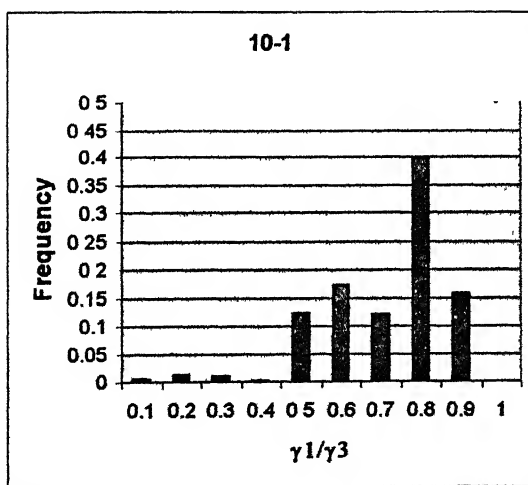
(b) Ni-20% Co



(c) Ni-30% Co



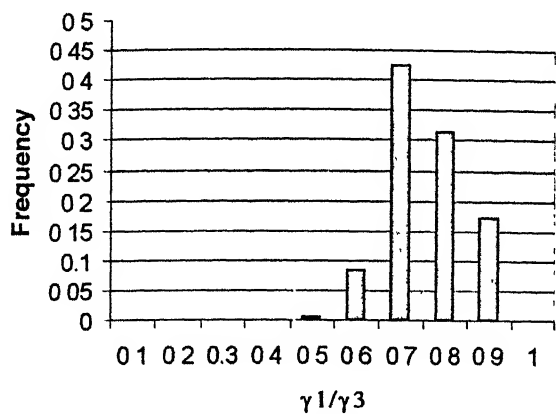
(d) Ni-40% Co



(e) Ni-60% Co

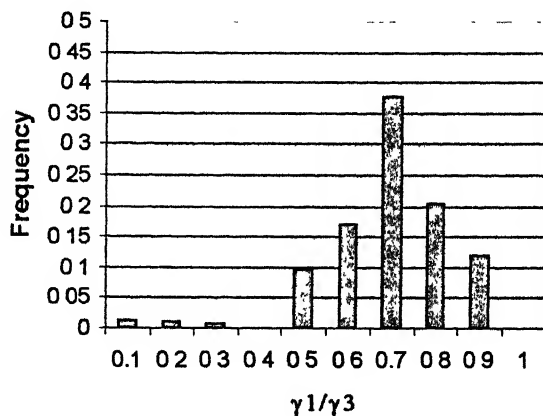
**Figure 4.11:** Frequency distribution of relative energy ratio  $\gamma_1/\gamma_3$  of different Ni-Co alloys annealed for 30 minutes.

11-1



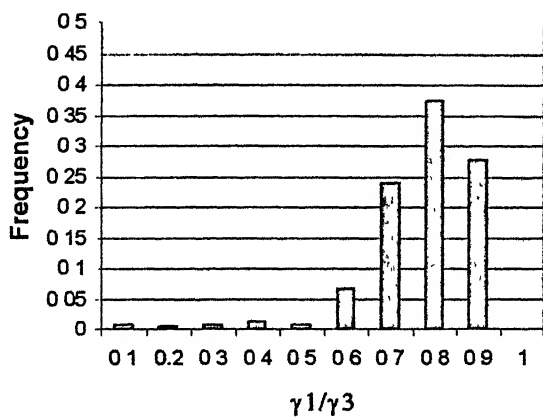
(a) Ni-10 % Co

12-1



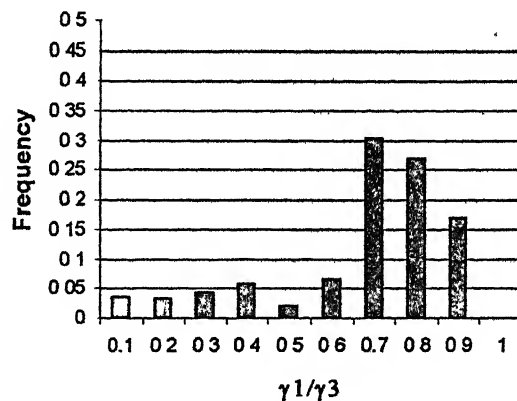
(b) Ni-20% Co

13-1



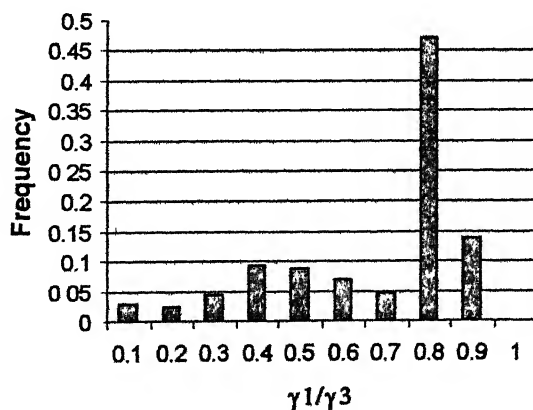
(c) Ni-30% Co

14-1



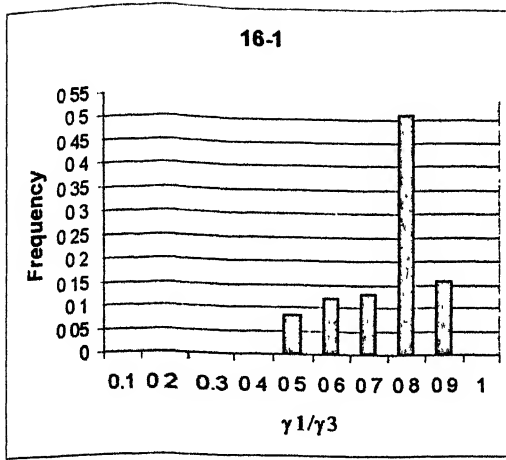
(d) Ni 40% Co

15-1

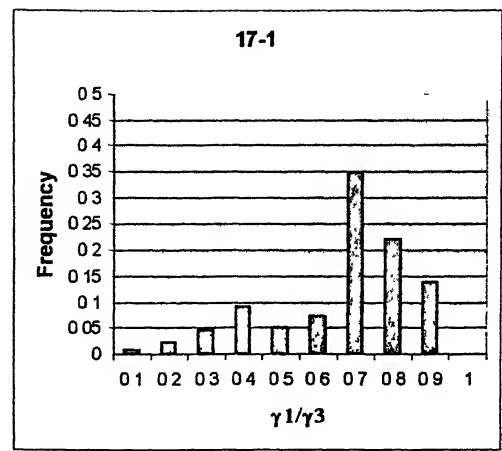


(e) Ni-60% Co

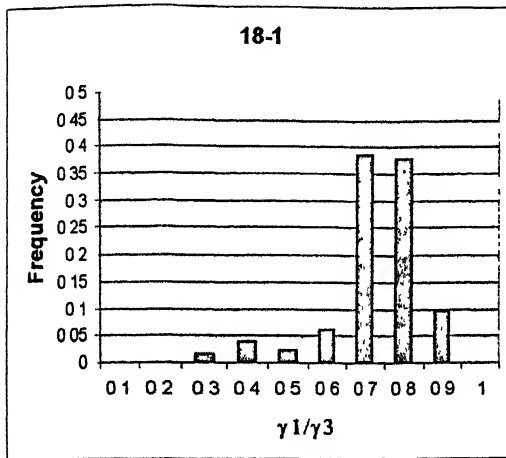
**Figure 4.12:** Frequency distribution of relative energy ratio  $\gamma_1/\gamma_3$  of different Ni-Co alloys annealed for 1 hour.



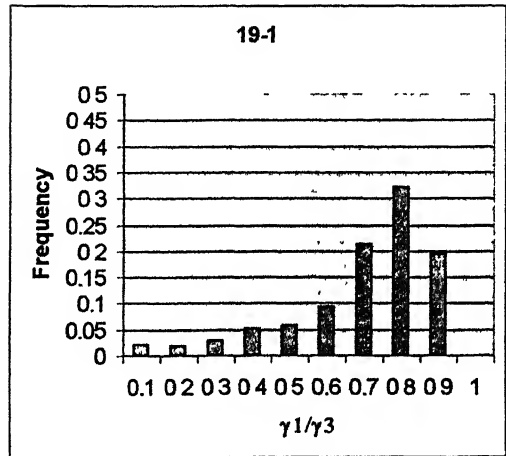
(a) Ni-10% Co



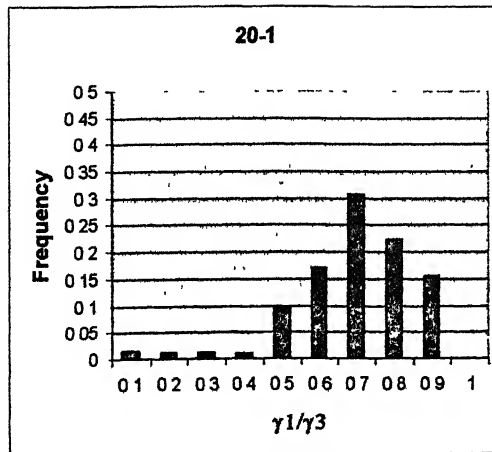
(b) Ni-20% Co



(c) Ni-30% Co

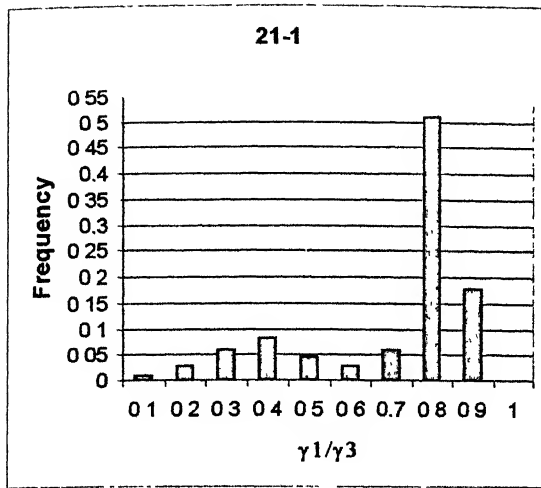


(d) Ni-40% Co

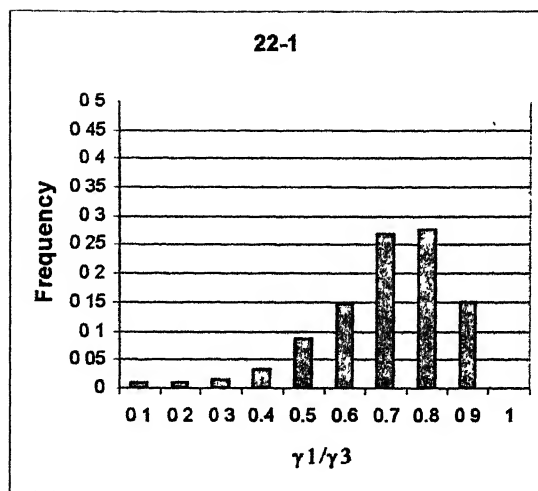


(e) Ni-60% Co

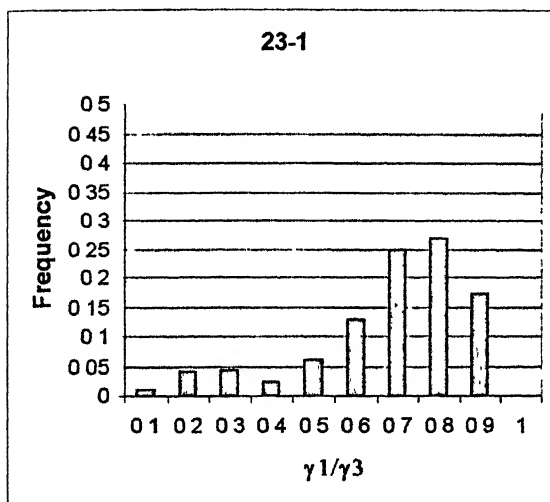
**Figure 4.13:** Frequency distribution of relative energy ratio  $\gamma_1/\gamma_3$  of different Ni-Co alloys annealed for 3 hours.



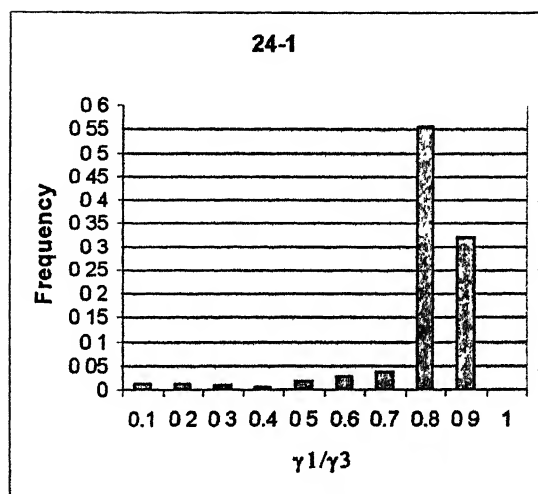
(a) Ni-10% Co



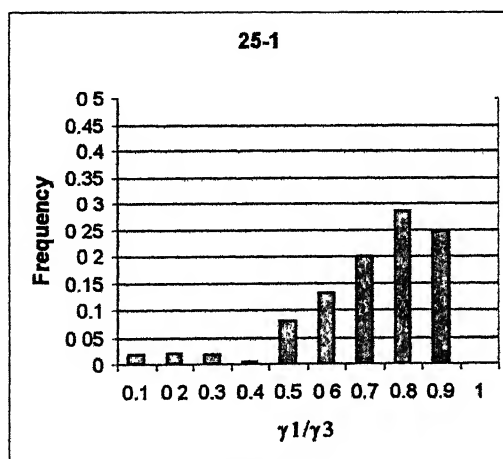
(b) Ni-20% Co



(c) Ni-30% Co

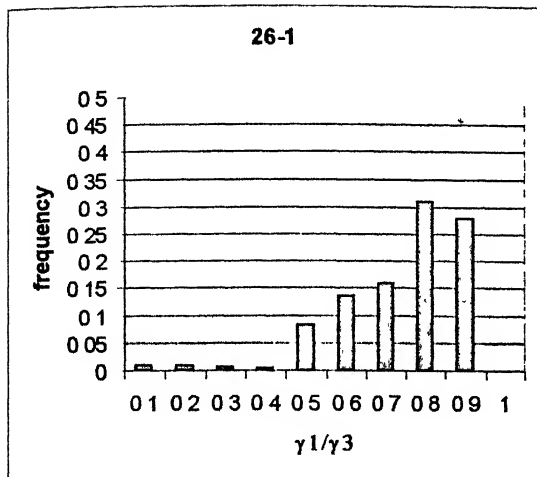


(d) Ni-40% Co

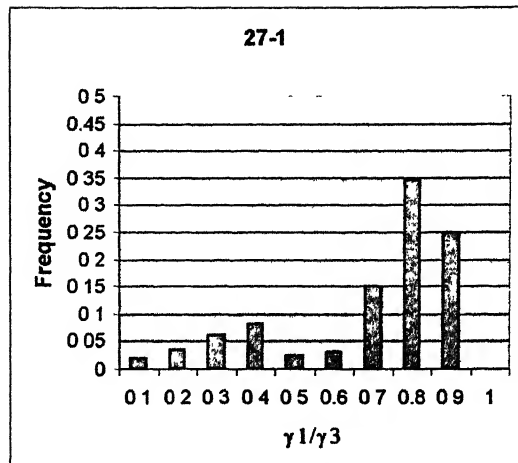


(e) Ni-60% Co

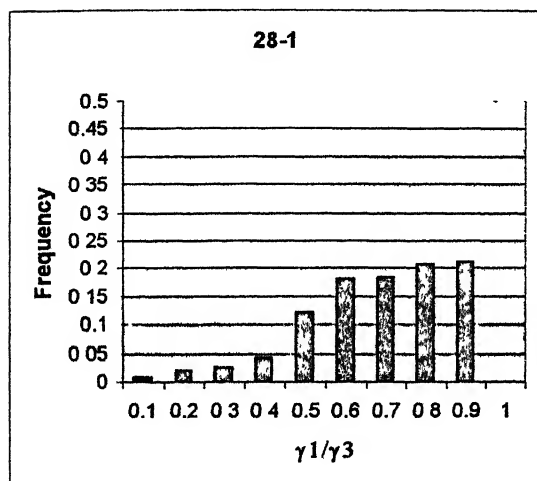
**Figure 4.14:** Frequency distribution of relative energy ratio  $\gamma_1/\gamma_3$  of different alloys annealed for 10 hours.



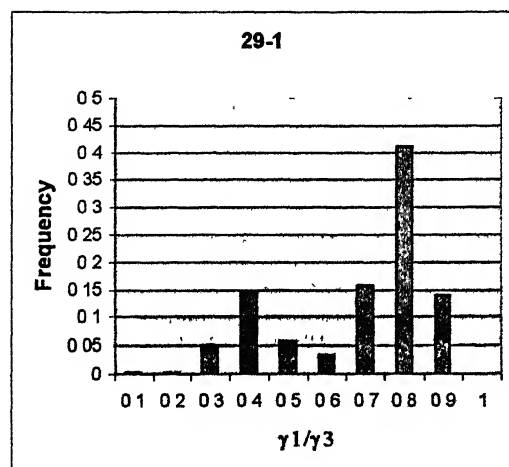
(a) Ni-10% Co



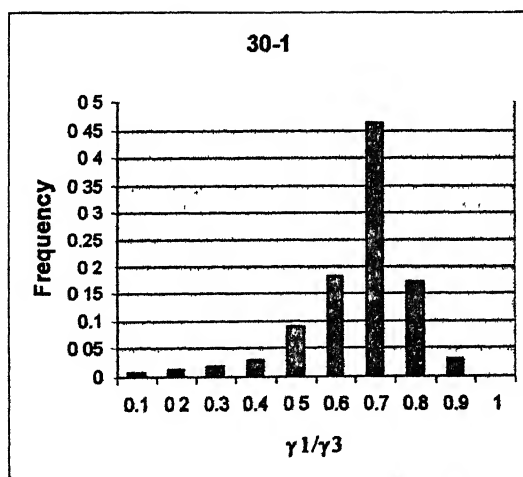
(b) Ni-20% Co



(c) Ni-30% Co



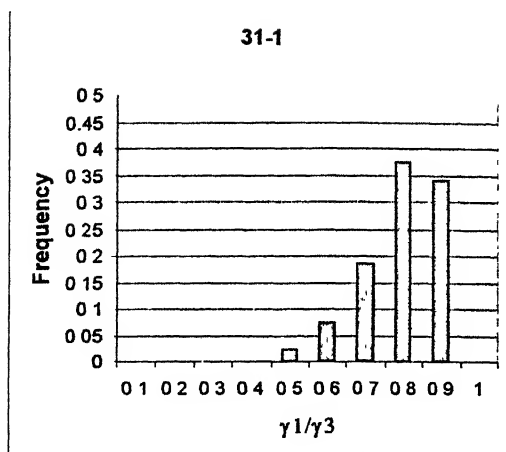
(d) Ni-40% Co



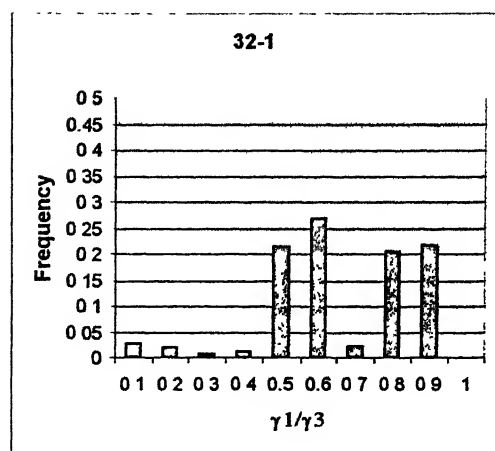
(e) Ni-60% Co

**Figure 4.15:** Frequency distribution of  $\gamma_1/\gamma_3$  energy ratio of different alloys annealed for 20 hours.

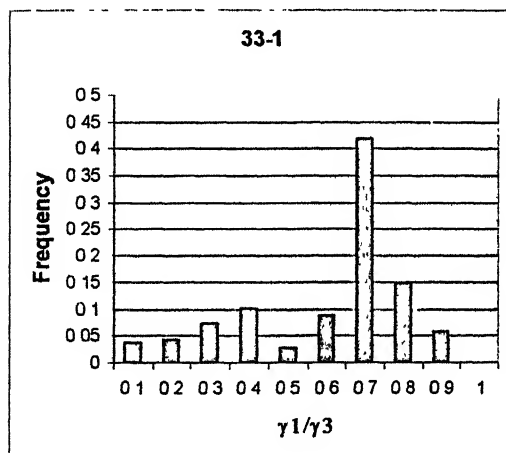




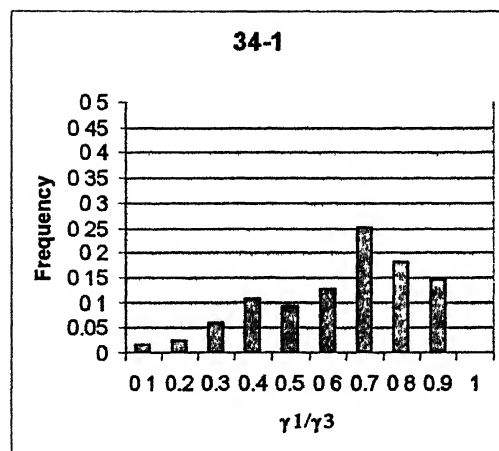
(a) Ni-10 % Co



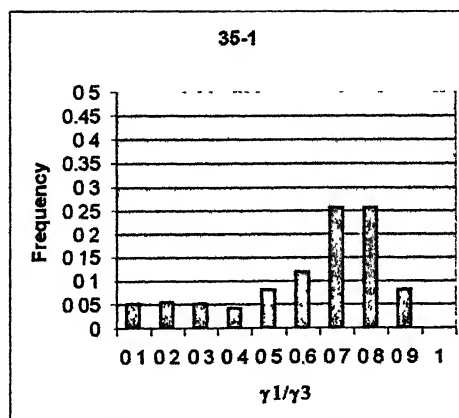
(b) Ni-20% Co



(c) Ni-30% Co



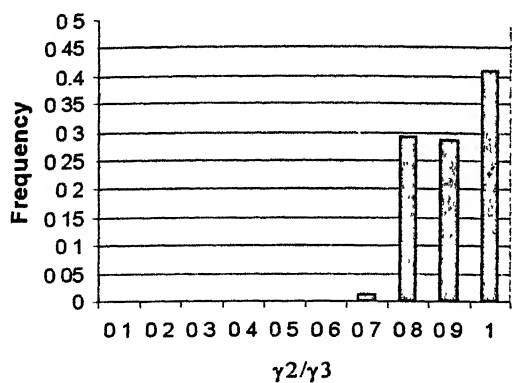
(d) Ni-40% Co



(e) Ni-60% Co

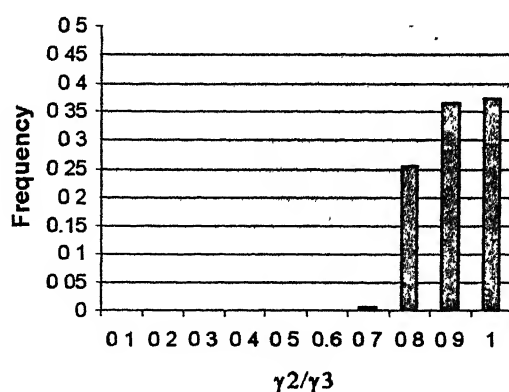
**Figure 4.16:** Frequency distribution of relative energy ratio  $\gamma_1/\gamma_3$  of different Ni-Co alloys annealed for 50 hours.

1-2



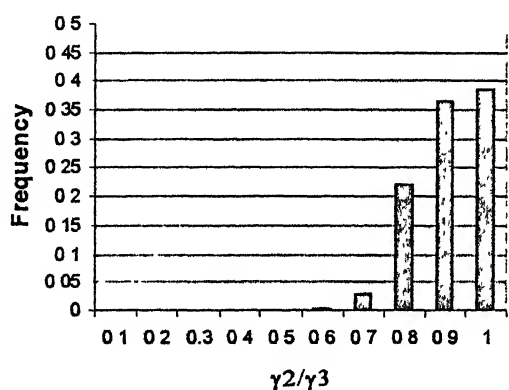
(a) Ni-10% Co

2-2



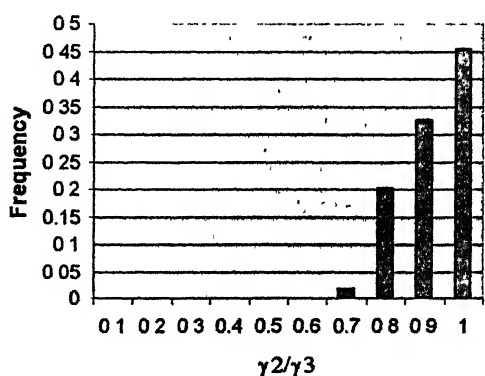
(b) Ni-20% Co

3-2



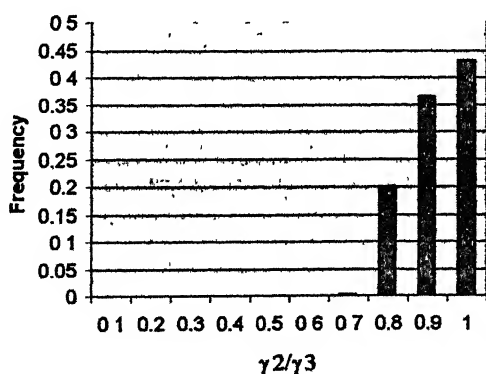
(c) Ni-30% Co

4-2



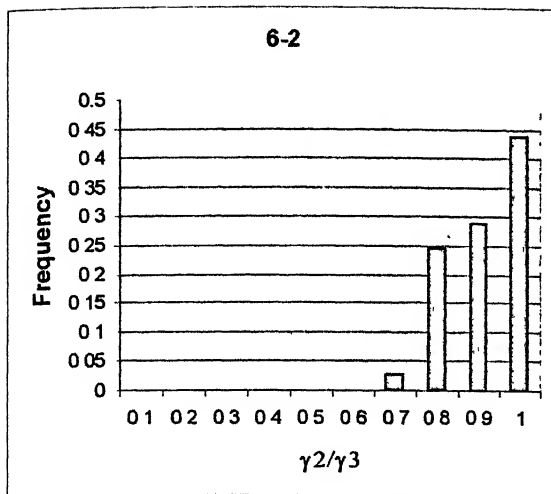
(d) Ni-40% Co

5-2

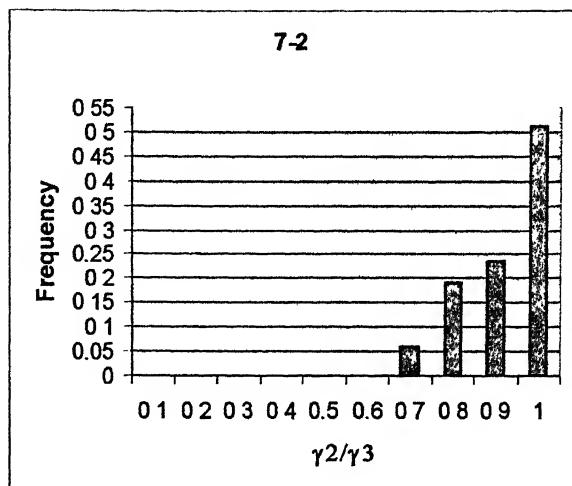


(e) Ni-60% Co

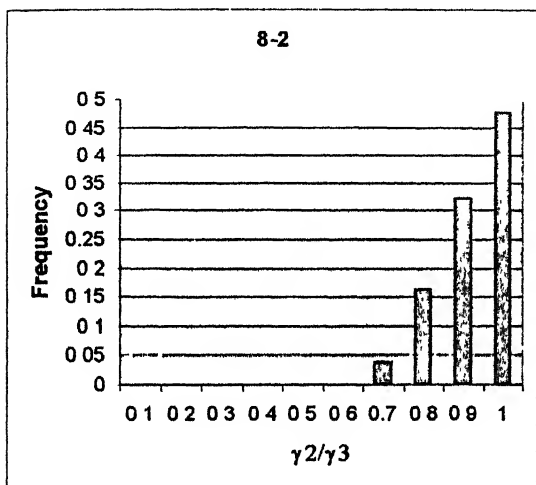
**Figure 4.17:** Frequency distribution of relative energy ratio  $\gamma_2/\gamma_3$  of different Ni-Co alloys annealed for 15 minutes.



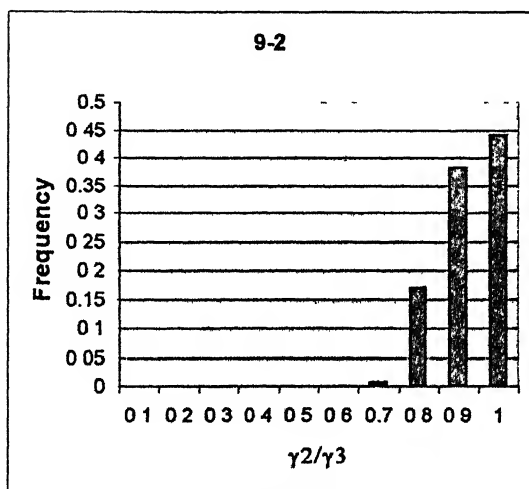
(a) Ni-10% Co



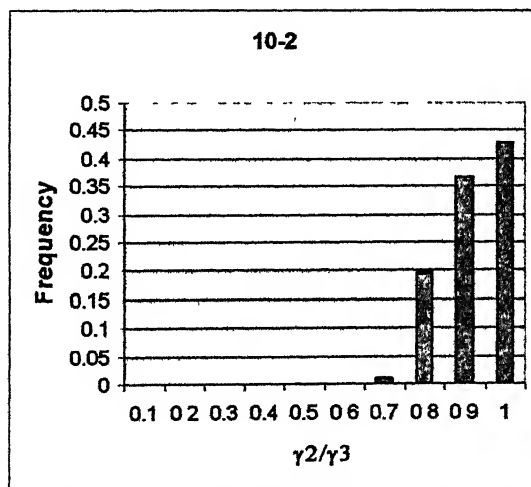
(b) Ni-20% Co



(c) Ni-30% Co

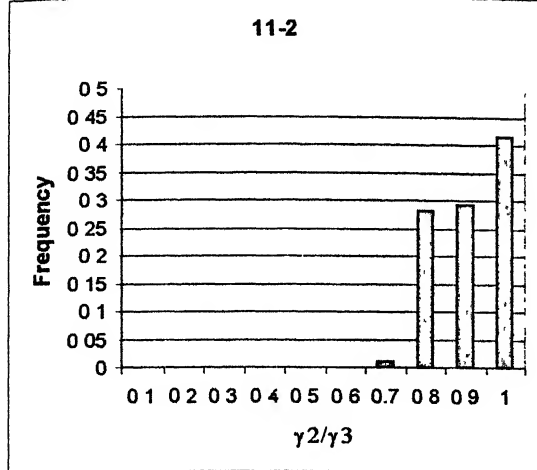


(d) Ni-40% Co

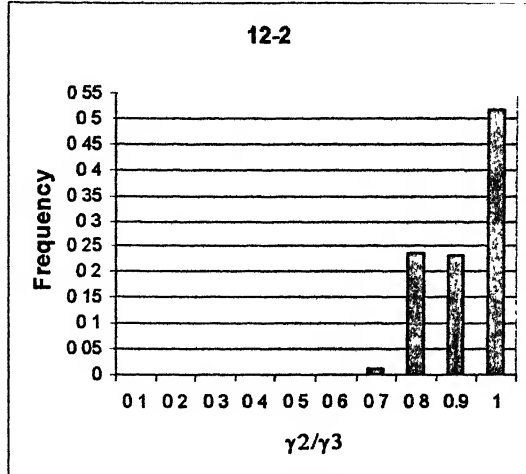


(e) Ni-60% Co

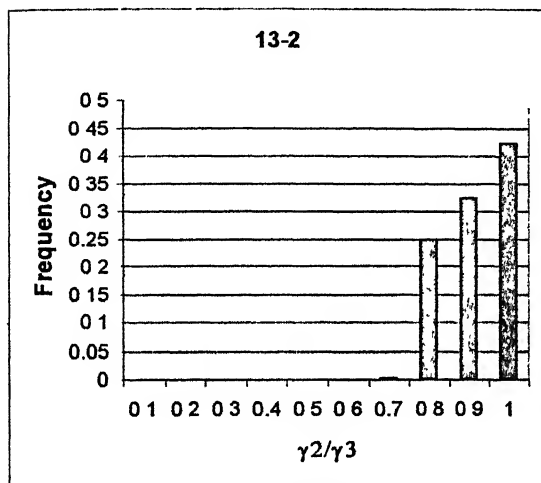
**Figure 18:** Frequency distribution of relative energy ratio  $\gamma_2/\gamma_3$  of different Ni-Co alloys annealed for 30 minutes.



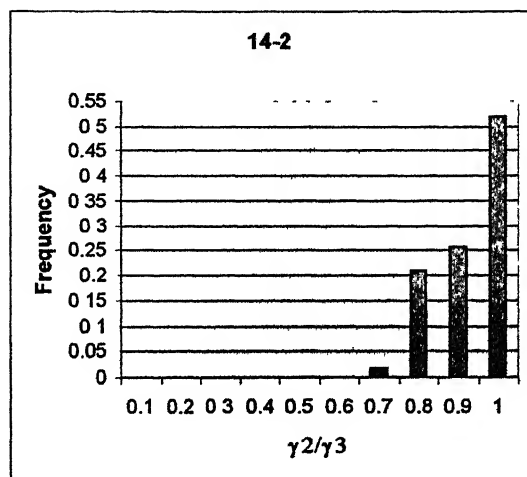
(a) Ni-10% Co



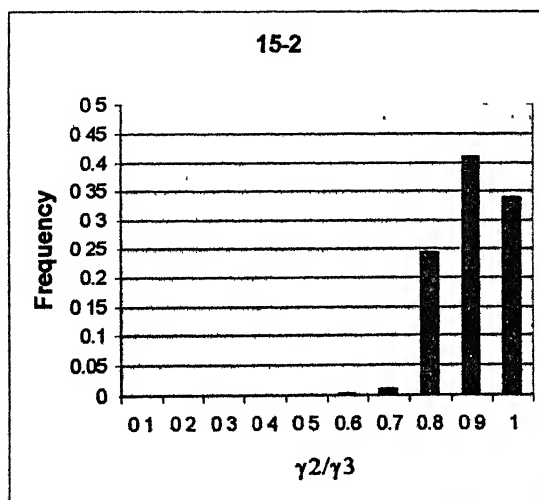
(b) Ni-20% Co



(c) Ni-30% Co

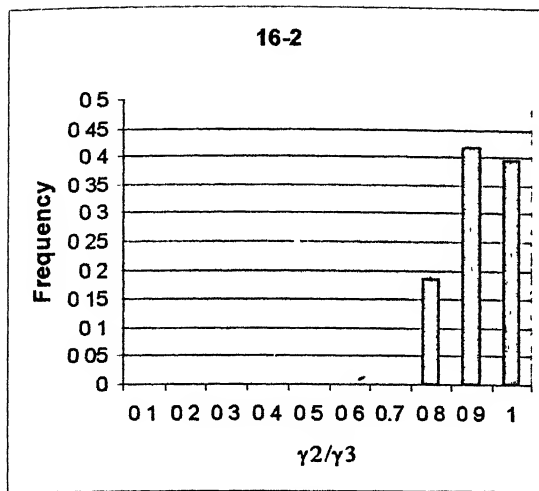


(d) Ni-40% Co

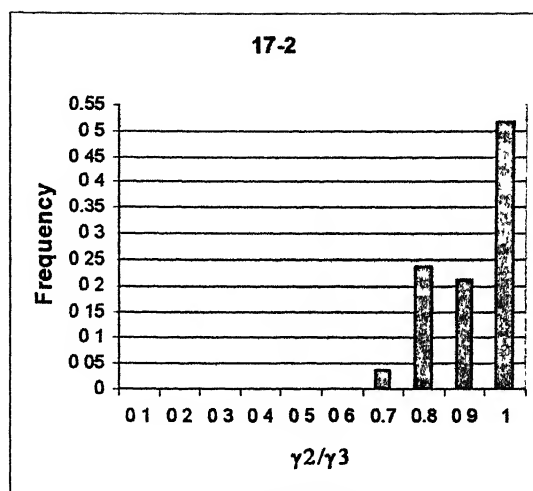


(e) Ni-60% Co

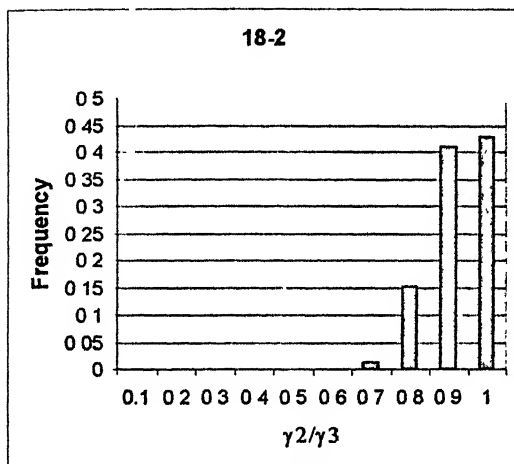
**Figure 19:** Frequency distribution of relative energy ratio  $\gamma_2/\gamma_3$  of different Ni-Co alloys annealed for 1 hour.



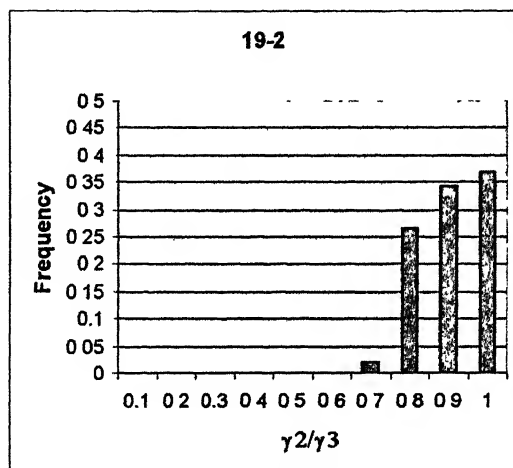
(a) Ni-10% Co



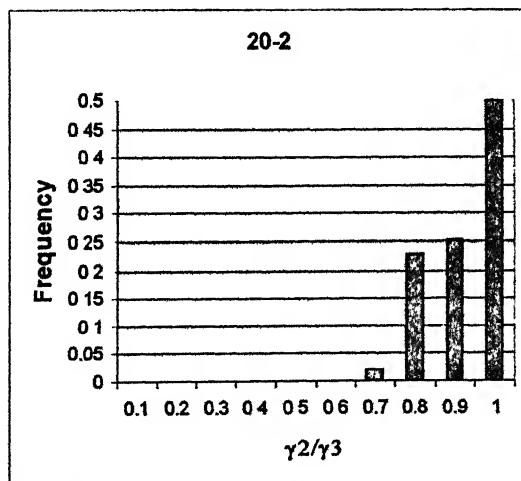
(b) Ni-20% Co



(c) Ni-30% Co

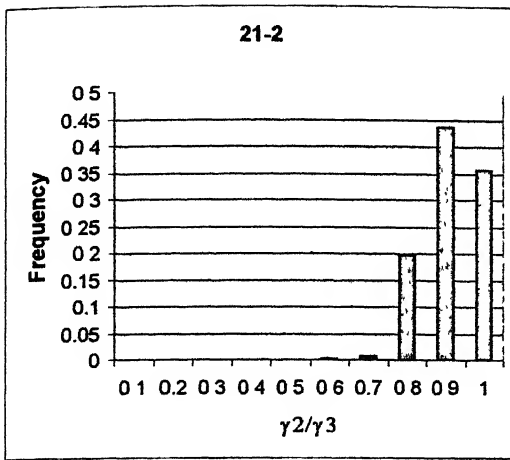


(d) Ni-40% Co

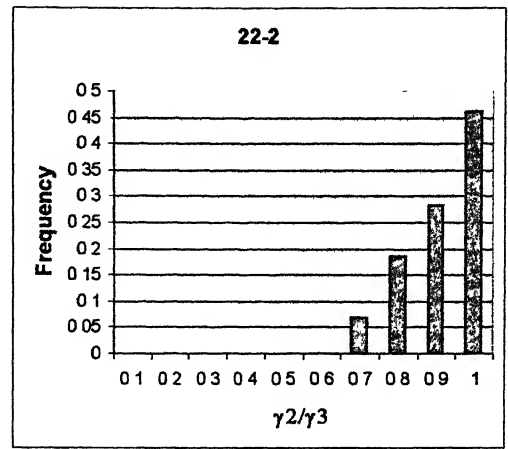


(e) Ni-60% Co

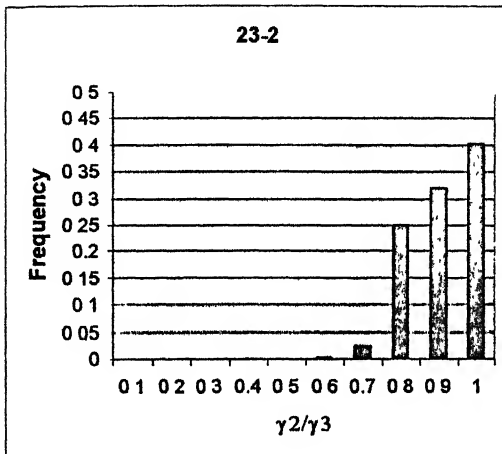
**Figure 4.20:** Frequency distribution of relative energy ratio  $\gamma_2/\gamma_3$  of different Ni-Co alloys annealed for 3 hours.



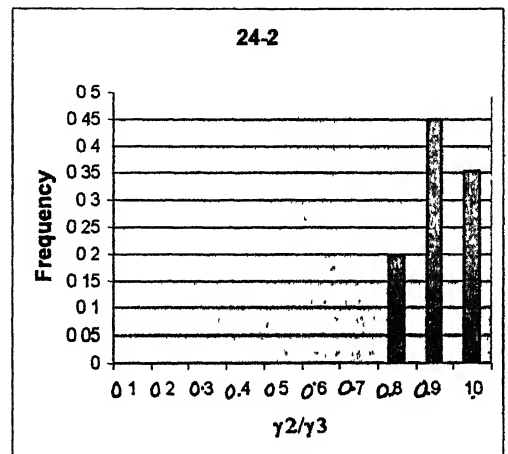
(a) Ni-10% Co



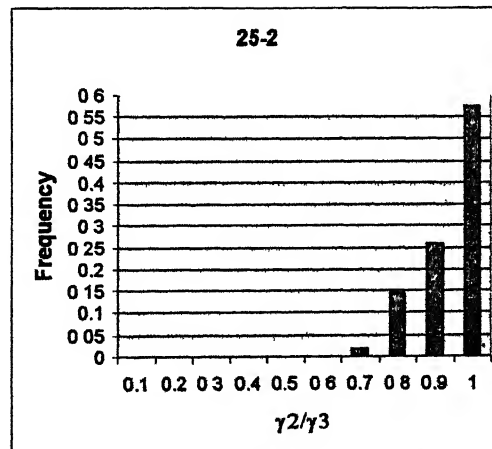
(b) Ni-20% Co



(c) Ni-30% Co

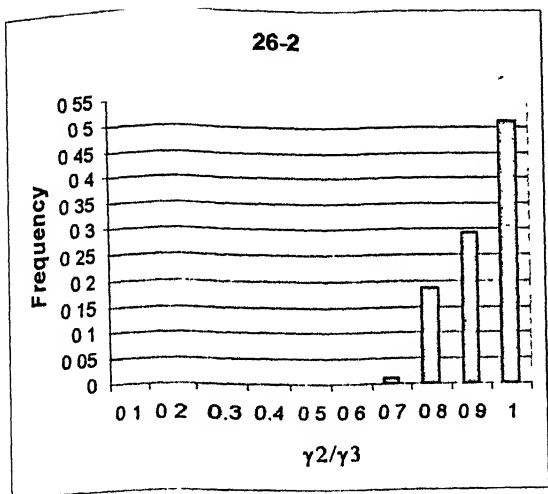


(d) Ni-40% Co

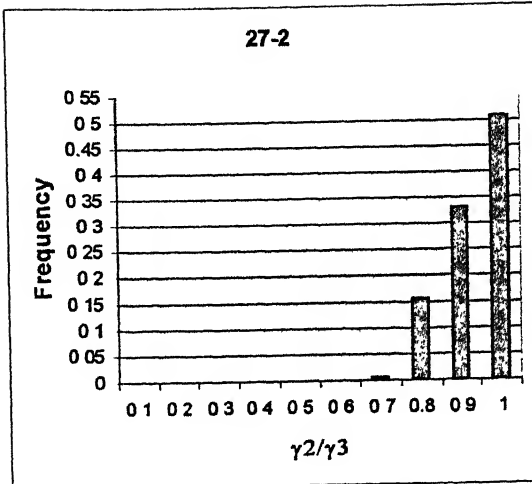


(e) Ni-60% Co

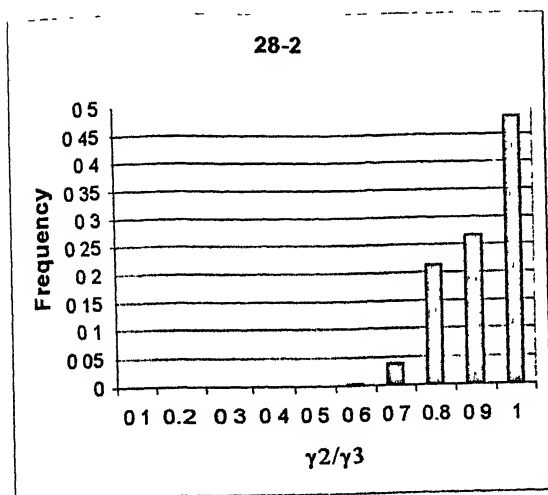
**Figure 4.21:** Frequency distribution of relative energy ratio  $\gamma_2/\gamma_3$  of different Ni-Co alloys annealed for 10 hours.



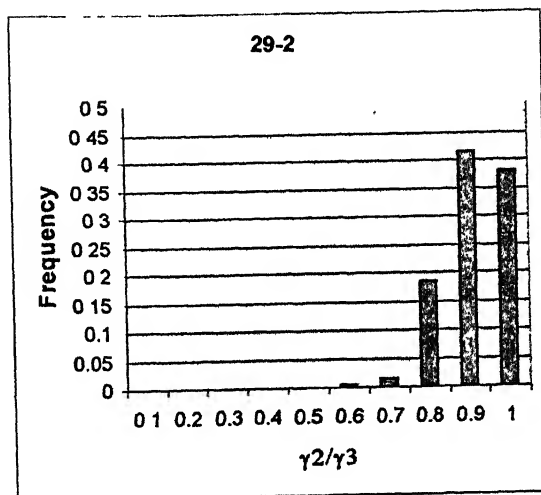
(a) Ni-10% Co



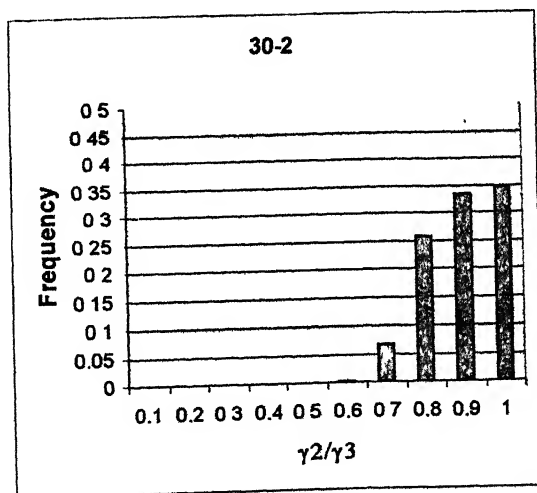
(b) Ni-20% Co



(c) Ni-30% Co

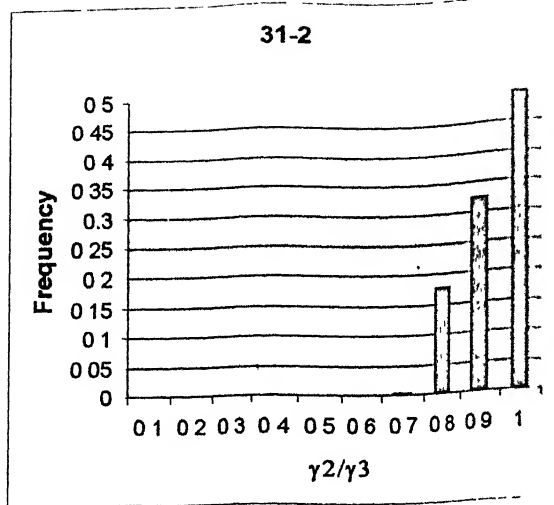


(d) Ni-40% Co

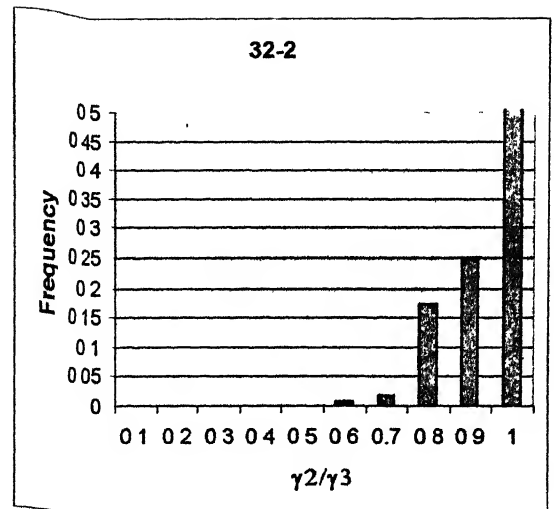


(e) Ni-60% Co

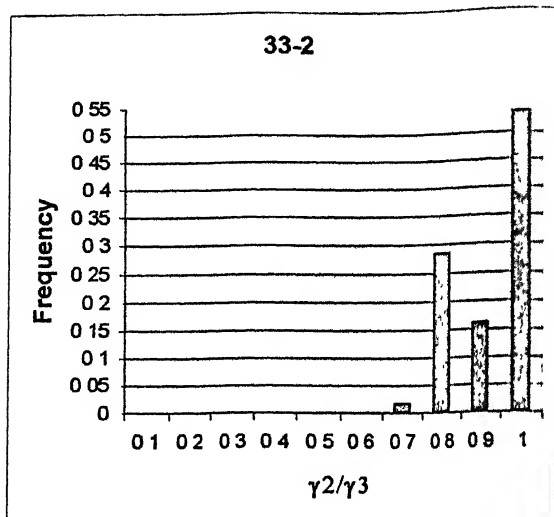
**Figure 4.22:** Frequency distribution of relative energy ratio  $\gamma_2/\gamma_3$  of different Ni-Co alloys annealed for 20 hours.



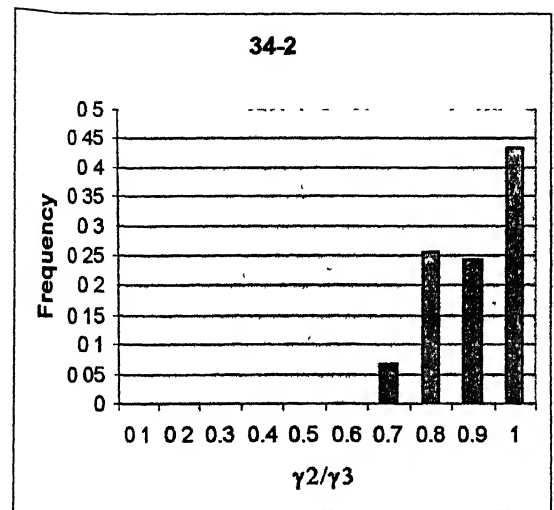
(a) Ni-10% Co



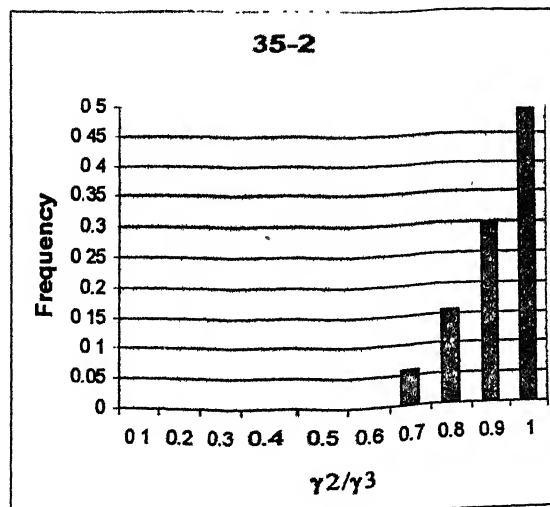
(b) Ni-20% Co



(c) Ni-30% Co



(d) Ni-40% Co



(e) Ni-60% Co

**Figure 4.23:** Frequency distribution of relative energy ratio  $\gamma_2/\gamma_3$  of different Ni-Co alloys annealed for 50 hours.



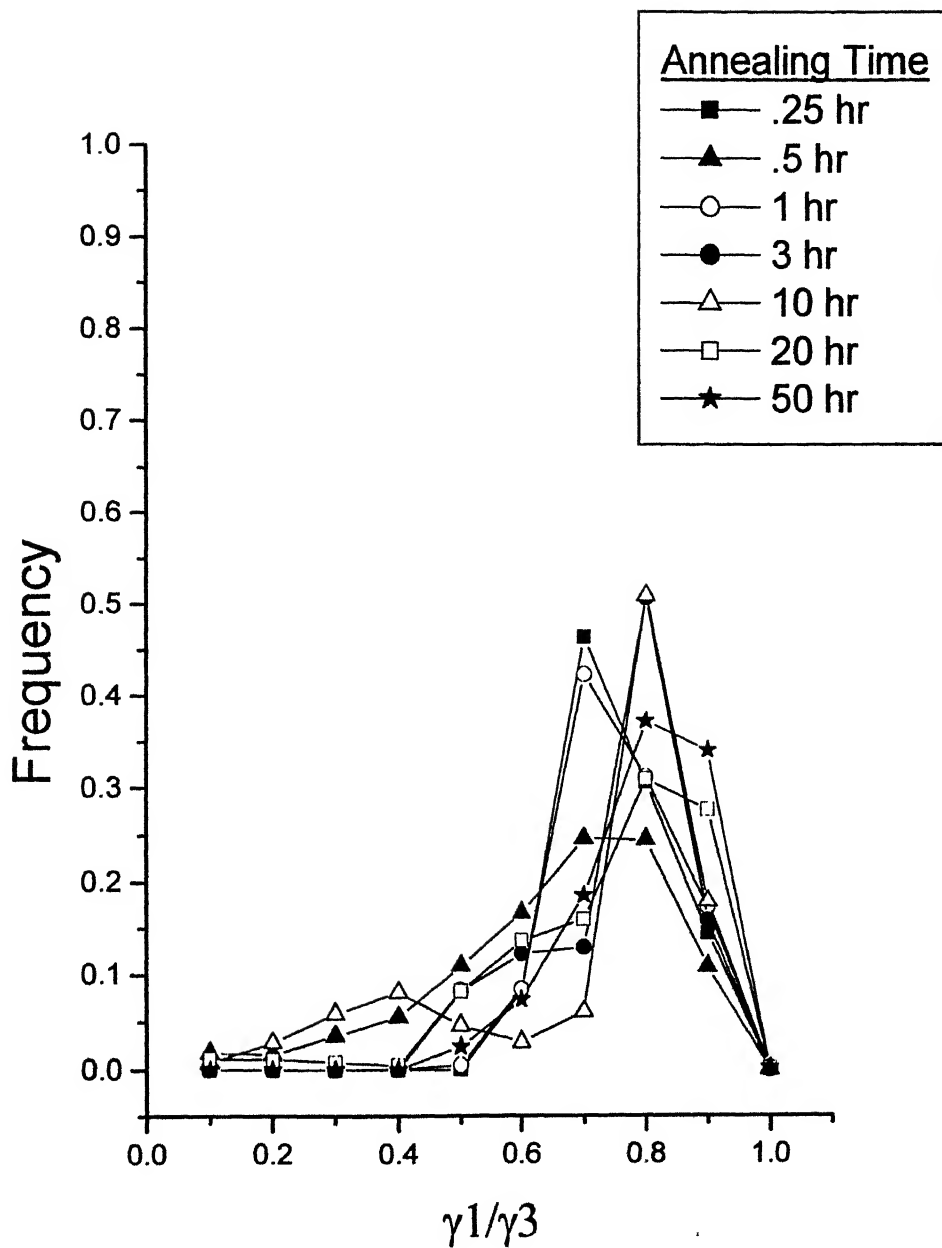


**Figure 4.24:** Frequency distribution of relative grain boundary energy ratio  $\gamma_1/\gamma_3$  for Ni-10% Co samples subjected to different annealing times.

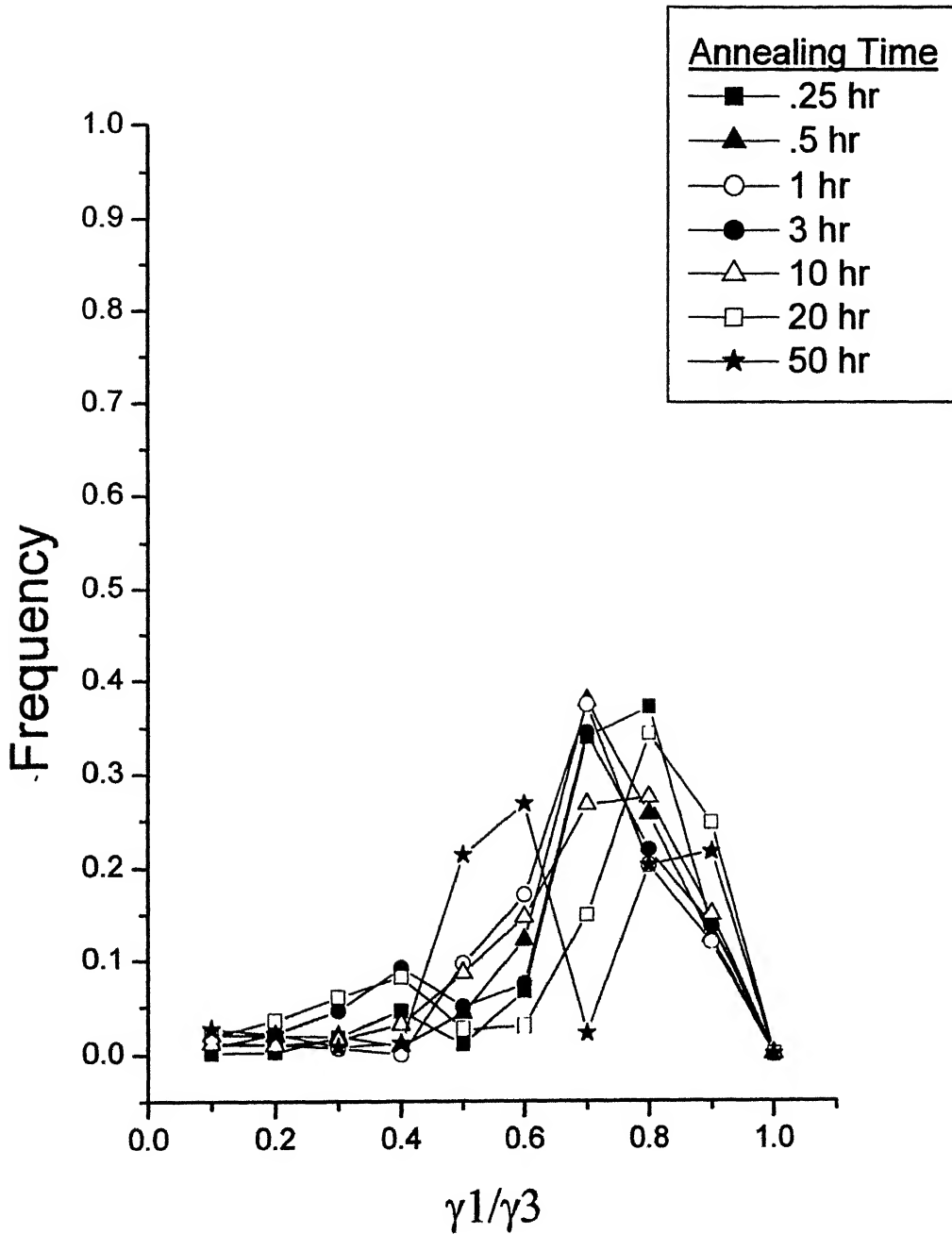


**Figure 4.25:** Frequency distribution of relative grain boundary energy ratio  $\gamma_1/\gamma_3$  for Ni-20% Co samples subjected to different annealing times.

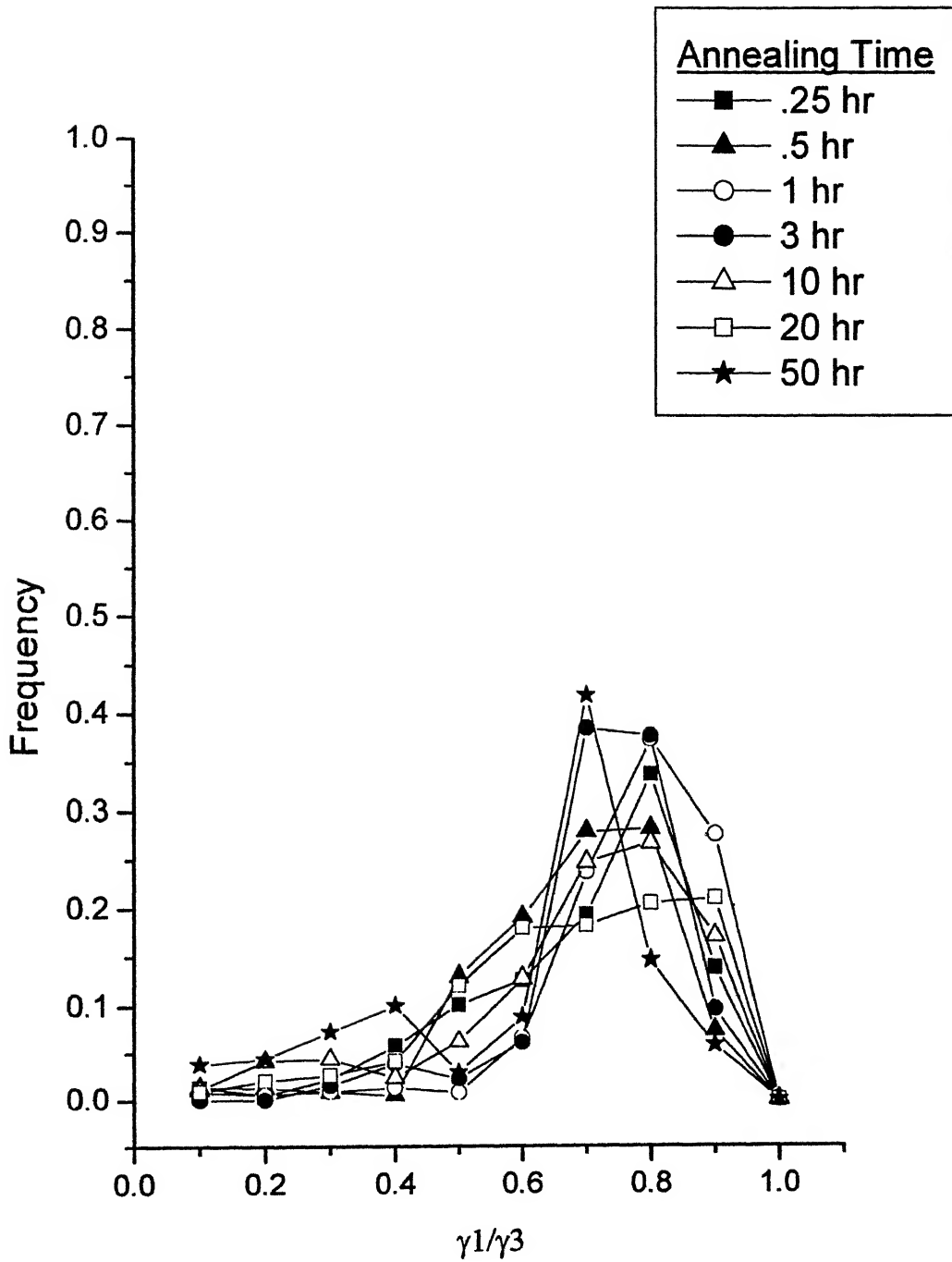


**Figure 4.26:** Frequency distribution of relative grain boundary energy ratio  $\gamma_1/\gamma_3$  for Ni-30% Co samples subjected to different annealing times.

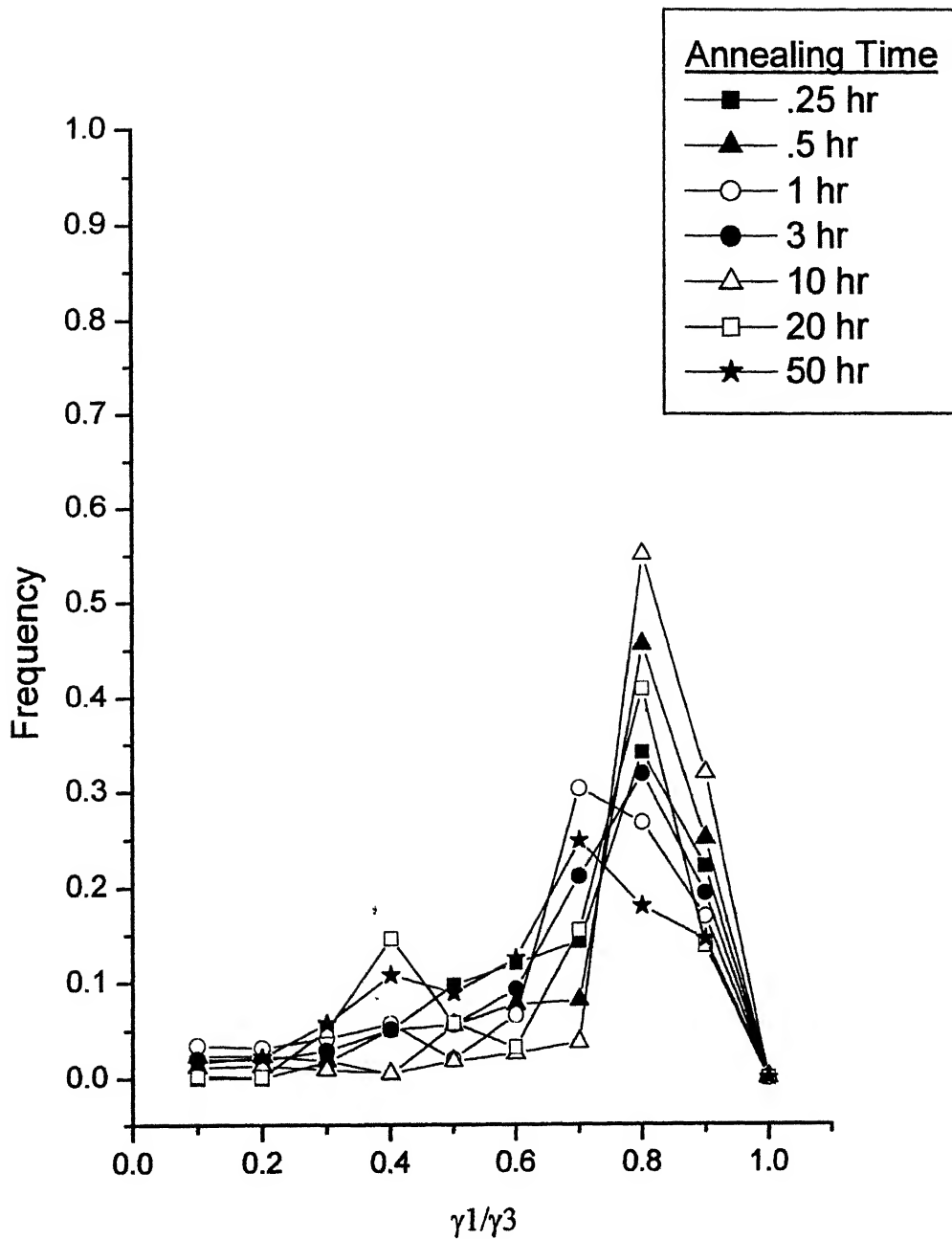


**Figure 4.27:** Frequency distribution of relative grain boundary energy ratio  $\gamma_1/\gamma_3$  for Ni-40% Co samples subjected to different annealing times.

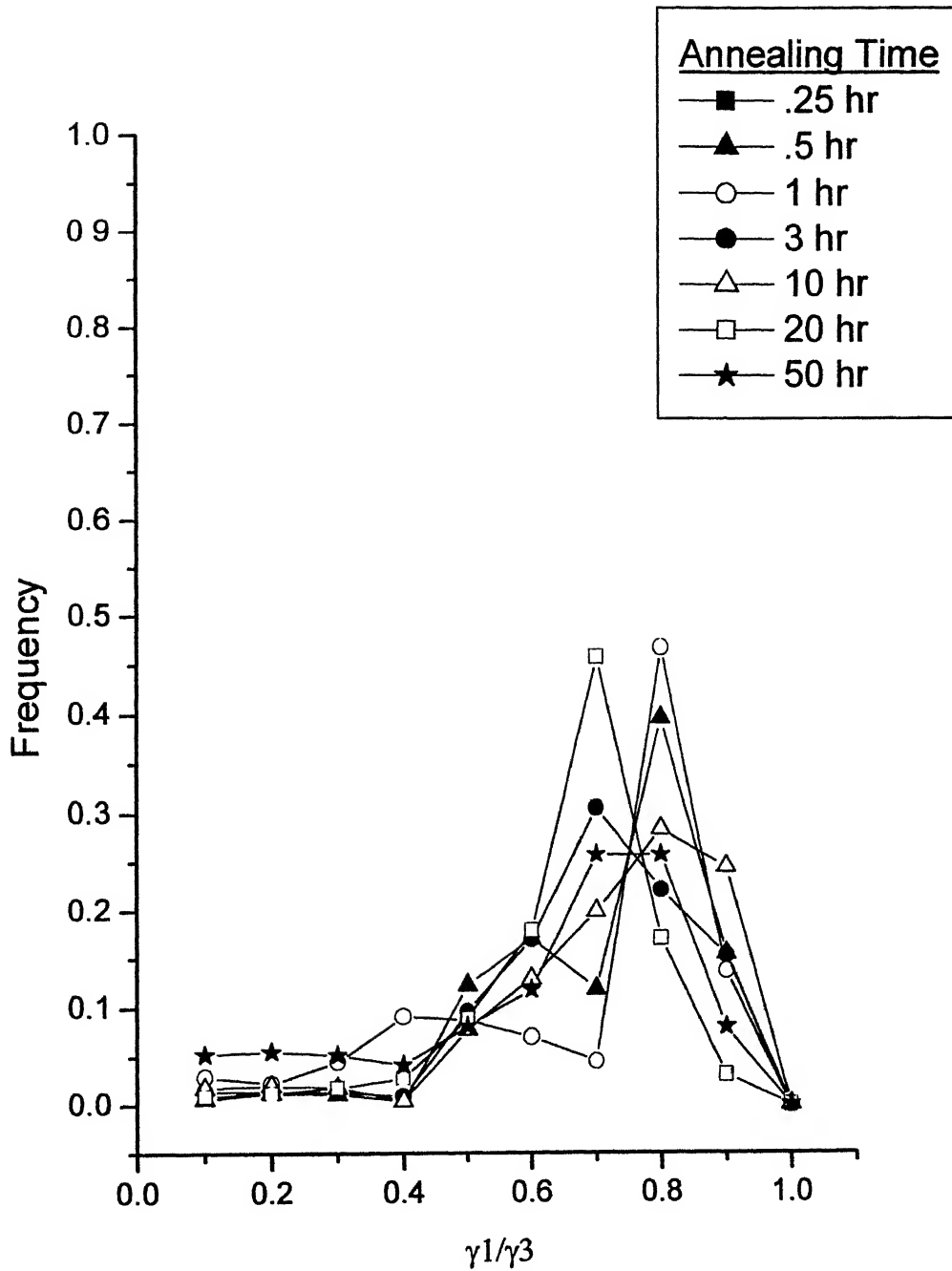


**Figure 4.28:** Frequency distribution of relative grain boundary energy ratio  $\gamma_1/\gamma_3$  for Ni-60% Co samples subjected to different annealing times.

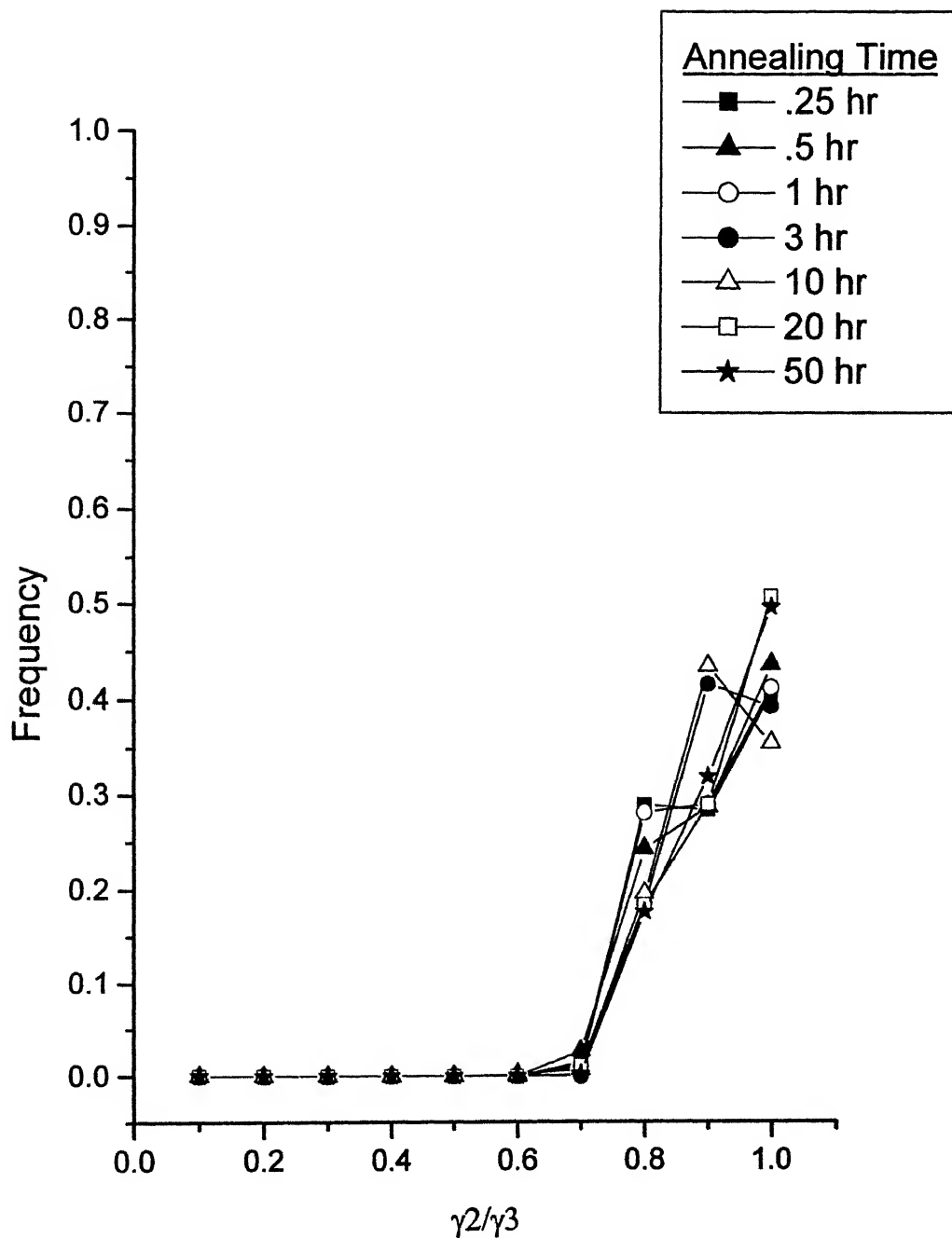


**Figure 4.29:** Frequency distribution of relative grain boundary energy ratio  $\gamma_2/\gamma_3$  for Ni-10% Co samples subjected to different annealing times.

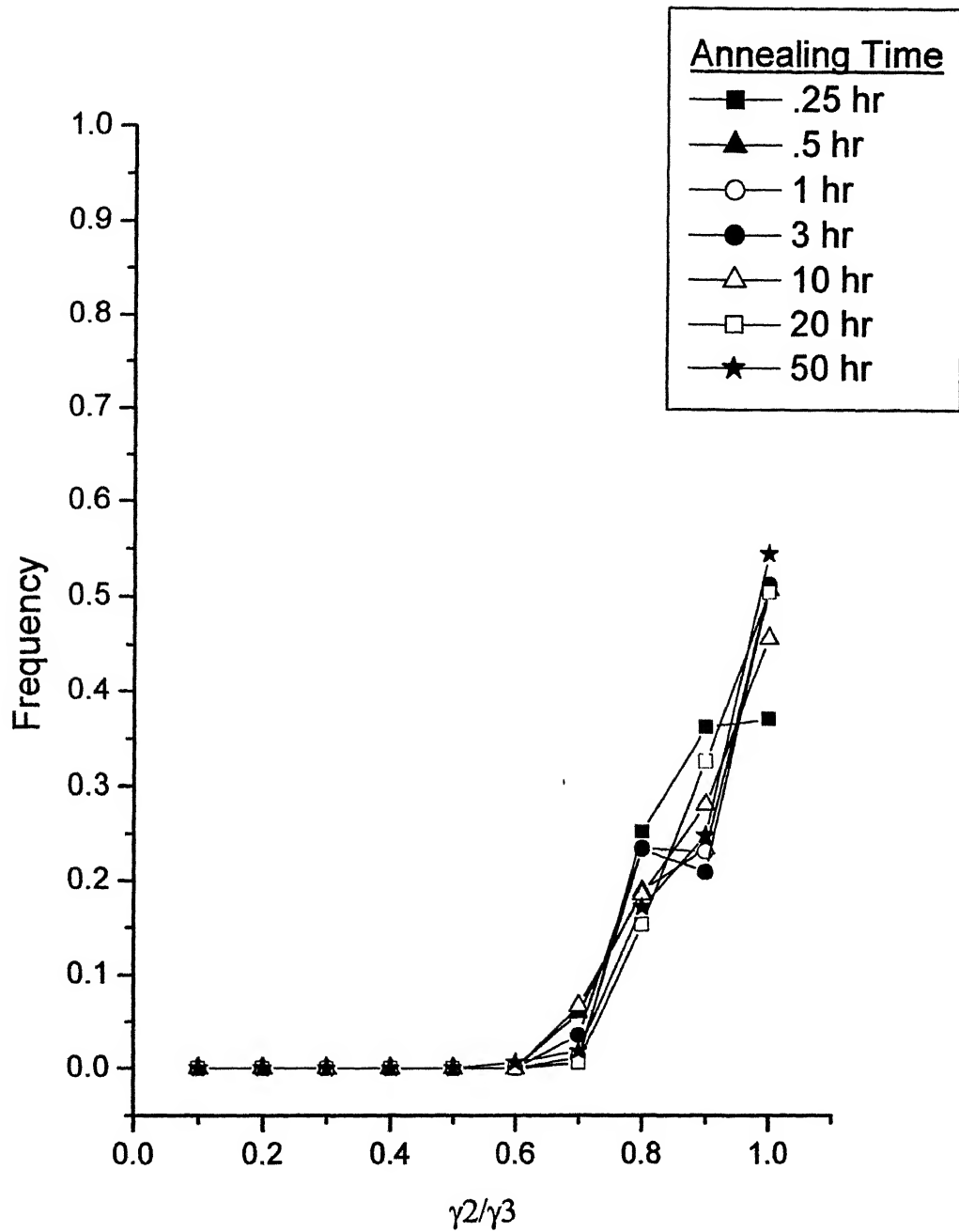


**Figure 4.30:** Frequency distribution of relative grain boundary energy ratio  $\gamma_2/\gamma_3$  for Ni-20% Co samples subjected to different annealing times.

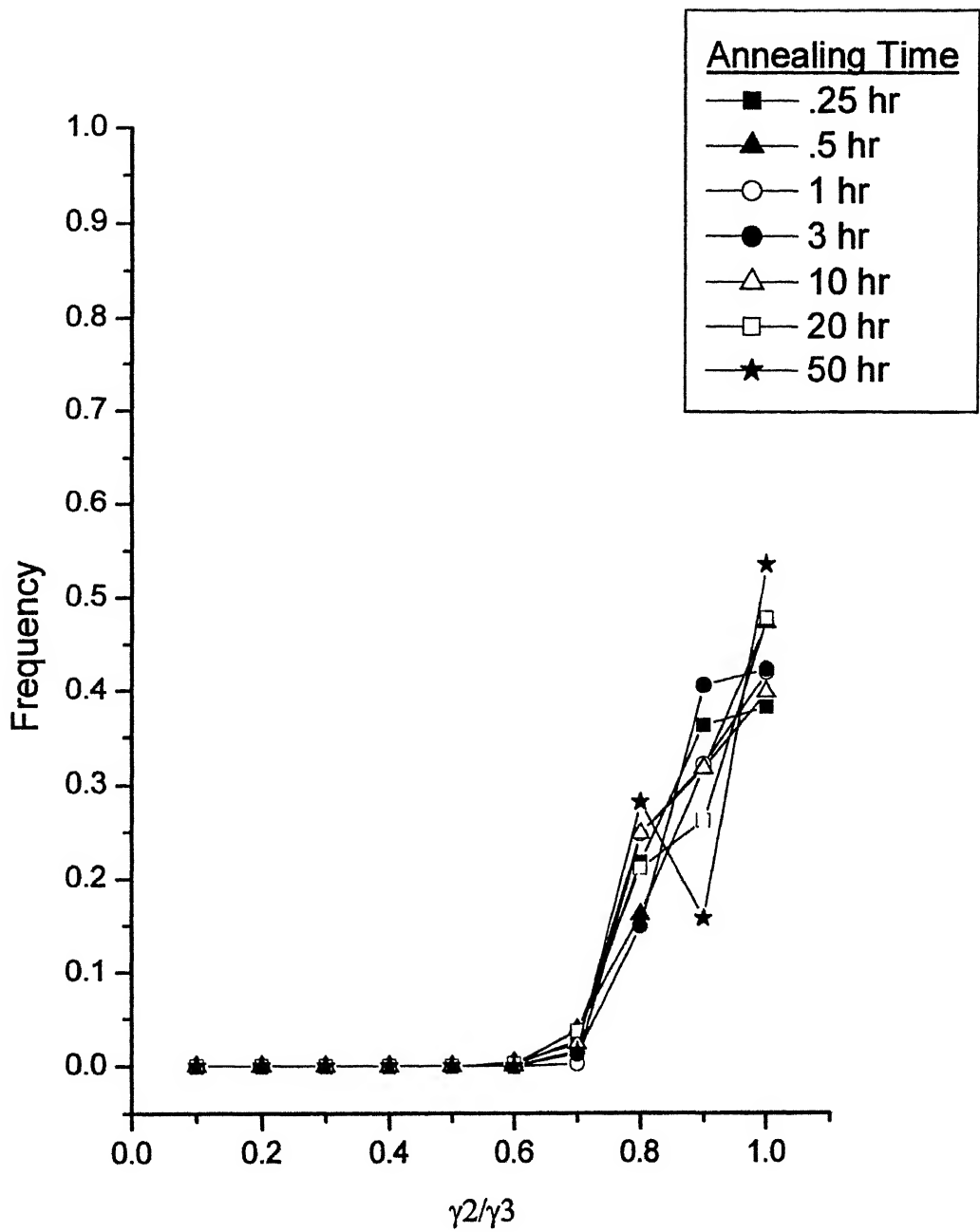


**Figure 4.31:** Frequency distribution of relative grain boundary energy ratio  $\gamma_2/\gamma_3$  for Ni-30% Co samples subjected to different annealing times.



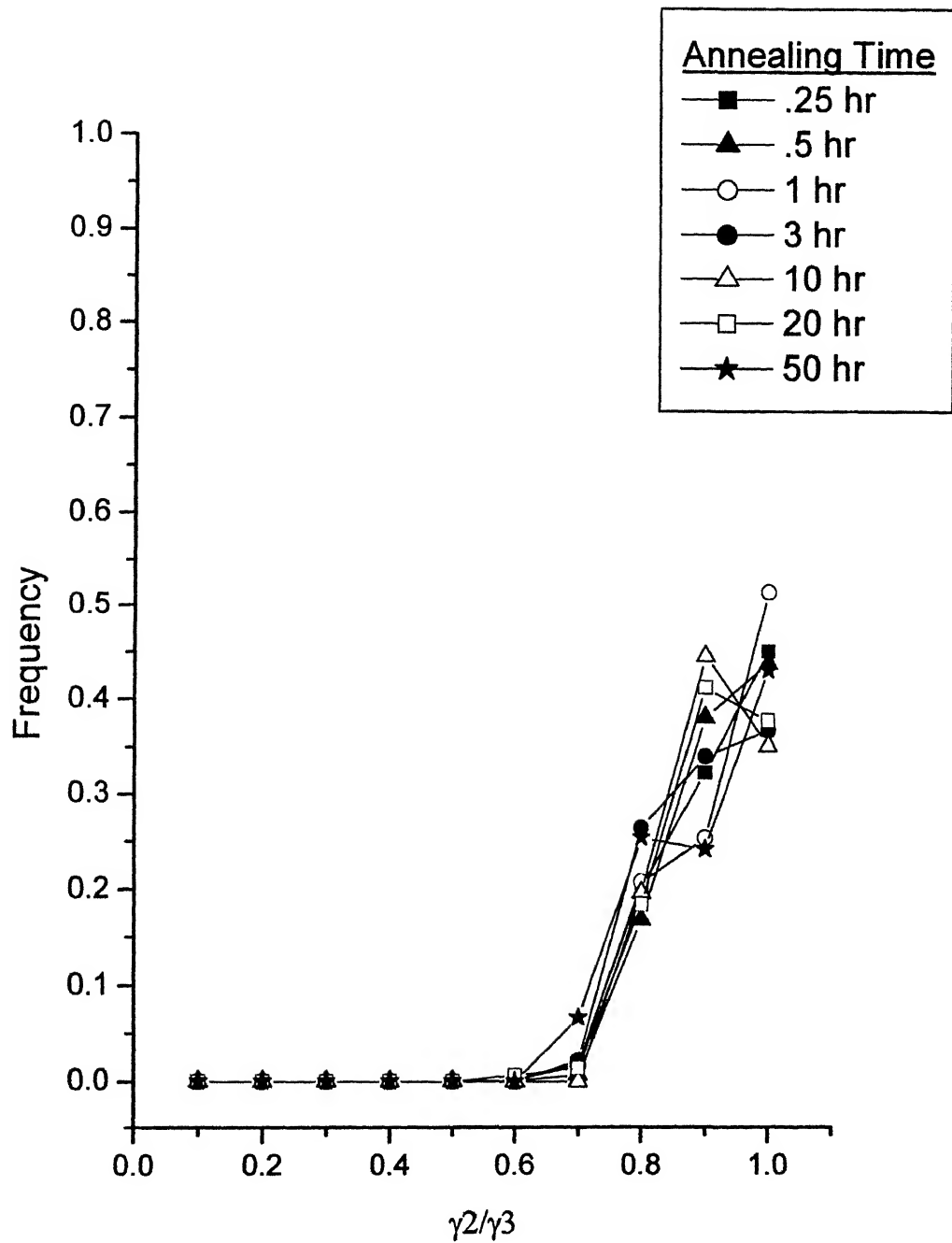


**Figure 4.32:** Frequency distribution of relative grain boundary energy ratio  $\gamma_2/\gamma_3$  for Ni-40% Co samples subjected to different annealing times.

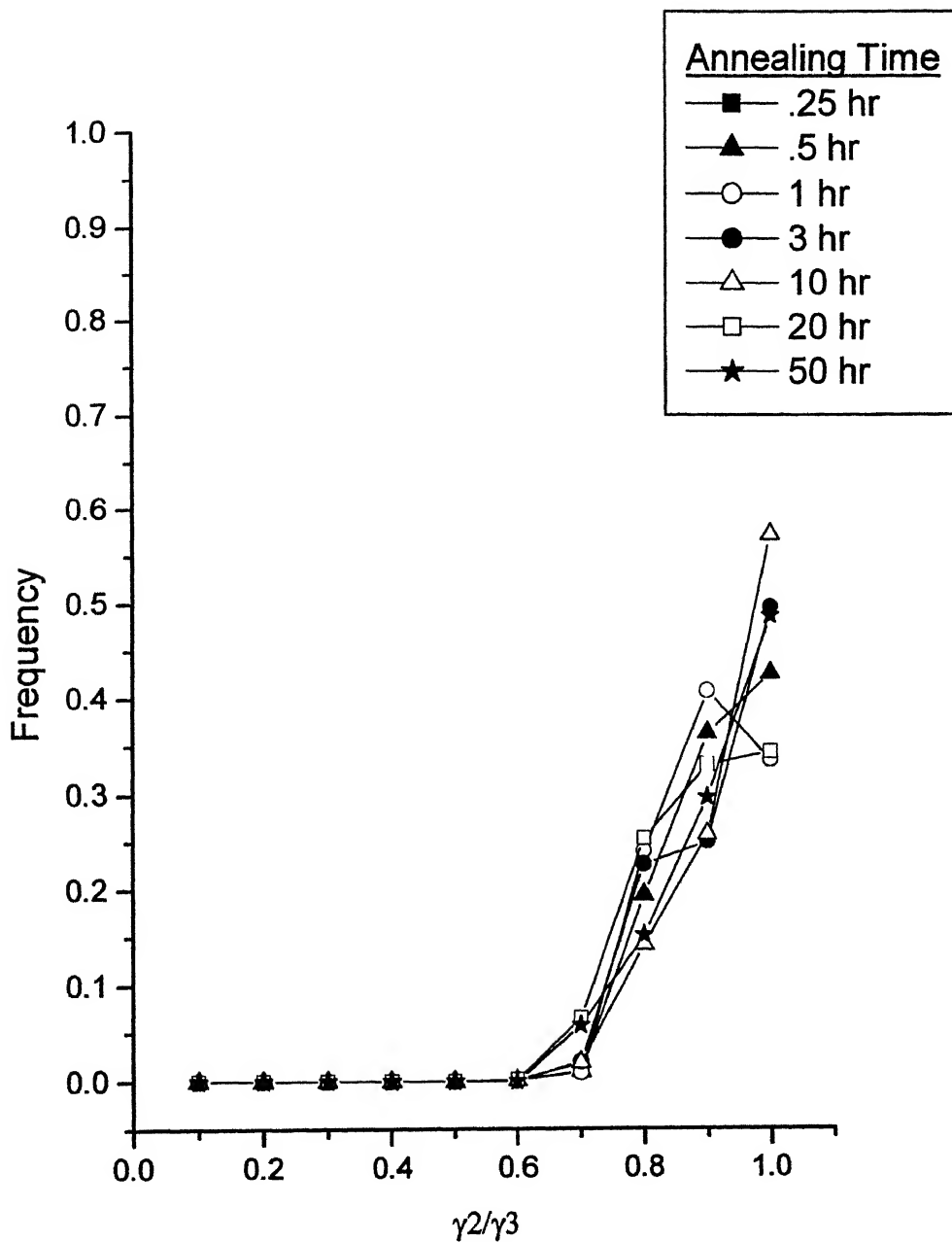


**Figure 4.33:** Frequency distribution of relative grain boundary energy ratio  $\gamma_2/\gamma_3$  for Ni-60% Co samples subjected to different annealing times.

Beyond that there is an increase in frequency upto the  $\gamma_2/\gamma_3$  ratio of 1. The fact is that the distribution of grain boundary energies is quite similar and this behavior is maintained for all the alloys. Although there is some small variation in the plots, it is not significant.

#### **4.2.3: VARIATION OF FREQUENCIES WITH ANNEALING TIME**

##### **4.2.3.1: FOR RELATIVE ENERGY RATIO $\gamma_1/\gamma_3$**

The frequencies of different classes of  $\gamma_1/\gamma_3$  as a function of annealing time in the five Ni-Co alloys are shown in **Figures 4.34 to 4.38**.

For Ni-10% Co alloy after 20 hours of annealing the frequencies of different classes of  $\gamma_1/\gamma_3$  become stabilized.

For Ni-20% Co the classes 0.5 to 0.6 and 0.7 to 0.8 of  $\gamma_1/\gamma_3$  increases drastically after 20 hours of annealing at the expense of other components.

For Ni-30% Co after 20 hours of annealing the 0.6 to 0.7 class of  $\gamma_1/\gamma_3$  starts growing drastically at the cost of other components.

For Ni-40% Co and Ni-60% Co all other classes of  $\gamma_1/\gamma_3$  except 0.6 to 0.7 and 0.7 to 0.8 reach an equilibrium value after 20 hours of annealing. From the initial stage of annealing they grow at the expense of each other. After 50 hours of annealing they are present in equal frequencies.

##### **4.2.3.2: FOR RELATIVE ENERGY RATIO $\gamma_2/\gamma_3$**

The frequencies of different classes of  $\gamma_2/\gamma_3$  as a function of annealing time in the four Ni-Fe alloys are shown in **Figures 4.39 to 4.43**. In this case the important classes of  $\gamma_2/\gamma_3$  are 0.7 to 0.8, 0.8 to 0.9 and 0.9 to 1.

In Ni-10% Co alloy the classes 0.8 to 0.9 and 0.9 to 1 of  $\gamma_2/\gamma_3$  grow at the expense of one another.

The class of  $\gamma_2/\gamma_3$  having maximum frequency in Ni-20% Co and Ni-30% Co is 0.9 to 1.

In Ni-40% Co and Ni-60% Co alloys the classes 0.8 to 0.9 and 0.9 to 1 of  $\gamma_2/\gamma_3$  grow at the expense of one another.

#### **4.2.4: AVERAGE vs. ANNEALING TIME**

The variations of average values of  $\gamma_1/\gamma_3$  and  $\gamma_2/\gamma_3$  for the different alloys as a function of annealing time are shown in **Figures 4.44 and 4.45** respectively. After 20 hours of annealing Ni-10% Co alloy showed highest average value for  $\gamma_1/\gamma_3$  which

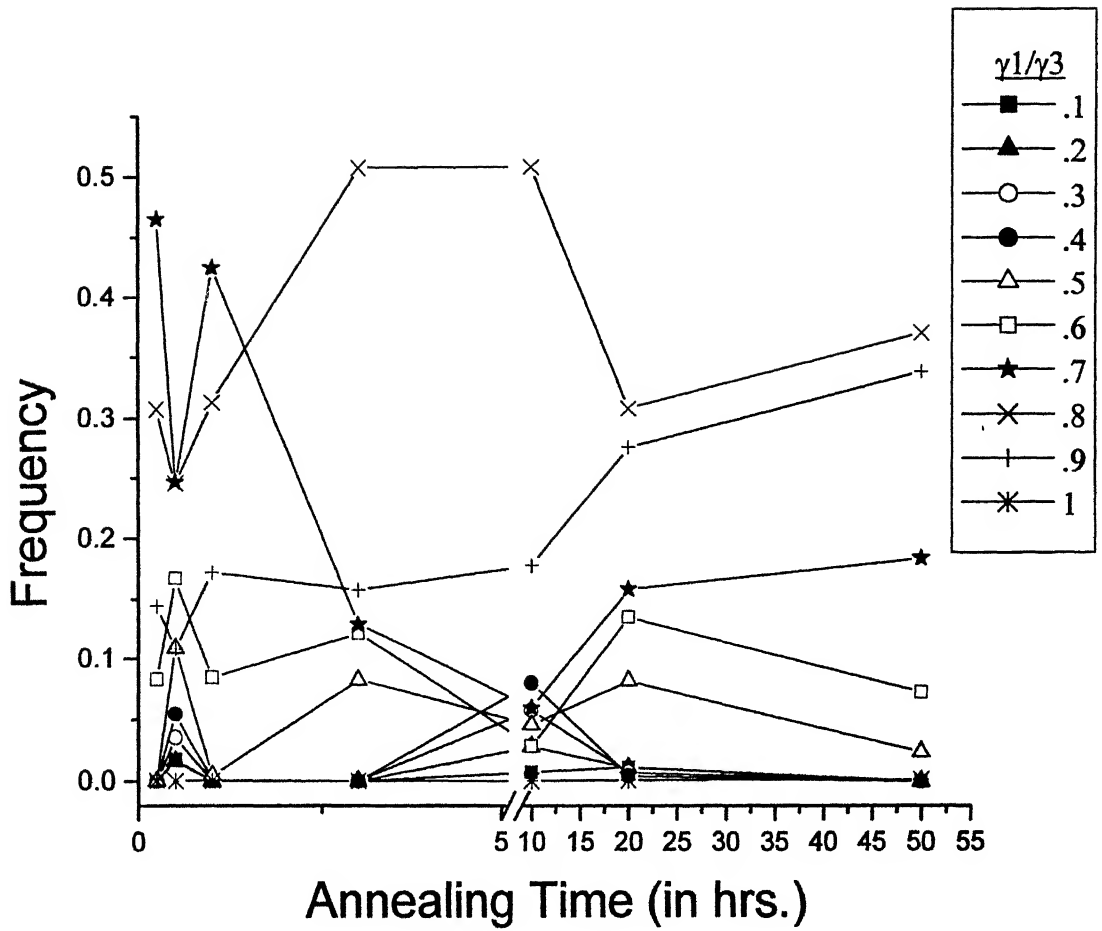


**Figure 4.34:** The variation of frequencies of different classes of  $\gamma_1/\gamma_3$  as a function of annealing time for Ni-10% Co samples.

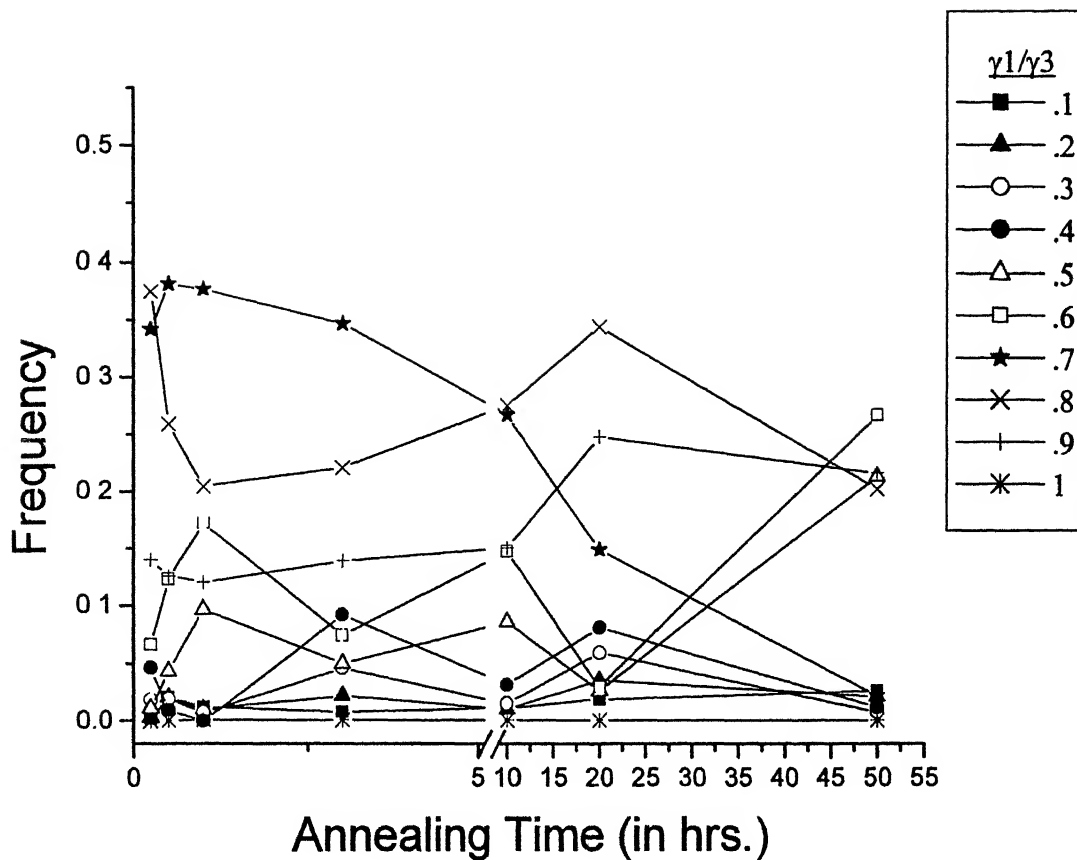


**Figure 4.35:** The variation of frequencies of different classes of  $\gamma_1/\gamma_3$  as a function of annealing time for Ni-20% Co samples.

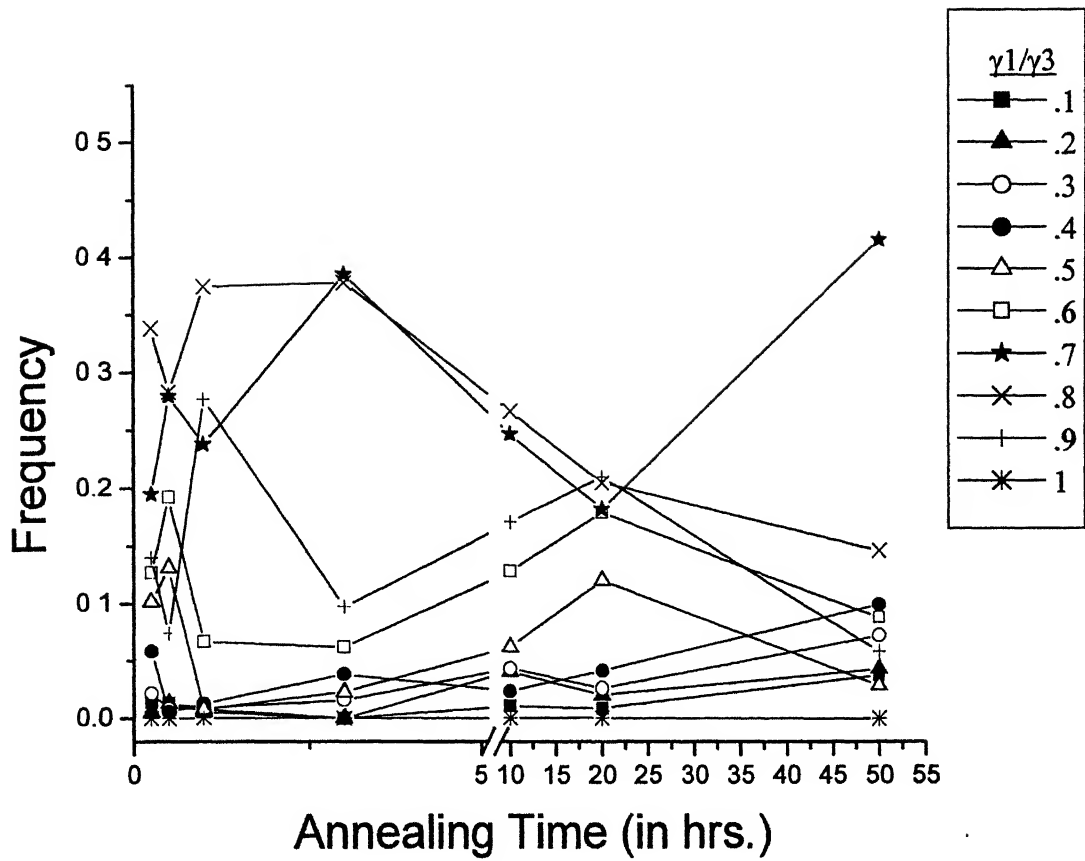


**Figure 4.36:** The variation of frequencies of different classes of  $\gamma_1/\gamma_3$  as a function of annealing time for Ni-30% Co samples.

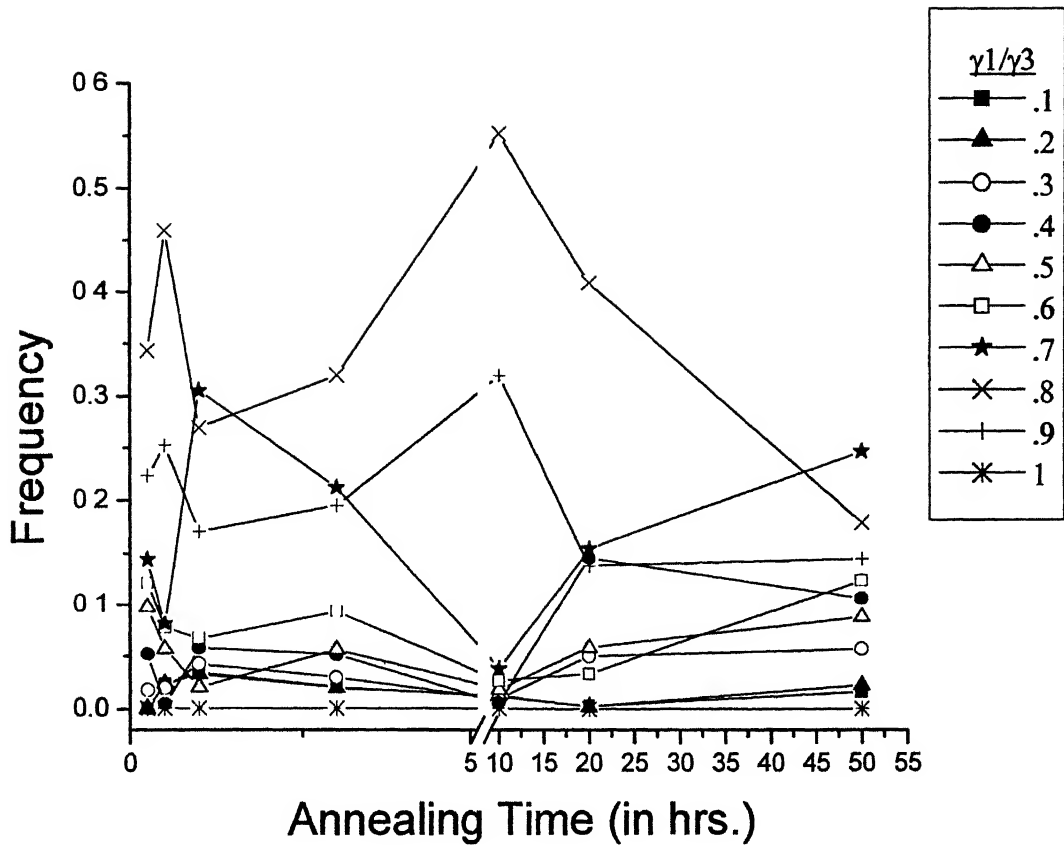


**Figure 4.37:** The variation of frequencies of different classes of  $\gamma_1/\gamma_3$  as a function of annealing time for Ni-40% Co samples.

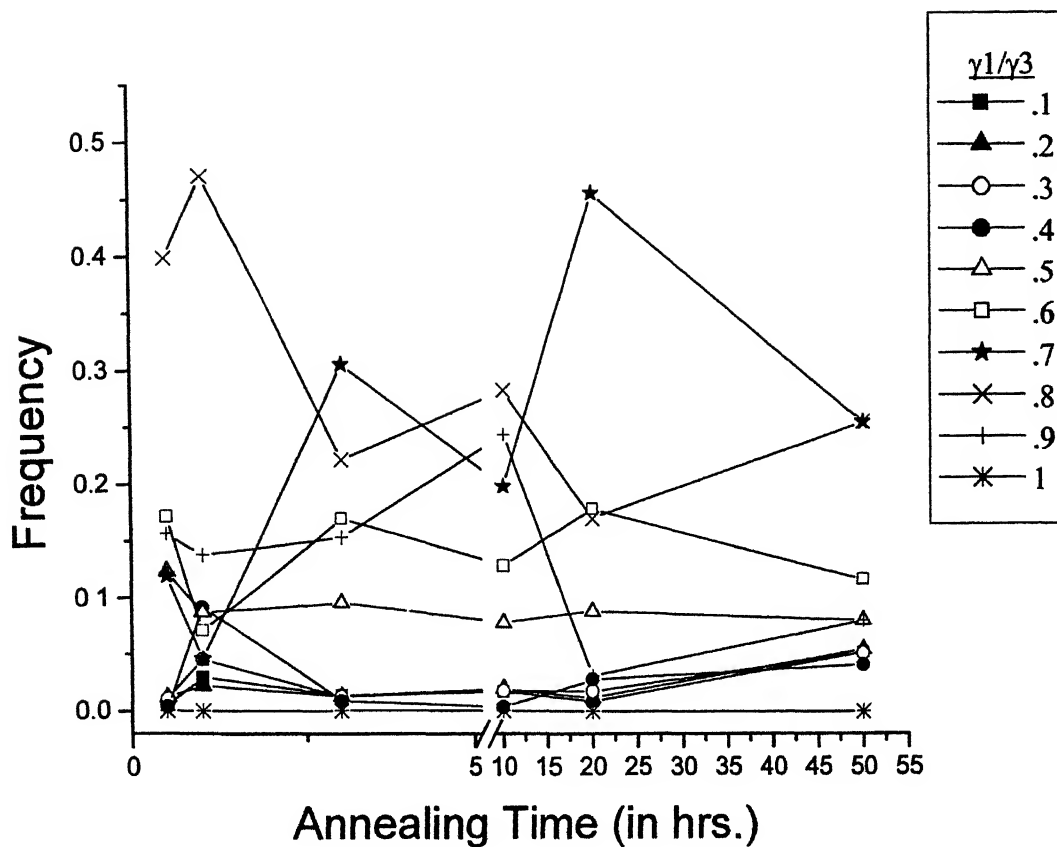


**Figure 4.38:** The variation of frequencies of different classes of  $\gamma_1/\gamma_3$  as a function of annealing time for Ni-60% Co samples.



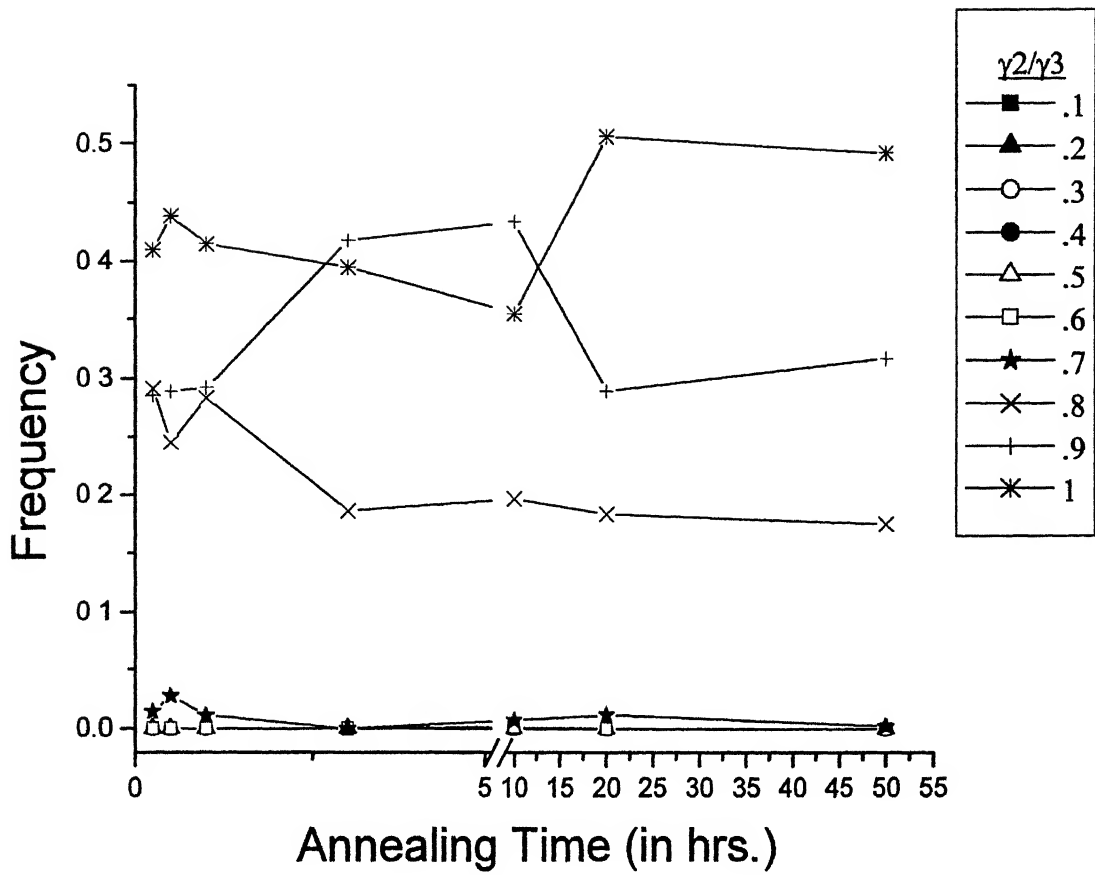


**Figure 4.39:** The variation of frequencies of different classes of  $\gamma_2/\gamma_3$  as a function of annealing time for Ni-10% Co samples.

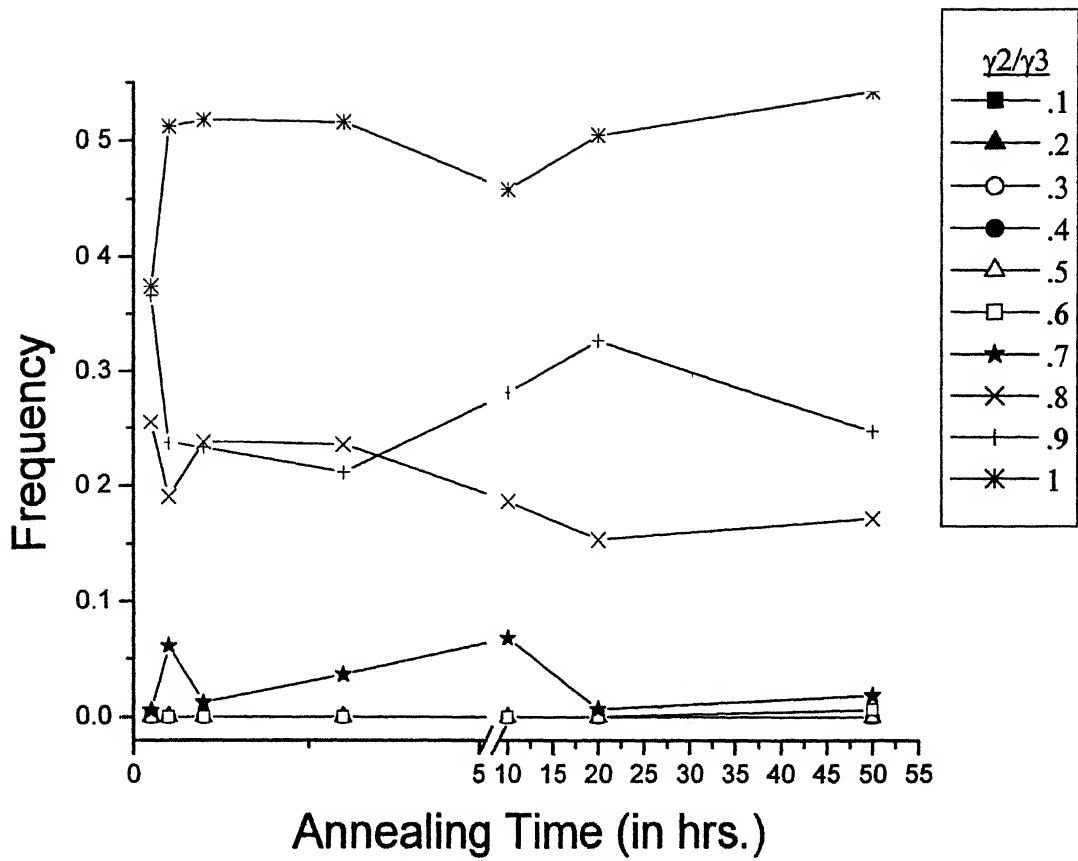


**Figure 4.40:** The variation of frequencies of different classes of  $\gamma_2/\gamma_3$  as a function of annealing time for Ni-20% Co samples.

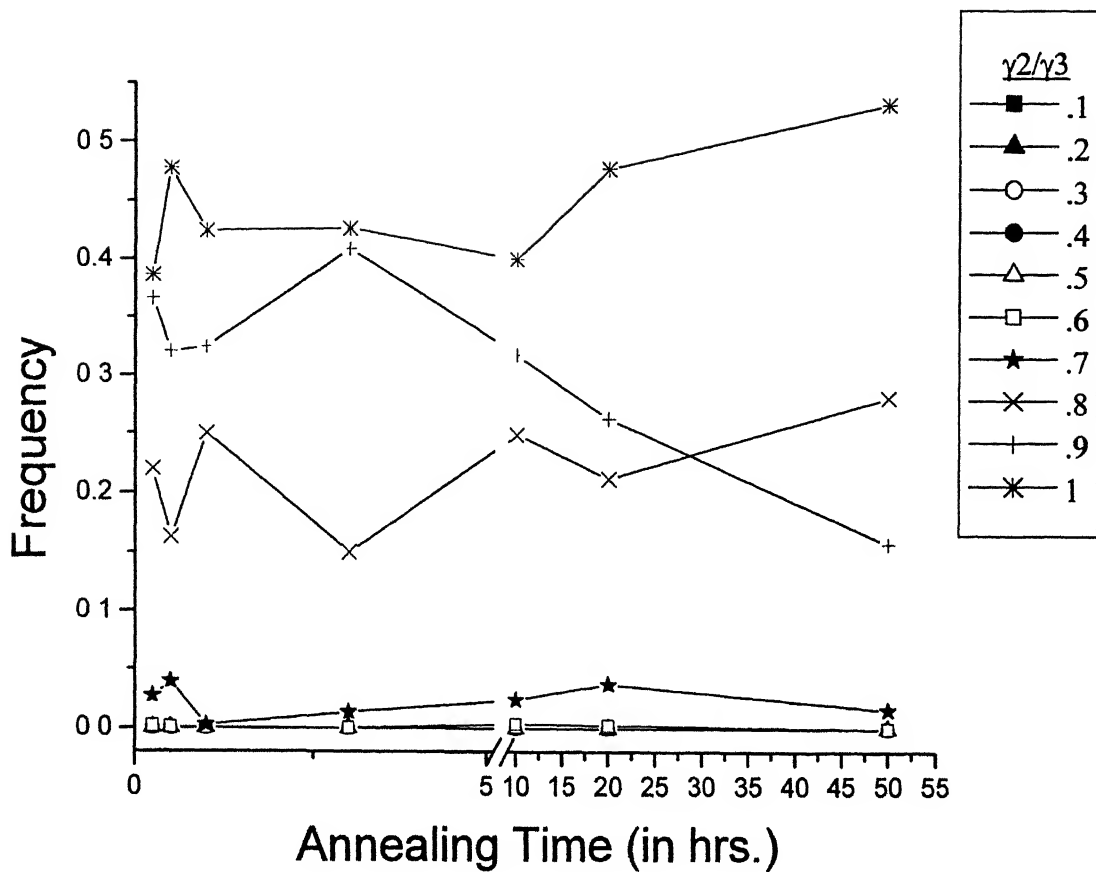


**Figure 4.41:** The variation of frequencies of different classes of  $\gamma_2/\gamma_3$  as a function of annealing time for Ni-30% Co samples.

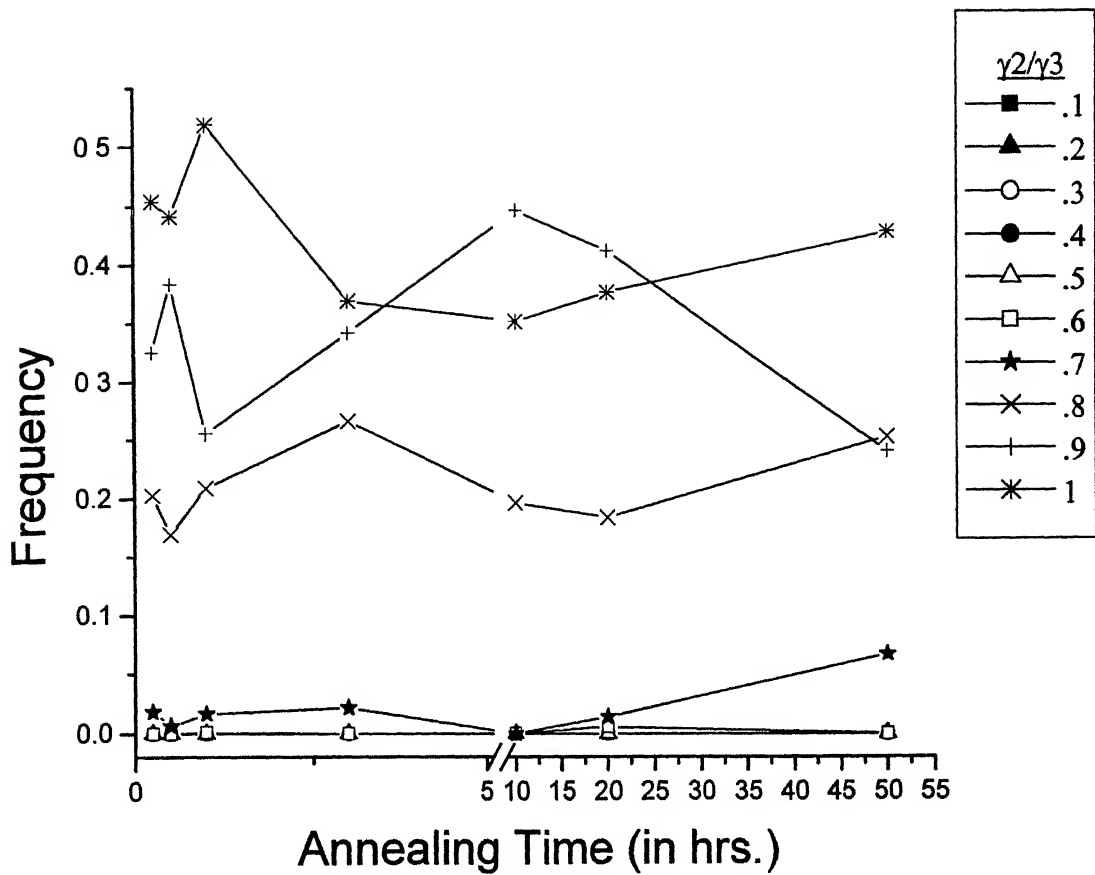


**Figure 4.42:** The variation of frequencies of different classes of  $\gamma_2/\gamma_3$  as a function of annealing time for Ni-40% Co samples.

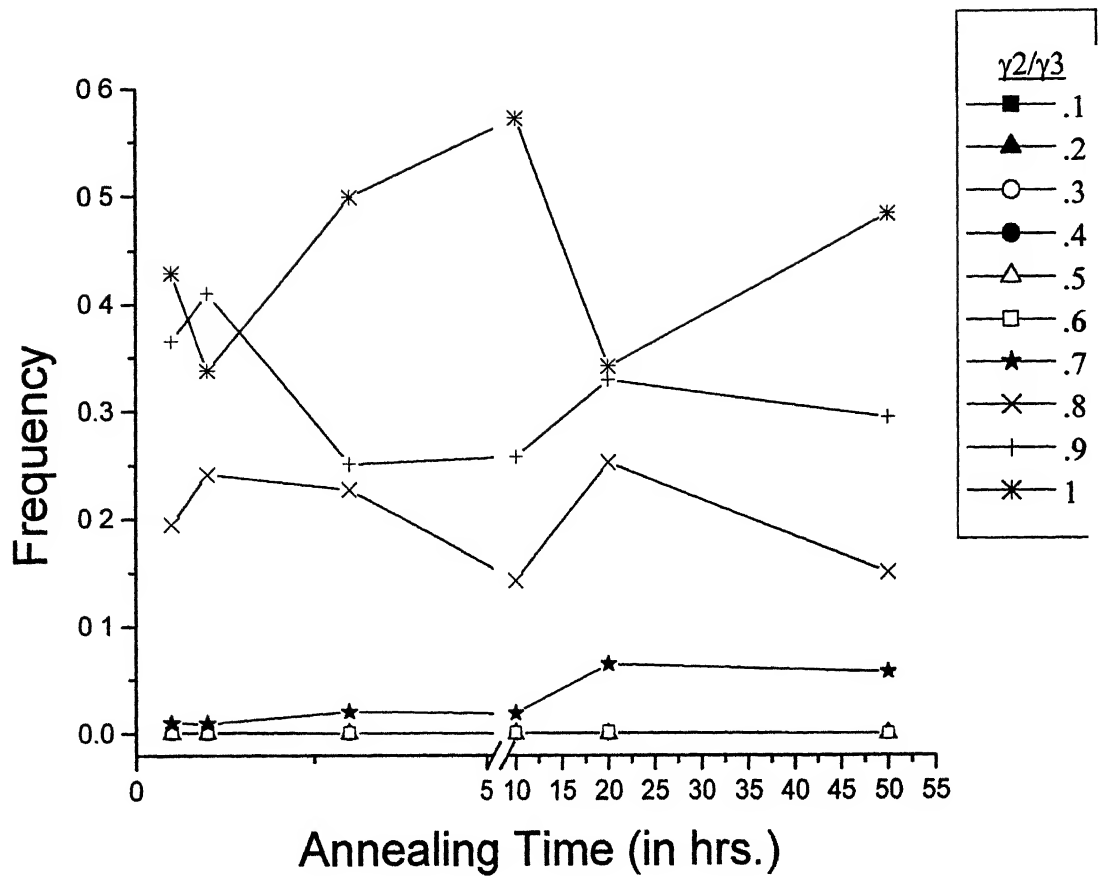


**Figure 4.43:** The variation of frequencies of different classes of  $\gamma_2/\gamma_3$  as a function of annealing time for Ni-60% Co samples.

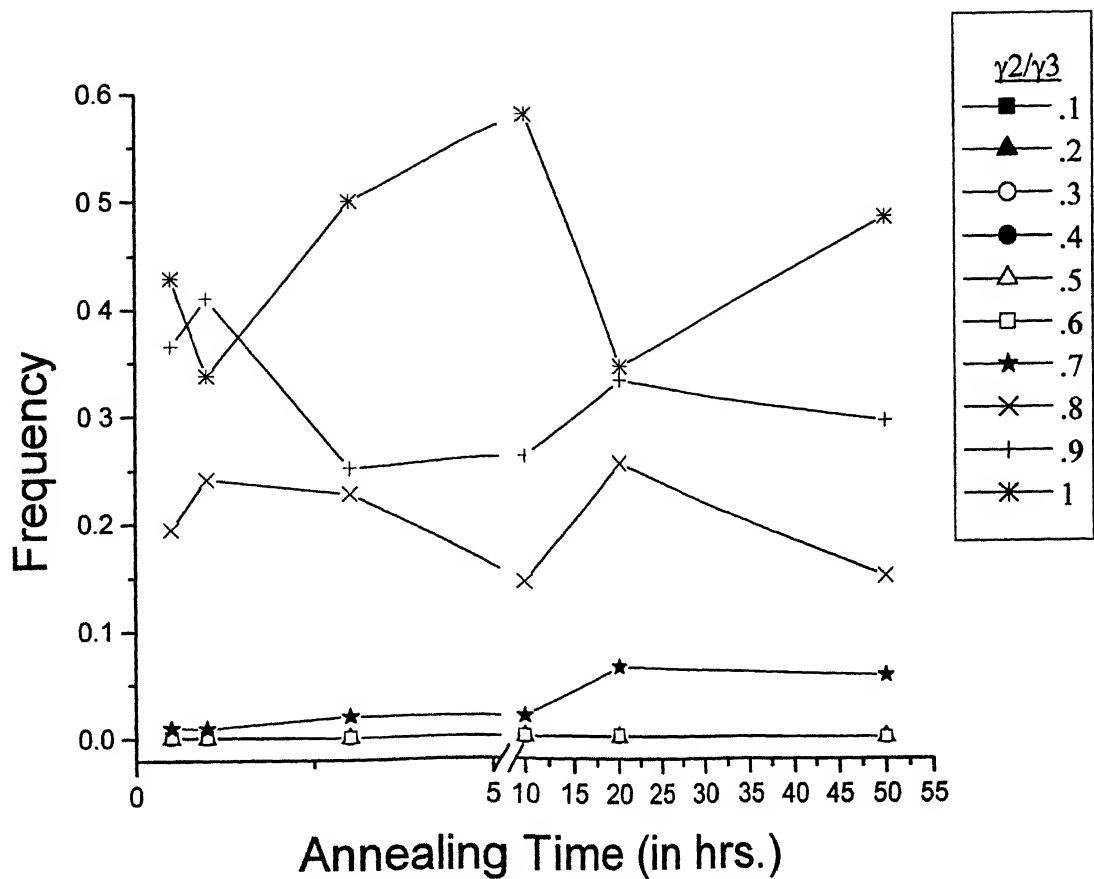


**Figure 4.43:** The variation of frequencies of different classes of  $\gamma_2/\gamma_3$  as a function of annealing time for Ni-60% Co samples.

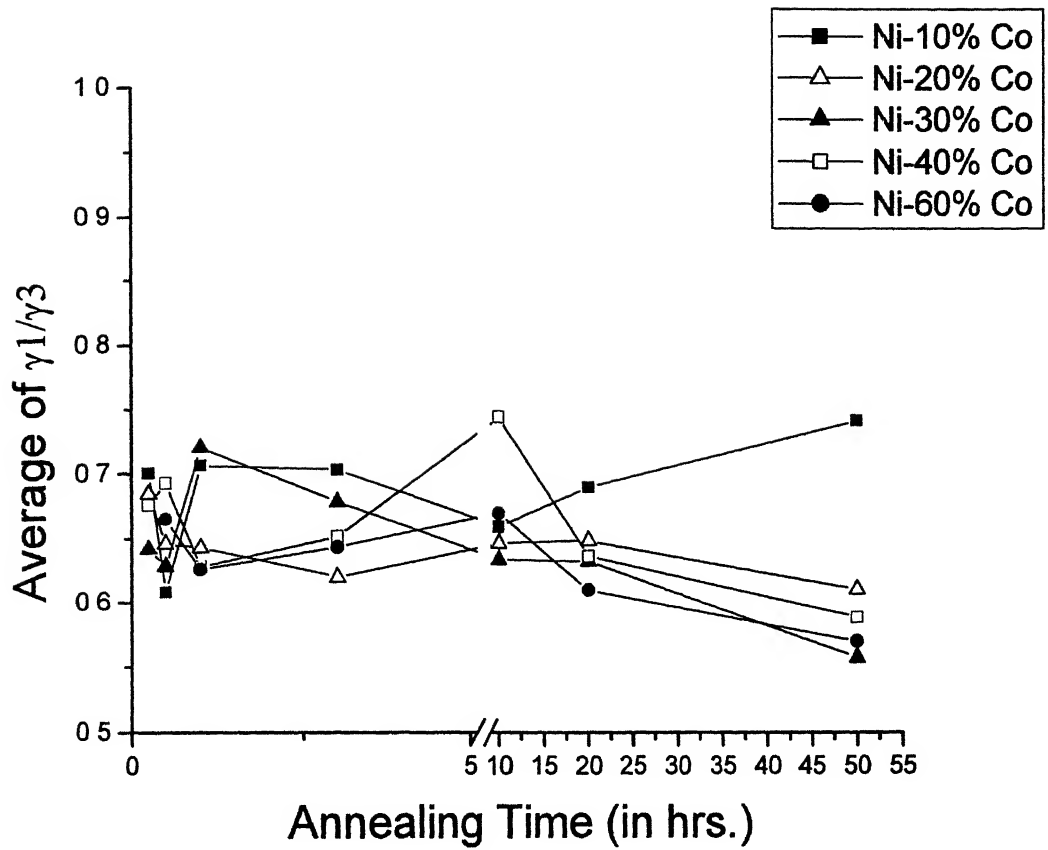


**Figure 4.44:** The variation of mean of relative energy ratio  $\gamma_1/\gamma_3$  of different alloys as a function of annealing time.

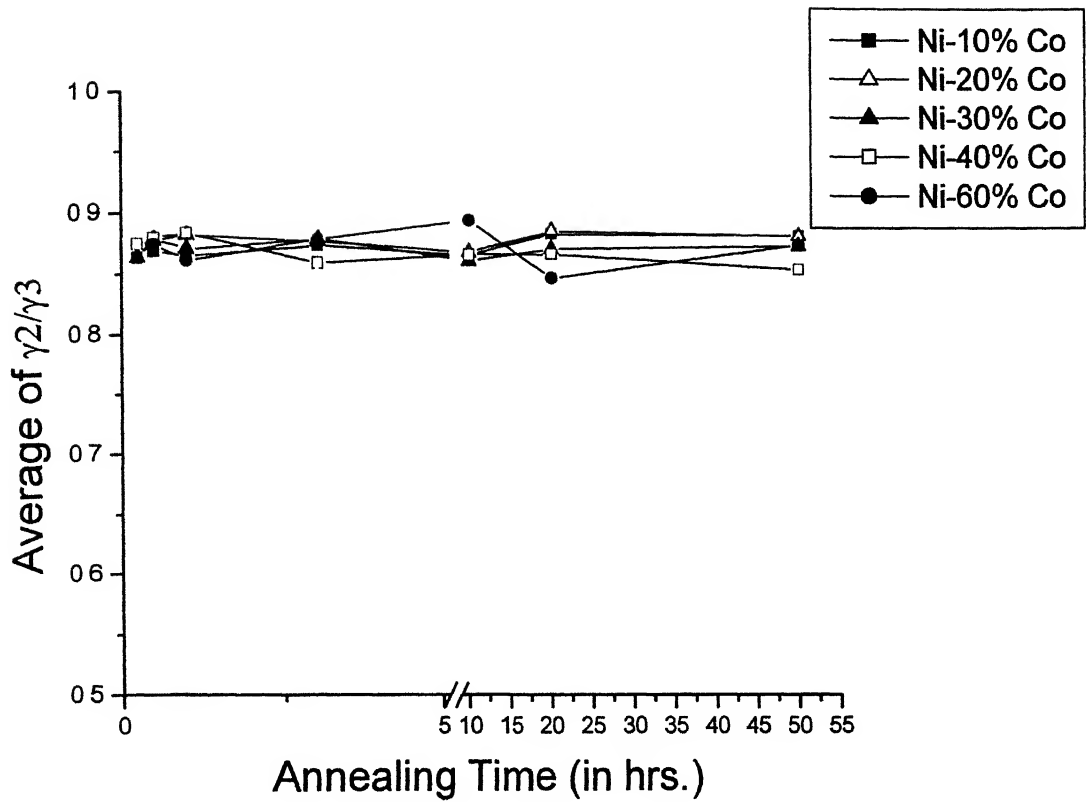


**Figure 4.45:** The variation of mean of relative energy ratio  $\gamma_2/\gamma_3$  of different alloys as a function of annealing time.



indicates that it has reached more near towards equilibrium than the other alloys. In the  $\gamma_2/\gamma_3$  plots there is hardly any variation among the alloys.

#### **4.2.5: COEFFICIENT OF VARIATION vs. ANNEALING TIME**

For the purpose of comparison, the coefficient of variation (i.e., standard deviation/mean) of  $\gamma_1/\gamma_3$  and  $\gamma_2/\gamma_3$  as a function of annealing time are plotted in **Figure 4.46 and 4.47** respectively. In case of  $\gamma_1/\gamma_3$  there is a significant scatter of coefficient of variation. In contrast to  $\gamma_1/\gamma_3$ , the fluctuation of coefficient of variation is less for  $\gamma_2/\gamma_3$ . This is quite expected, as the dihedral angles become closer to each other and the grain boundary energy variation also reduces.

#### **4.3: TEXTURE RESULTS**

The various texture components in different alloys for different annealing times are given in **Tables 4.1 to 4.30**. From the tables it can be observed that in the samples of Ni-10% Co, Ni-20% Co, and Ni-30% Co the cube component  $\{100\}\langle 001 \rangle$  is predominantly present. Along with cube component its twin components are also present. The first generation twin of cube is represented as CT1  $\{212\}\langle 122 \rangle$  and second generation twins of cube are represented as CT2  $\{148\}\langle 841 \rangle$  and  $\{148\}\langle 474 \rangle$ . In Ni-40% Co alloy, cube component is present in little amount. In Ni-10% Co, Ni-20% Co, and Ni-30% Co alloys a component  $\{437\}\langle 4\ 11\ 7 \rangle$  which is near to first generation twin of Bs recrystallisation component (BsT) is also present consistently. In Ni-40% Co alloy three components are important: Bs recrystallisation component (BsR)  $\{236\}\langle 385 \rangle$ ,  $\{279\}\langle 7\ 11\ 7 \rangle$ , and the retained S component  $\{123\}\langle 634 \rangle$ . In Ni-60% Co alloy the primary components are rotated Goss component  $\{011\}\langle 110 \rangle$  and a component which is near to it i.e.  $\{011\}\langle 114 \rangle$ .

##### **4.3.1: VARIATION OF CUBE COMPONENT WITH ANNEALING TIME IN Ni-10% Co TO Ni-40% Co ALLOY**

The variations of intensity and volume fraction of cube component as a function of annealing time for different alloys are shown in **Figures 4.48 and 4.49** respectively. The intensity of cube component in both Ni-30% Co and Ni-40% Co alloys do not vary much and remains nearly the same for almost all annealing times. Although Ni-10% Co and Ni-20% Co show larger variation at the initial period of annealing time, after 20 hours of annealing the intensity of all the alloys become steady. In case of volume fraction of cube component upto 10 hours of annealing time there are some

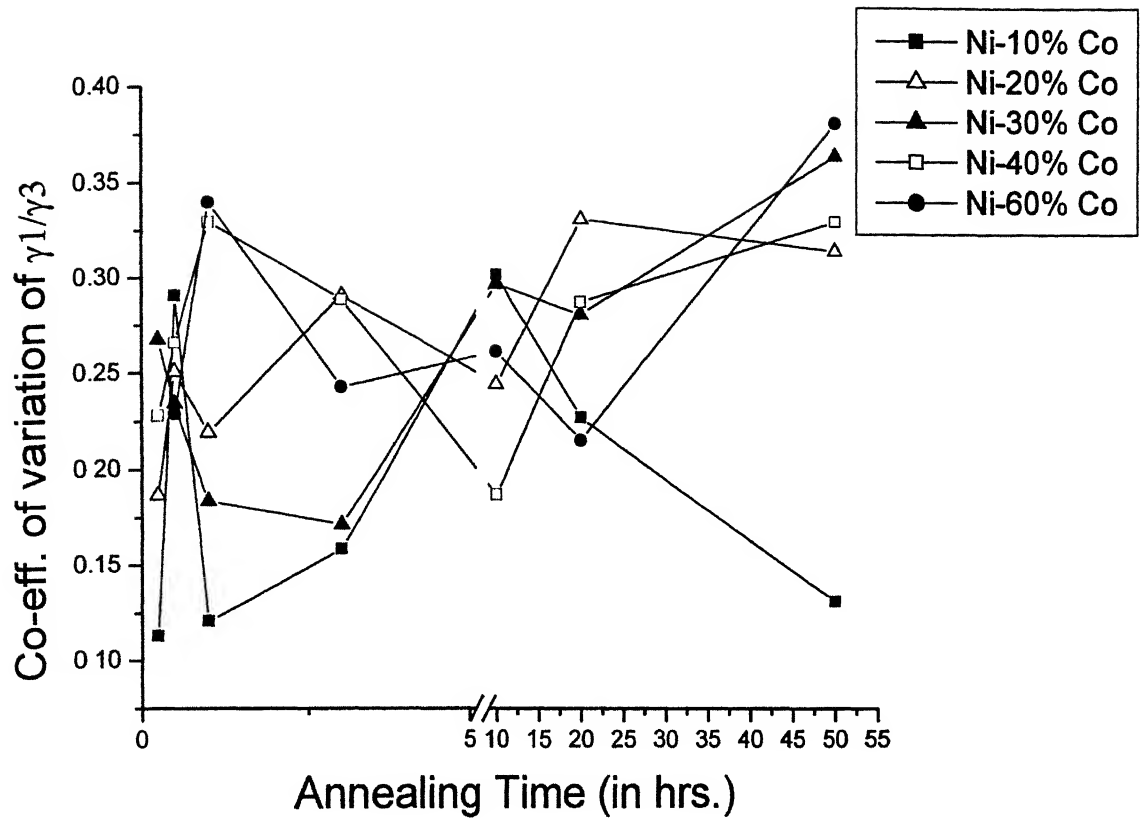


**Figure 4.46:** The variation of co-efficient of variation of relative energy ratio  $\gamma_1/\gamma_3$  of different alloys as a function of annealing time.

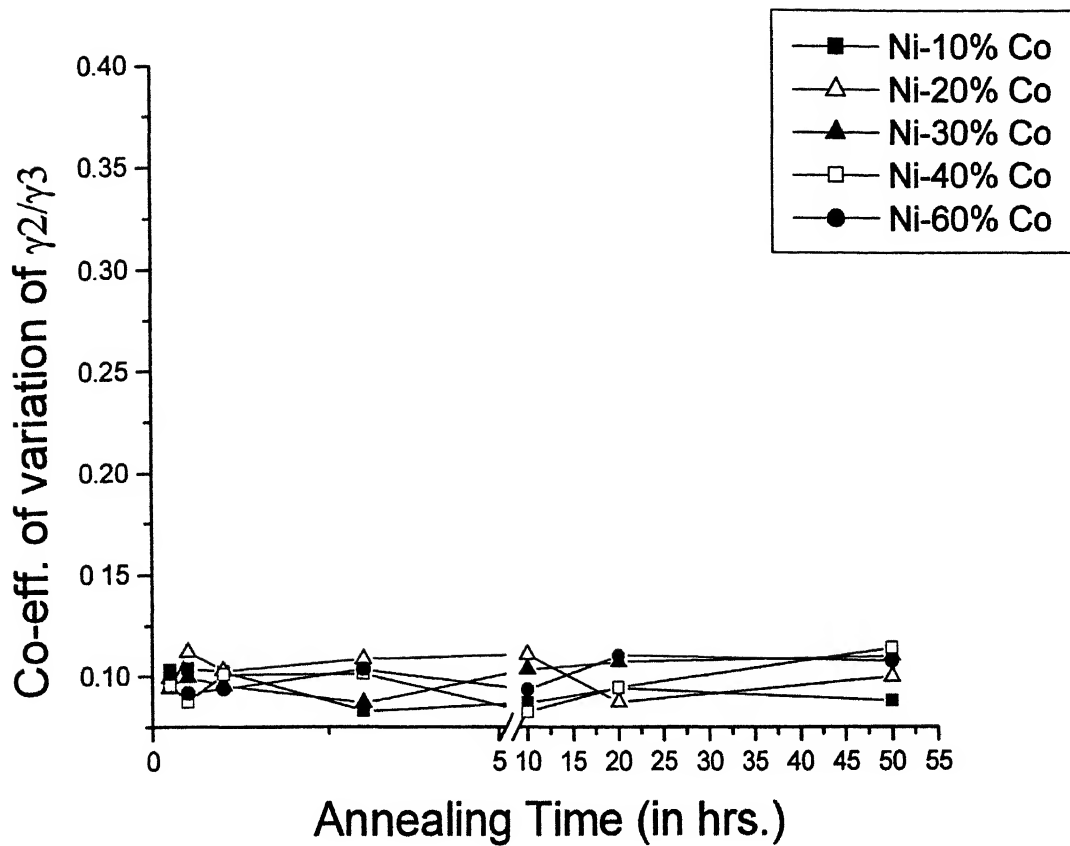


**Figure 4.47:** The variation of co-efficient of variation of relative energy ratio  $\gamma_2/\gamma_3$  of different alloys as a function of annealing time.

**Table: 4.1:** Ni-10% Co annealed at 800°C for 15 minutes.

Serial No.	Component ID	Euler Angles			f(g)	Volume %
		$\phi_1$	$\phi$	$\phi_2$		
1	Rotated Cube	0	34.4	0	3.53	6.59
2	Cube	0	0.4	0	19.25	29.36
3	CT1	66.6	45.8	62.6	6.76	30.08
4	Near to Bs Rex. T1	61.2	35.1	50	2.6	14.7
5	CT2	74.4	28.9	75	2.3	10.55
6	CT2	14.7	25.7	10	2.3	7.95

**Table: 4.2:** Ni-10% Co annealed at 800°C for 1 hr.

Serial No.	Component ID	Euler Angles			f(g)	Volume %
		$\phi_1$	$\phi$	$\phi_2$		
1	Rotated Cube	0	30.7	0	4.1	6.57
2	Cube	0	0.4	0	23.22	41.62
3	CT1	65	44.6	62.8	5.62	21.22
4	Near to Bs Rex. T1	61.2	36	55	5.1	18
5	CT2	15.3	25.2	10	2.4	5.33
6	CT2	71.1	29.1	75	2	5.76

**Table: 4.3:** Ni-10% Co annealed at 800°C for 3 hr.

Serial No.	Component ID	Euler Angles			f(g)	Volume %
		$\phi_1$	$\phi$	$\phi_2$		
1	Rotated Cube	0.5	25.9	0	4.36	5.11
2	Cube	0	0.4	0	32.59	45.66
3	CT1	64.2	45.2	61.8	7.02	18.53
4	Near to Bs Rex. T1	60.8	35.8	55	6	14.41
5	CT2	71.4	30.6	75	2.3	9.78
6	CT2	15.3	25.5	10	2.6	3.59

**Table: 4.4:** Ni-10% Co annealed at 800°C for 10 hr.

Serial No.	Component ID	Euler Angles			f(g)	Volume %
		$\phi_1$	$\phi$	$\phi_2$		
1	Rotated Cube	0	25.4	0	5.12	5.09
2	Cube	0	0.5	0	27.76	42.81
3	Near Bs Rex. T1	58.3	35.8	57.5	4.98	21.46
4	CT1	65.3	44.4	60	5.33	20.4
5	CT2	16.4	25.7	10	2.5	3.79
6	CT2	74.2	30.1	75	2.2	3.93

**Table: 4.5:** Ni-10% Co annealed at 800°C for 20 hr.

Serial No.	Component ID	Euler Angles			f(g)	Volume %
		$\phi_1$	$\phi$	$\phi_2$		
1	Cube	0	0.4	0	34.56	44.71
2	CT2	15.7	26.7	11.9	2.88	9.96
3	Near to Bs Rex. T1	60.4	35.1	55.6	5.84	22.57
4	CT1	65	45	61.8	7.07	14.1
5	Goss	0	45	0	4.5	1.48
6	CT2	70.8	29.9	75	2.6	4
7	Rotated Cube	0	28.5	0	4.5	2.06

**Table: 4.6:** Ni-10% Co annealed at 800°C for 50 hr.

Serial No.	Component ID	Euler Angles			f(g)	Volume %
		$\phi_1$	$\phi$	$\phi_2$		
1	Rotated Cube	0	25.1	0	5.8	6.06
2	Cube	0	0.4	0	32.73	46.91
3	Goss	0	44	0	4.69	3.24
4	CT1	63.9	44.6	61.2	6.67	14.2
5	CT2	15.8	25.3	10	2.5	3.58
6	Near to Bs Rex. T1	65.6	35.1	50	4.6	15.94
7	CT2	71.2	29.5	75	2.5	7.94

**Table: 4.7:** Ni-20% Co annealed at 800°C for 15 minutes.

Serial No.	Component ID	Euler Angles			f(g)	Volume %
		$\phi_1$	$\phi$	$\phi_2$		
1	Rotated Cube	0	30.8	0	3	7.11
2	CT2	19.2	25.6	5	2.43	18.69
3	Cube	0	0.3	0	12.47	17.82
4	CT1	65.1	44.8	63.1	4.74	24.55
5	CT2	74.5	29.4	75	2.23	23.17
6	Near to Bs Rex. T1	65.7	35	50	2.5	7.78

**Table: 4.8:** Ni-20% Co annealed at 800°C for 1 hr.

Serial No.	Component ID	Euler Angles			f(g)	Volume %
		$\phi_1$	$\phi$	$\phi_2$		
1	Rotated Cube	0	25.7	0	5.29	4.53
2	Cube	0	0.4	0	38.75	48.63
3	Goss	0	45	0	5.18	1.81
4	Near to Bs Rex. T1	58.6	35.6	57.4	7.56	9.18
5	CT1	64.2	44.1	60	7.68	12.22
6	CT2	16.1	25.8	10	3.1	3.93
7	CT2	74.8	29.5	75	2.7	3.55
8	Bs Rex.	74.1	31.2	40	3.9	8.26
9	{416}<121>	46	36.5	70	3.9	4.92

**Table: 4.9:** Ni-20% Co annealed at 800°C for 3 hr.

Serial No.	Component ID	Euler Angles			f(g)	Volume %
		$\phi_1$	$\phi$	$\phi_2$		
1	Rotated Cube	0	24.8	0	3.59	6.26
2	Goss	0	45	0	2.77	2
3	Cube	0	0.3	0	18.89	31.16
4	Near Bs Rex. T1	60.1	35.8	58.2	6.29	48.39
5	CT1	60	45	65	4.4	3.01
6	CT2	15.4	24.8	10	1.9	3.23
7	CT2	70.7	30.1	75	2.1	4.84

**Table: 4.10:** Ni-20% Co annealed at 800°C for 10 hr.

Serial No.	Component ID	Euler Angles			f(g)	Volume %
		$\phi_1$	$\phi$	$\phi_2$		
1	Cube	0	0.4	0	31.97	47.07
2	CT1	64.4	44.9	61.3	7.68	17.52
3	Goss	0	45	0	4.2	1.88
4	Near to Bs Rex. T1	65.5	35.1	50	5.1	20.13
5	CT2	16.1	25.6	10	2.8	4.87
6	CT2	71.1	29.1	75	2.4	6.56

**Table: 4.11:** Ni-20% Co annealed at 800°C for 20 hr.

Serial No.	Component ID	Euler Angles			f(g)	Volume %
		$\phi_1$	$\phi$	$\phi_2$		
1	Rotated Cube	0	25.8	0	6.25	2.62
2	Goss	0	45	0	6.86	1.42
3	Cube	0	0.4	0	51.51	49.89
4	CT2	15.3	28.6	13.2	3.48	4.12
5	Near to Bs Rex. T1	58.6	35.4	57.2	8.6	7.52
6	CT1	64.5	44.6	60	9.22	12.54
7	CT2	71.3	30.5	75	3	5.21
8	Bs Rex.	73.1	30.6	40	3.5	9.84
9	{416}<121>	46.2	35.7	70	4.2	4.26

**Table: 4.12:** Ni-20% Co annealed at 800°C for 50 hr.

Serial No.	Component ID	Euler Angles			f(g)	Volume %
		$\phi_1$	$\phi$	$\phi_2$		
1	Rotated Cube	0	26	0	4.09	1.85
2	Cube	0	0.4	0	33.37	43.07
3	Goss	0	45	0	3.9	1.75
4	CT1	64.5	42.4	58.7	7.46	28.74
5	CT2	15.5	26.1	10	2.4	3.09
6	Near to Bs Rex. T1	65.4	34.8	50	6.2	13.41
7	CT2	70.7	29.5	75	2.2	6.11

**Table: 4.13:** Ni-30% Co annealed at 800°C for 15 minutes.

Serial No.	Component ID	Euler Angles			f(g)	Volume %
		$\phi_1$	$\phi$	$\phi_2$		
1	Rotated Cube	0	30.4	0	3.13	7.4
2	CT2	16	25.9	3.6	2.28	15.38
3	Cube	0	0.4	0	9.53	15.94
4	{019}<991>	45	0	0	0.56	3.54
5	Near to Bs Rex. T1	61.1	35.6	55	3.26	15.81
6	CT1	65.8	44.5	63.2	3.9	10.73
7	CT2	71.2	31	70	2.34	22.75
8	{416}<121>	44.8	39.8	75	1.94	5.86

**Table: 4.14:** Ni-30% Co annealed at 800°C for 1 hr.

Serial No.	Component ID	Euler Angles			f(g)	Volume %
		$\phi_1$	$\phi$	$\phi_2$		
1	{0 6 11}<0 11 6>	90	34	0	2.33	3.59
2	Rotated Cube	0	25.4	0	2.7	2.13
3	Goss	0	45	0	2.51	2.05
4	Cube	0	0.4	0	11.75	14.35
5	CT2	20.3	19	0	2.27	5.9
6	Near to Bs Rex. T1	64.7	34.7	53.6	6.24	48
7	Bs Rex. T1	31.8	41.1	75	1.93	10.58
8	CT2	71.1	30.5	70	2.6	7.2
9	CT1	65	42	65	3	3.99

**Table: 4.15:** Ni-30% Co annealed at 800°C for 3 hr.

Serial No.	Component ID	Euler Angles			f(g)	Volume %
		$\phi_1$	$\phi$	$\phi_2$		
1	Rotated Cube	0	25.5	0	3.49	3.56
2	Cube	0	0.4	0	15.97	24.74
3	Near to Bs Rex. T1	60.8	35.3	56.1	7.34	28.69
4	Goss	0	45	0	2.4	1.9
5	Rotated Cube	0	25	0	3.5	1.78
6	Bs Rex. T1	31.9	40	75	1.9	6.57
7	CT2	75	30	75	2.1	24.26
8	CT1	60	40	65	4.6	7.78



**Table: 4.16:** Ni-30% Co annealed at 800°C for 10 hr.

Serial No.	Component ID	Euler Angles			f(g)	Volume %
		$\phi_1$	$\phi$	$\phi_2$		
1	Rotated Cube	0	26.3	0	3.17	2.95
2	Cube	0	0.5	0	15.31	23.4
3	Goss	0	45	0	2.35	1.79
4	Near to Bs Rex. T1	59	35	57.3	6.69	42.39
5	CT2	75.4	30.5	70	2	14.4
6	CT2	14.6	25.9	10	1.6	6.6
7	CT1	55	40	65	5.2	7.56

**Table: 4.17:** Ni-30% Co annealed at 800°C for 20 hr.

Serial No.	Component ID	Euler Angles			f(g)	Volume %
		$\phi_1$	$\phi$	$\phi_2$		
1	Rotated Cube	0	25.3	0	3.2	3.99
2	Goss	0	45	0	3.31	1.66
3	Cube	0	0.5	0	19.84	25.72
4	Near to Bs Rex. T1	61.6	35	54.6	8.01	33.51
5	CT1	60	45	65	4.7	5.57
6	CT2	70	30	75	2.1	23.2
7	CT2	16	26.7	10	1.9	4.85

**Table: 4.18:** Ni-30% Co annealed at 800°C for 50 hr.

Serial No.	Component ID	Euler Angles			f(g)	Volume %
		$\phi_1$	$\phi$	$\phi_2$		
1	Rotated Cube	0	28.3	0	3.62	3.95
2	Cube	0	0.4	0	17.55	27.47
3	Goss	0	43.9	0	2.76	2.16
4	Near to Bs Rex. T1	59.3	35.5	56.7	6.07	42.56
5	CT1	60	45	65	4.4	10.53
6	CT2	14.5	25.6	10	2.1	3.23
7	CT2	74.3	30	75	2.6	8.31

**Table: 4.19:** Ni-40% Co annealed at 800°C for 15 minutes.

Serial No.	Component ID	Euler Angles			f(g)	Volume %
		$\phi_1$	$\phi$	$\phi_2$		
1	Cube	0	0.5	0	2.57	3.17
2	{279}<7 11 7>	48.2	39.1	16.9	2.46	37.94
3	Cu	90	30.1	45	2.15	7.79
4	Near to S	58.7	35.4	61.8	1.98	7.94
5	Goss	0	45	0	1.93	2.07
6	{5 1 12}<171>	20.8	19.4	83.5	1.72	20.49
7	Rotated Cube	0.6	23.2	0	1.69	2.26
8	Near to S	60	35	60	2	17.23

**Table: 4.20:** Ni-40% Co annealed at 800°C for 1 hr.

Serial No.	Component ID	Euler Angles			f(g)	Volume %
		$\phi_1$	$\phi$	$\phi_2$		
1	{279}<7 11 7>	49.9	37.4	13.2	4.61	52.91
2	Cube	0	0.5	0	3.78	7.69
3	Goss	0	45	0	2.5	3.94
4	Retained S	60.3	35.3	60	2.1	7.62
5	Bs Rex.	70.3	33.3	50	2.3	16.65

**Table: 4.21:** Ni-40% Co annealed at 800°C for 3 hr.

Serial No.	Component ID	Euler Angles			f(g)	Volume %
		$\phi_1$	$\phi$	$\phi_2$		
1	Retained S	55.5	36.8	61.1	2.51	24.3
2	Goss	0	45	0	2.05	2.38
3	Cube	0	0.6	0	4.58	15.84
4	{279}<7 11 7>	49.9	39.2	13.2	4.25	43.72
5	Bs Rex.	69.4	34.4	50	2.1	12.31

**Table: 4.22:** Ni-40% Co annealed at 800°C for 10 hr.

Serial No.	Component ID	Euler Angles			f(g)	Volume %
		$\phi_1$	$\phi$	$\phi_2$		
1	Goss	4.8	45	0	2.3	5.9
2	Cube	0	0.6	0	3.3	9.95
3	{279}<7 11 7>	51.7	39.1	12.4	4.12	51.07
4	Retained S	64.2	35.8	60.2	2.34	16.88
5	Bs Rex.	75.5	33.2	45	2.18	14.49

**Table: 4.23:** Ni-40% Co annealed at 800°C for 20 hr.

Serial No.	Component ID	Euler Angles			f(g)	Volume %
		$\phi_1$	$\phi$	$\phi_2$		
1	Goss	0	45	0	2.37	4.33
2	Cube	0	0.5	0	3.93	7.02
3	{279}<7 11 7>	51.6	39.6	12.3	4.4	53.2
4	Retained S	62.9	35.3	57.4	2.71	20.57
5	Bs Rex.	69.9	34.2	50	2.6	13.16

**Table: 4.24:** Ni-40% Co annealed at 800°C for 50 hr.

Serial No.	Component ID	Euler Angles			f(g)	Volume %
		$\phi_1$	$\phi$	$\phi_2$		
1	Cube	0	0.7	0	5.62	11
2	{279}<7 11 7>	47.2	40.4	13.5	4.3	48.48
3	Retained S	60.9	38.2	59	2.7	6.46
4	Bs Rex.	70.7	34.3	45	2.34	23.03
5	Goss	0	45	0	2.6	9.77

**Table: 4.25:** Ni-60% Co annealed at 800°C for 15 minutes.

Serial No.	Component ID	Euler Angles			f(g)	Volume %
		$\phi_1$	$\phi$	$\phi_2$		
1	Goss	0	45	0	1.94	2.15
2	{0 4 11}<8 11 4>	56.1	21.1	0	1.95	32.02
3	Cu	90	28.6	45	4.63	22.76
4	Rotated Goss	90	35.8	0	4.9	36.66
5	Near to Bs	30	45	0	1.7	5.42

**Table: 4.26:** Ni-60% Co annealed at 800°C for 1 hr.

Serial No.	Component ID	Euler Angles			f(g)	Volume %
		$\phi_1$	$\phi$	$\phi_2$		
1	Near to rotated Goss	19.2	45	0.2	7.41	28.75
2	Rotated Goss	90	39.9	0	13.51	47.07
3	{011}<655>	54.1	38.8	10	2.2	4.55
4	Bs Rex. T1	33.6	41.6	75	4.2	2.07
5	Bs Rex.	81.2	33.7	30	4.7	17.9

**Table: 4.27:** Ni-60% Co annealed at 800°C for 3 hr.

Serial No.	Component ID	Euler Angles			f(g)	Volume %
		$\phi_1$	$\phi$	$\phi_2$		
1	Nearly rotated Goss	15.5	45	0.1	7.39	37.4
2	Rotated Goss	90	39.7	0	11.4	43.07
3	{011}<655>	49.4	38.1	10	2	3.59
4	Bs Rex. T1	34.5	41.8	75	3.9	2.69
5	Bs Rex.	81.3	34	30	3.3	13.2

**Table: 4.28:** Ni-60% Co annealed at 800°C for 10 hr.

Serial No.	Component ID	Euler Angles			f(g)	Volume %
		$\phi_1$	$\phi$	$\phi_2$		
1	Nearly rotated Goss	15.3	45	0	10.02	42.42
2	{011}<655>	44.8	35.6	3.2	2.28	25.28
3	Near to Bs Rex. T1	30	41.6	75	4.5	1.41
4	Rotated Goss	90	45	0	10.7	30.93

**Table: 4.29:** Ni-60% Co annealed at 800°C for 20 hr.

Serial No.	Component ID	Euler Angles			f(g)	Volume %
		$\phi_1$	$\phi$	$\phi_2$		
1	Rotated Goss	90	40	0	9.25	29.56
2	Nearly rotated Goss	15.1	45	0	9.63	23.4
3	{011}<655>	49.7	39.3	8.7	2.03	7.79
4	Near to Bs Rex. T1	34.2	41.5	75	4.29	24.99
5	Goss	0	40	0	5.5	6.45
6	Bs Rex.	85.3	33.1	30	2.4	7.93

**Table: 4.30:** Ni-60% Co annealed at 800°C for 50 hr.

Serial No.	Component ID	Euler Angles			f(g)	Volume %
		$\phi_1$	$\phi$	$\phi_2$		
1	Nearly rotated Goss	18.3	45	0	11.97	40.63
2	Rotated Goss	90	45	0	13.15	36.96
3	Goss	0	45	0	6.5	6.92
4	{011}<655>	49	40.2	5	2.2	3.17
5	Near to Bs Rex. T1	30.2	40.7	75	5.2	4.85
6	Bs Rex.	84.6	35.2	25	2.8	7.53

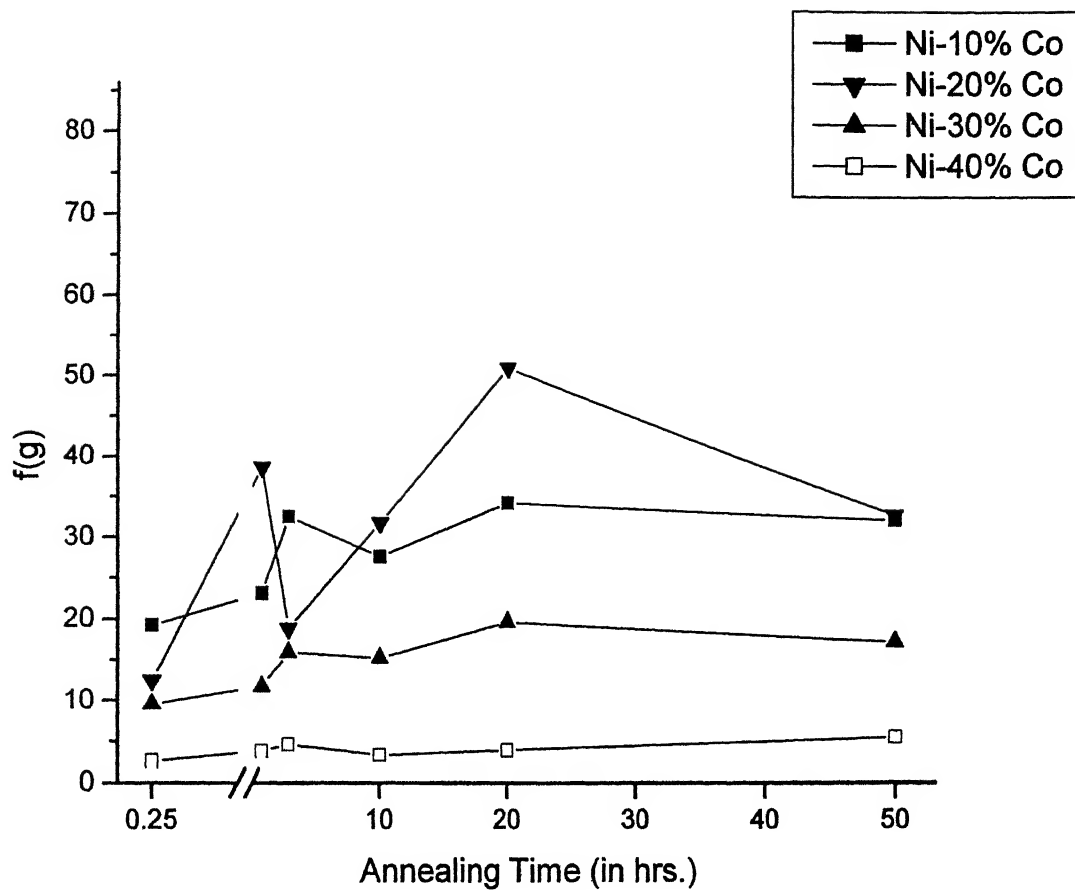


**Figure 4.48:** Variation of intensity of cube component as a function of annealing time for different samples.

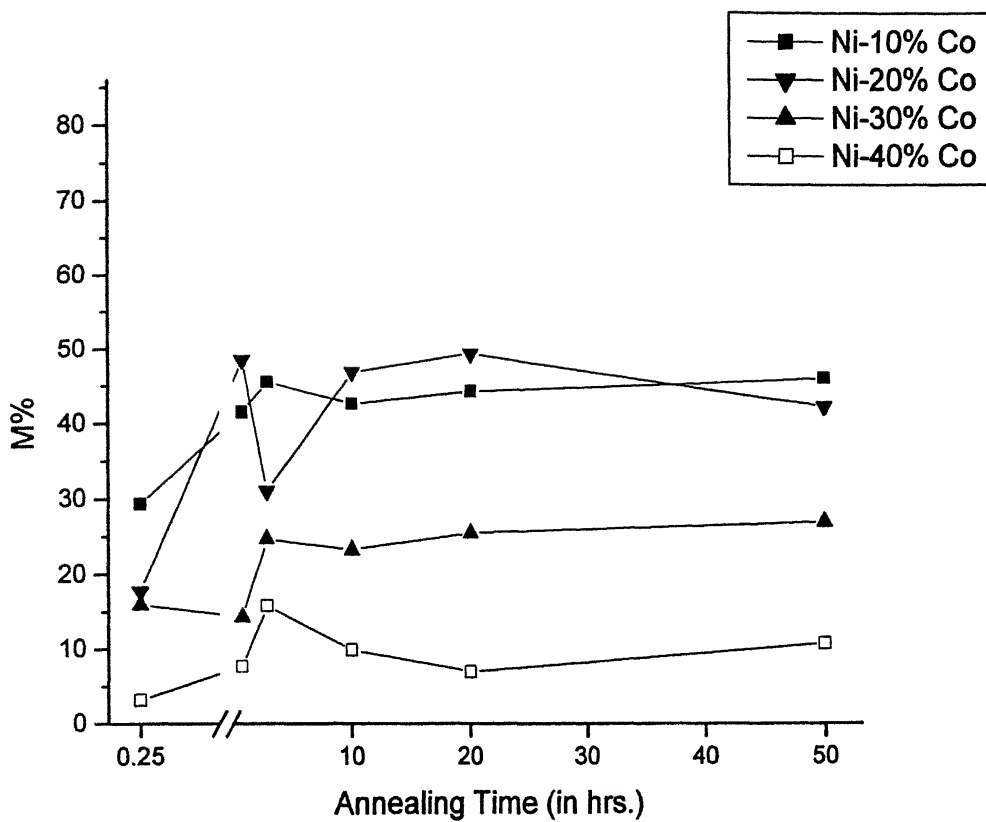


**Figure 4.49:** Variation of volume fraction of cube component as a function of annealing time for different samples.

change in all the four alloys. But after 10 hours of annealing time the volume fraction of cube component for all the samples becomes nearly constant.

The variation of intensity and volume fraction of cube component as a function of Co content for different annealing times are shown in **Figures 4.50 and 4.51** respectively. It can be observed from the figure that the intensity and volume fraction of the cube component decreases as the Co content is increased beyond 20 wt%.

#### **4.3.2: VARIATION OF CUBE COMPONENT AND ITS TWINS WITH ANNEALING TIME IN Ni-10% Co TO Ni-30% Co ALLOY**

The volume fractions of cube component and its twins, as a function of annealing time for different alloys, are shown in **Figure 4.52**. It can be observed from the figure that cube and its twin components constitute major volume fraction of samples. The volume fraction of cube and its twin component in Ni-10% Co possess almost 80% of the total volume from initial stages of annealing. Although there is no general trend for different samples but, if observed closely, it can be revealed that at the initial stages of annealing there is higher variation in volume fractions. With increasing annealing time the volume fraction become steady.

The volume fraction of cube component and its twins, as a function of Co content for different annealing times are shown in **Figure 4.53**. Generally the volume fraction of cube and its twin component decreases if Co content increases beyond 20 wt%.

#### **4.3.3: VARIATION OF BsT COMPONENT WITH ANNEALING TIME IN Ni-10% Co TO Ni-30% Co ALLOY**

The variation of intensity and volume fraction of the BsT component  $\{437\}\langle 4\ 11\ 7\rangle$  as a function of annealing time for different alloys is shown in **Figures 4.54 and 4.55** respectively. The intensity of this component is nearly constant with annealing time and is very low. But there is a wide variation of volume fraction of this component upto 20 hours of annealing time after which it attains a constant value for different samples. In case of Ni-30% Co this component constitute about more than 40% of volume after 20 hours of annealing time. But the intensity of this component was relatively small which indicates that this component is quite spread out.

#### **4.3.4: VARIATION OF MAJOR TEXTURE COMPONENTS WITH ANNEALING TIME IN Ni-40% Co ALLOY**

The major texture components of Ni-40% Co alloy are cube component, BsR component  $\{236\}\langle 385\rangle$ , retained S component  $\{123\}\langle 634\rangle$ , and the  $\{279\}\langle 7\ 11\ 7\rangle$  component. Among these we have discussed about the cube component earlier. The



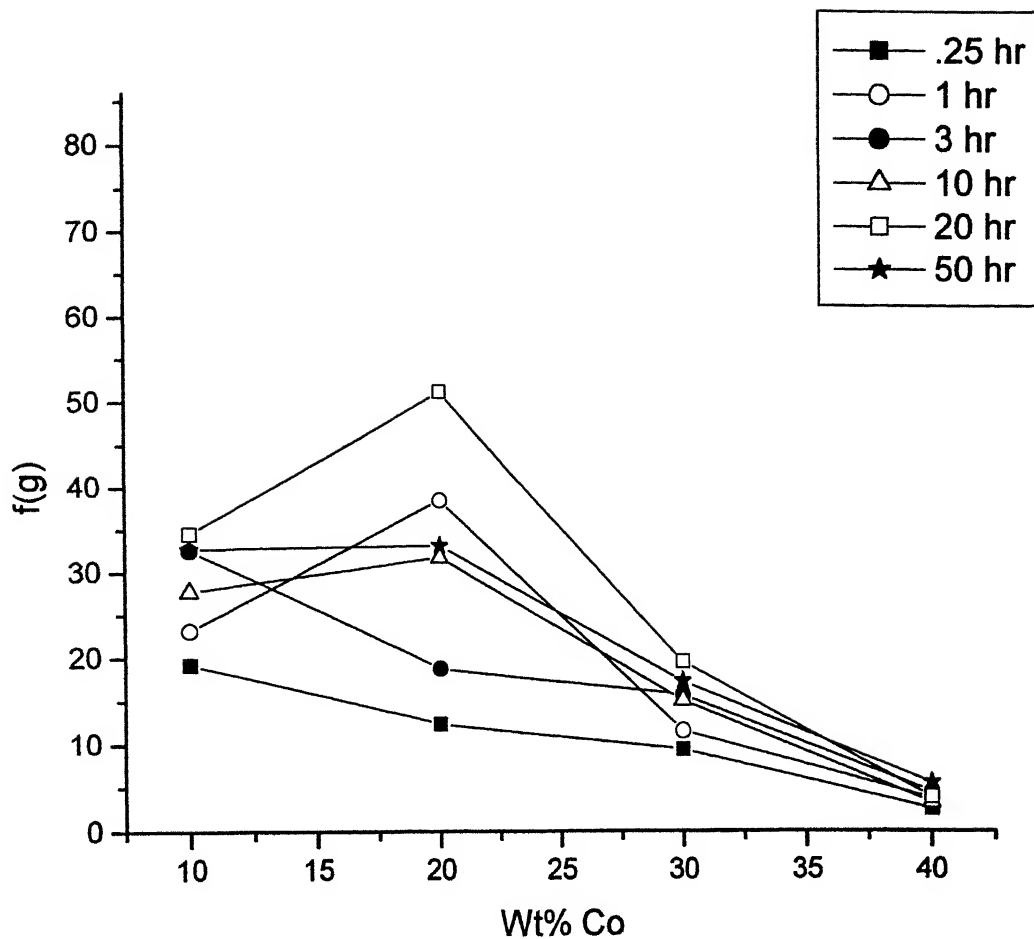


**Figure 4.50:** Variation of intensity of cube component as a function of Co content and subjected to different annealing times.

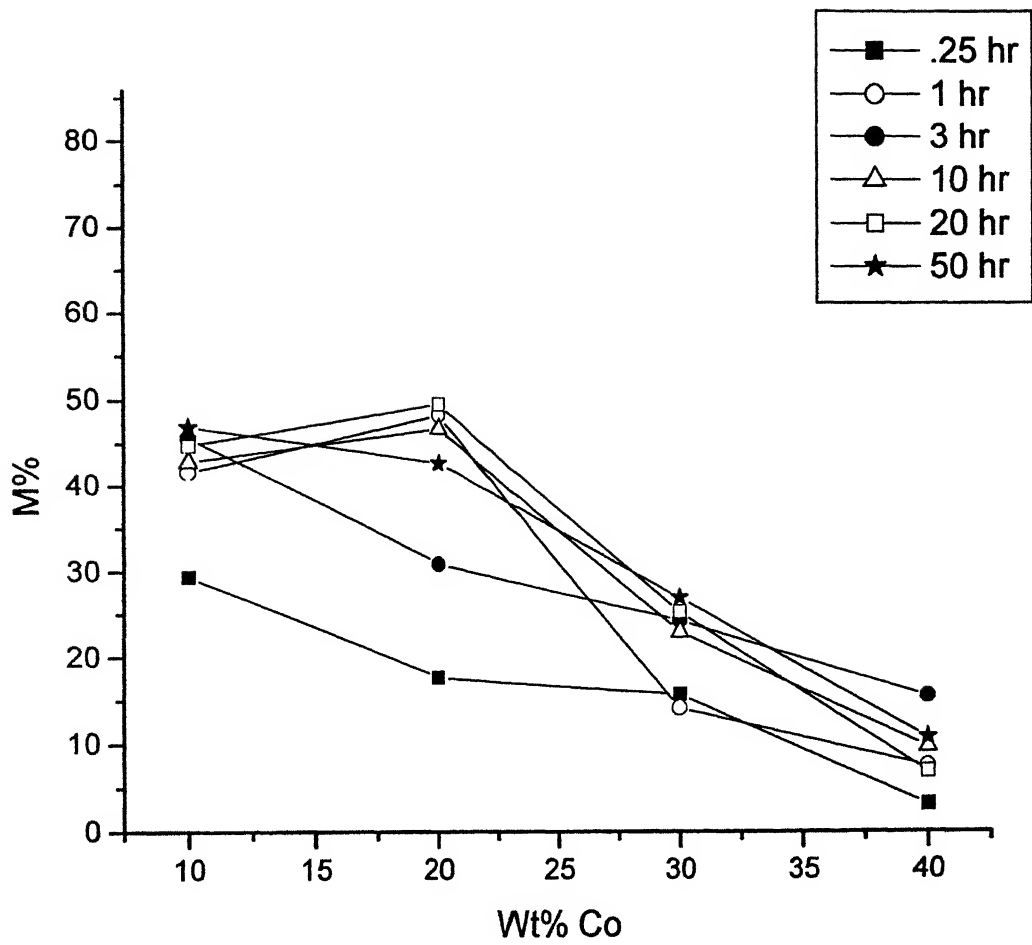


**Figure 4.51:** Variation of volume fraction of cube component as a function of Co content and subjected to different annealing times.

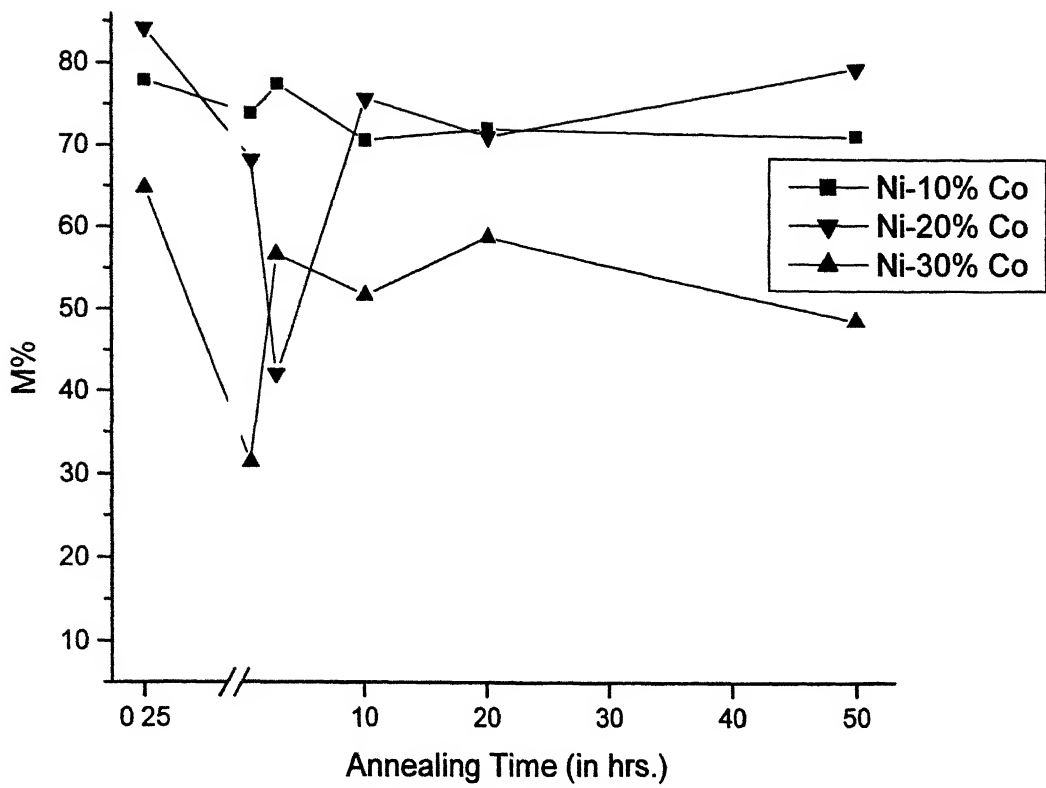


**Figure 4.52:** Variation of volume fraction of cube and its twin component as a function of annealing time for different samples.

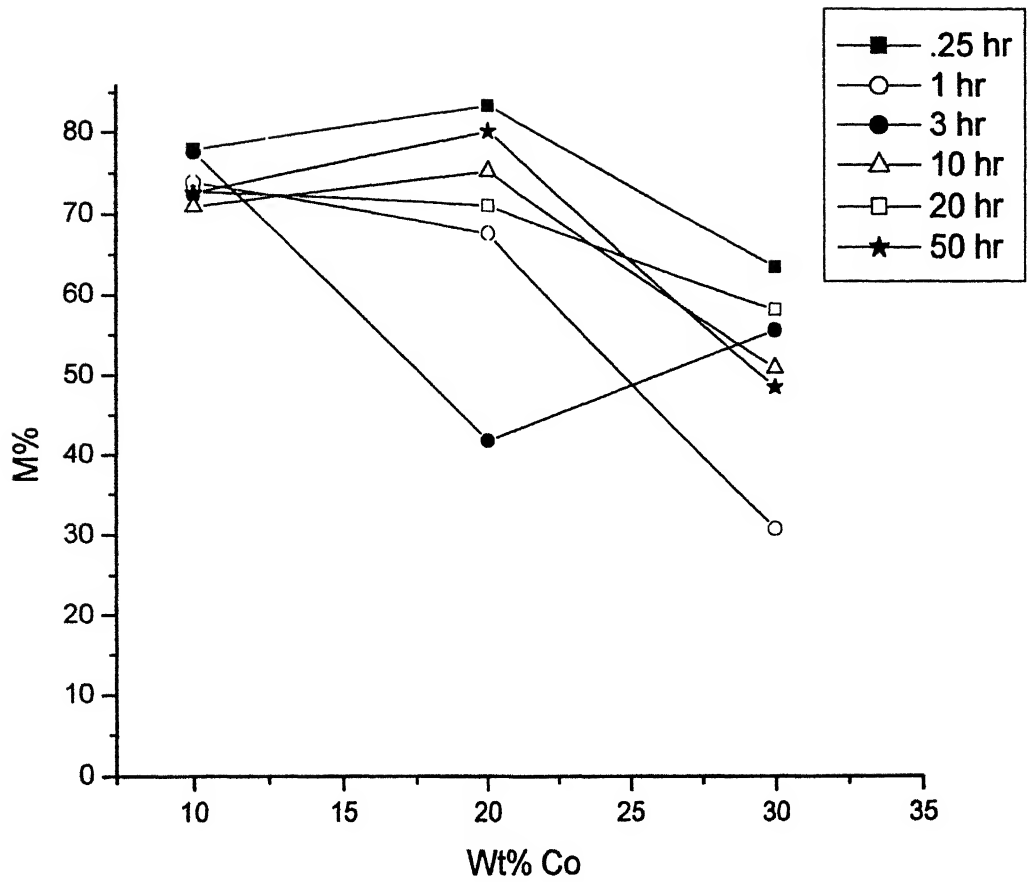


**Figure 4.53:** Variation of volume fraction of cube and its twin component as a function of Co content and subjected to different annealing times.

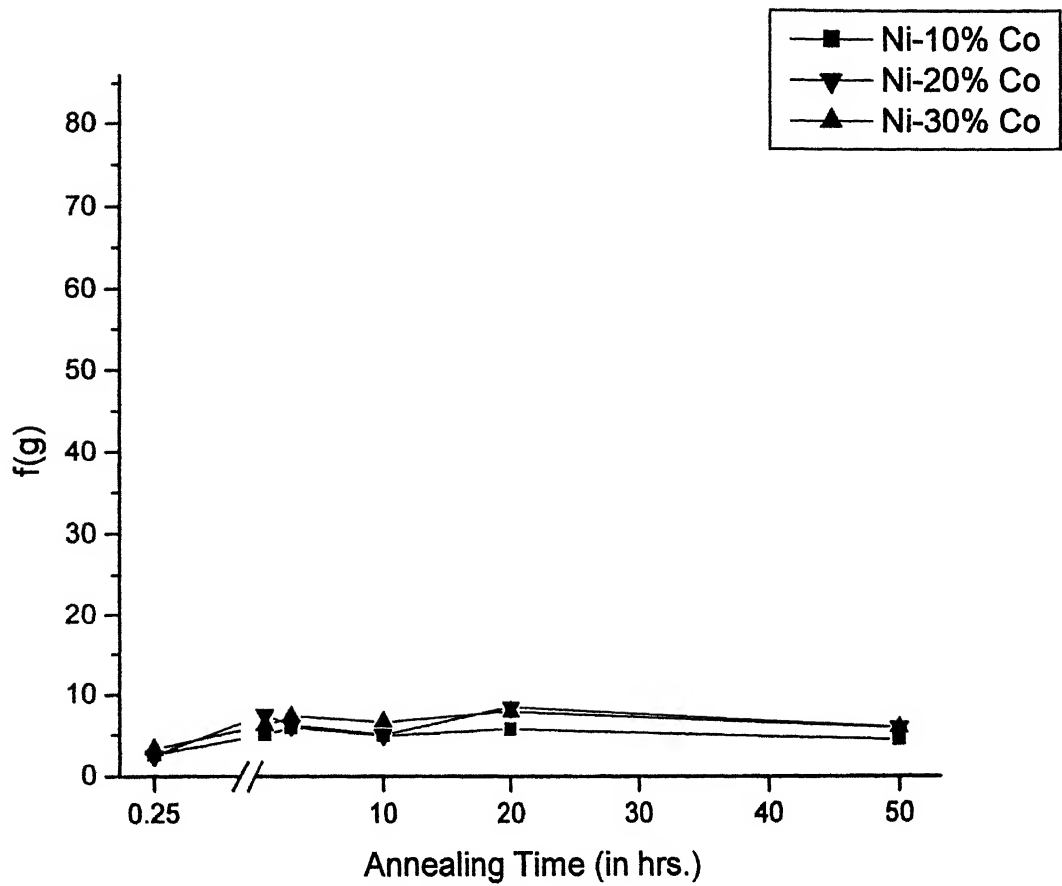


**Figure 4.54:** Variation of intensity of BsT component  $\{437\}<4\ 11\ 7>$  as a function of annealing time for different samples.

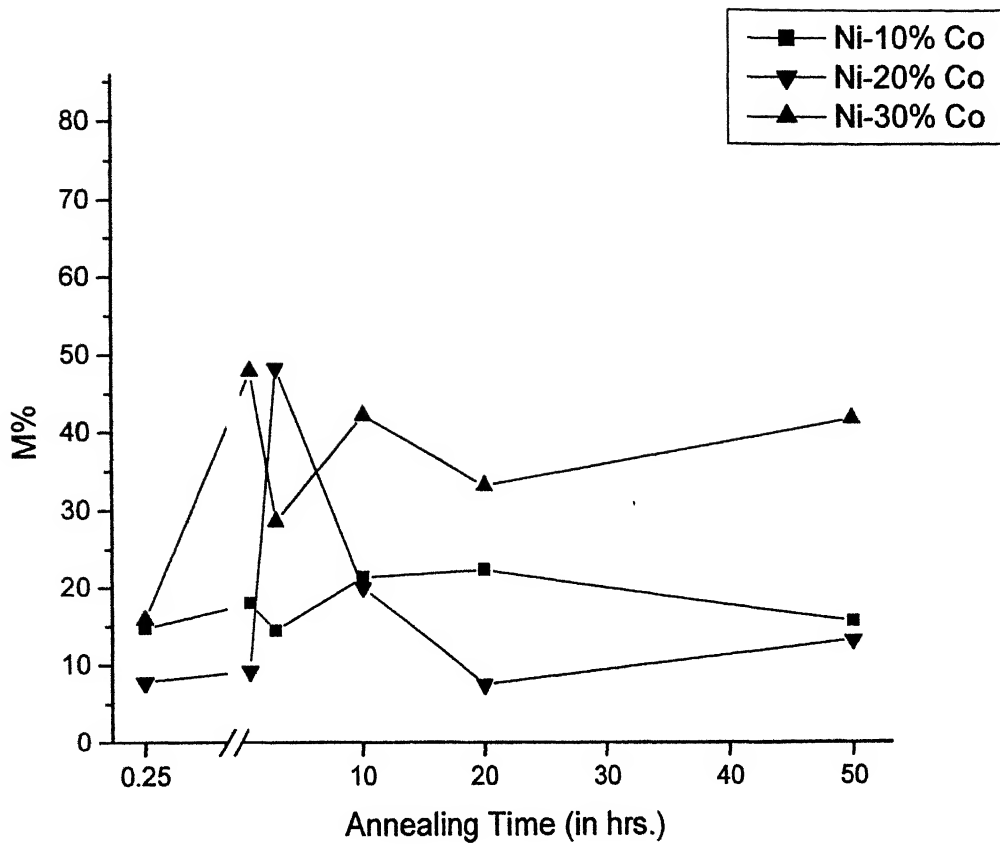


**Figure 4.55:** Variation of volume fraction of BsT component  $\{437\}\langle 4\ 11\ 7\rangle$  as a function of annealing time for different samples.

intensity and volume fraction of rest of the components as a function of annealing time is plotted in **Figures 4.56 and 4.57** respectively. The intensities are constant and nearly same for all the components. In case of volume fraction the  $\{279\}\langle 7\ 11\ 7\rangle$  component is nearly about 50% after 10 hours of annealing time. The plot of rest of the two components is mirror image of each other. It suggests that they grow at the expense of each other. Also considering both the plots it can be said that all three components are highly spread out.

#### **4.3.5: VARIATION OF MAJOR TEXTURE COMPONENTS WITH ANNEALING TIME IN Ni-60% Co ALLOY**

There are two major texture components of Ni-60% Co alloy. They are rotated Goss component  $\{011\}\langle 110\rangle$  and a component near to it  $\{011\}\langle 114\rangle$ . The intensity and volume fraction of this two components as a function of annealing time is plotted in **Figures 4.58 and 4.59** respectively. The intensities of these two components are very nearly the same for all annealing times. The variations of the volume fractions are also similar for the two components and together they constitute almost 80% of the total volume. Again the low intensities of these components indicate that they are highly spread out.

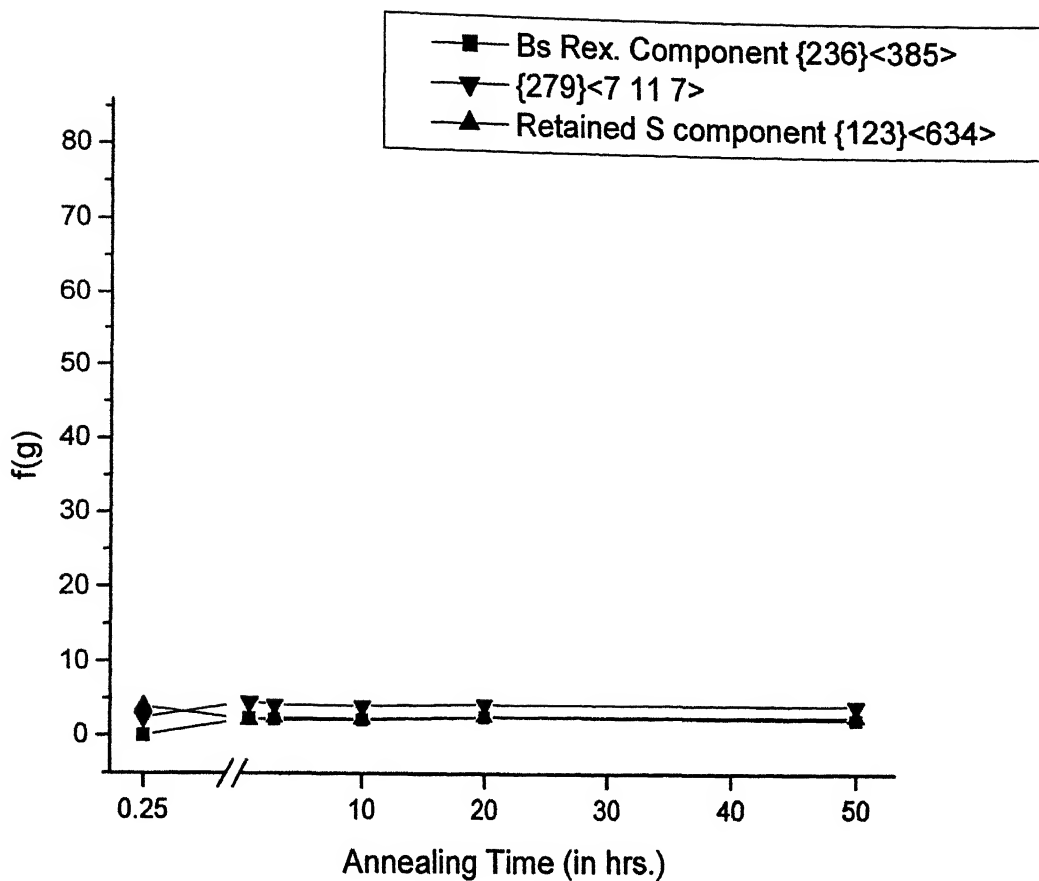


**Figure 4.56:** Variation of intensities of different texture components in Ni-40% Co alloy as a function of annealing time.



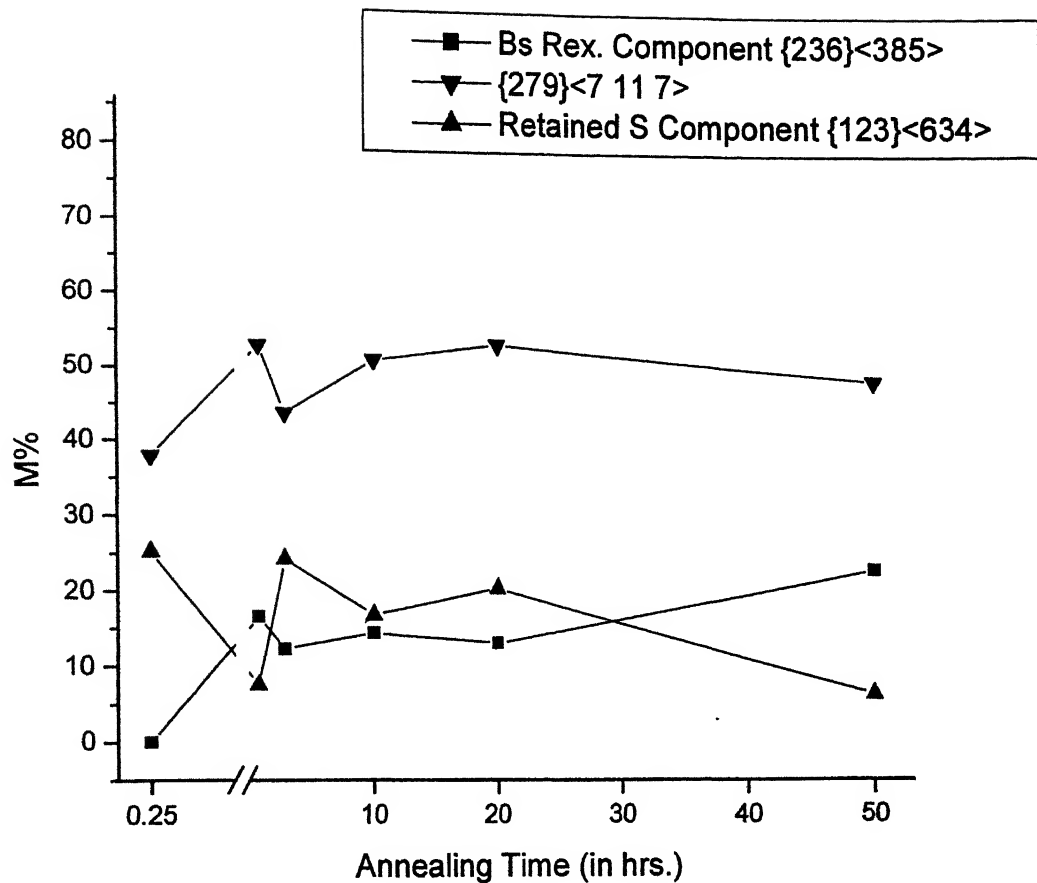


**Figure 4.57:** Variation of volume fractions of different texture components in Ni-40% Co alloy as a function of annealing time.

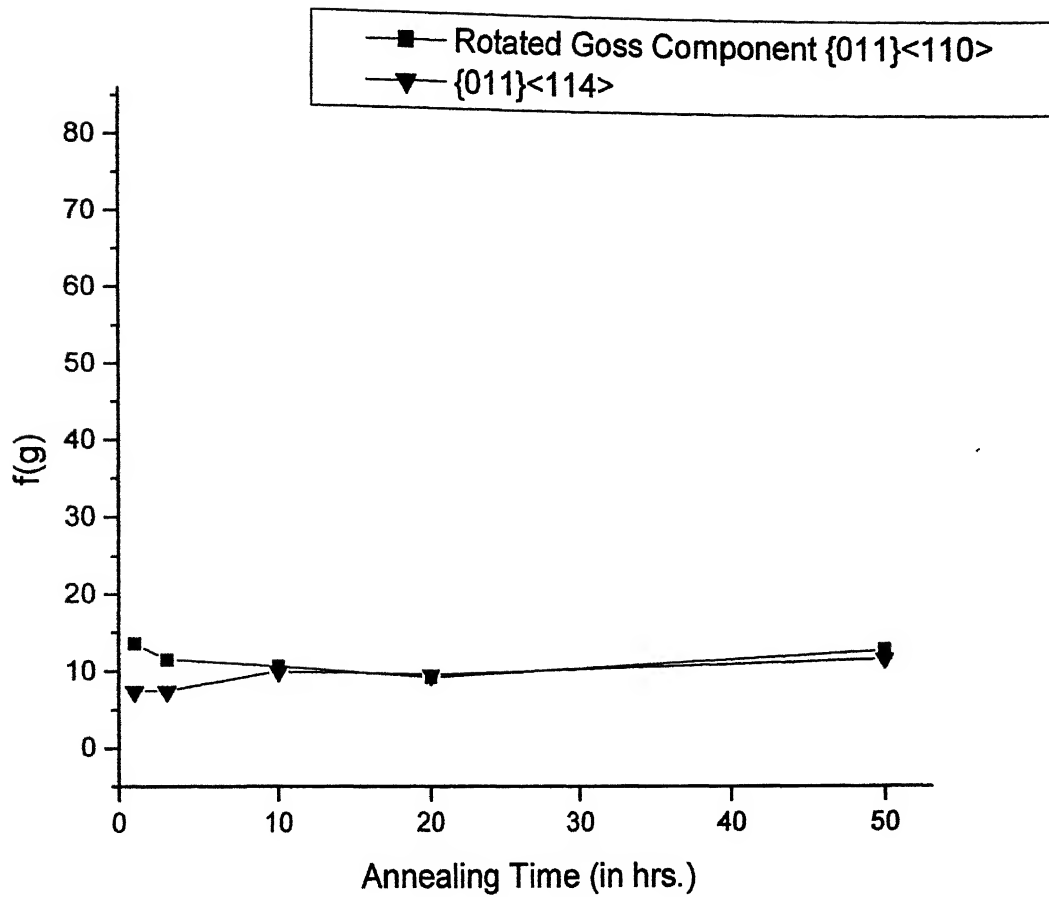


**Figure 4.58:** Variation of intensities of different texture components in Ni-60% Co alloy as a function of annealing time.

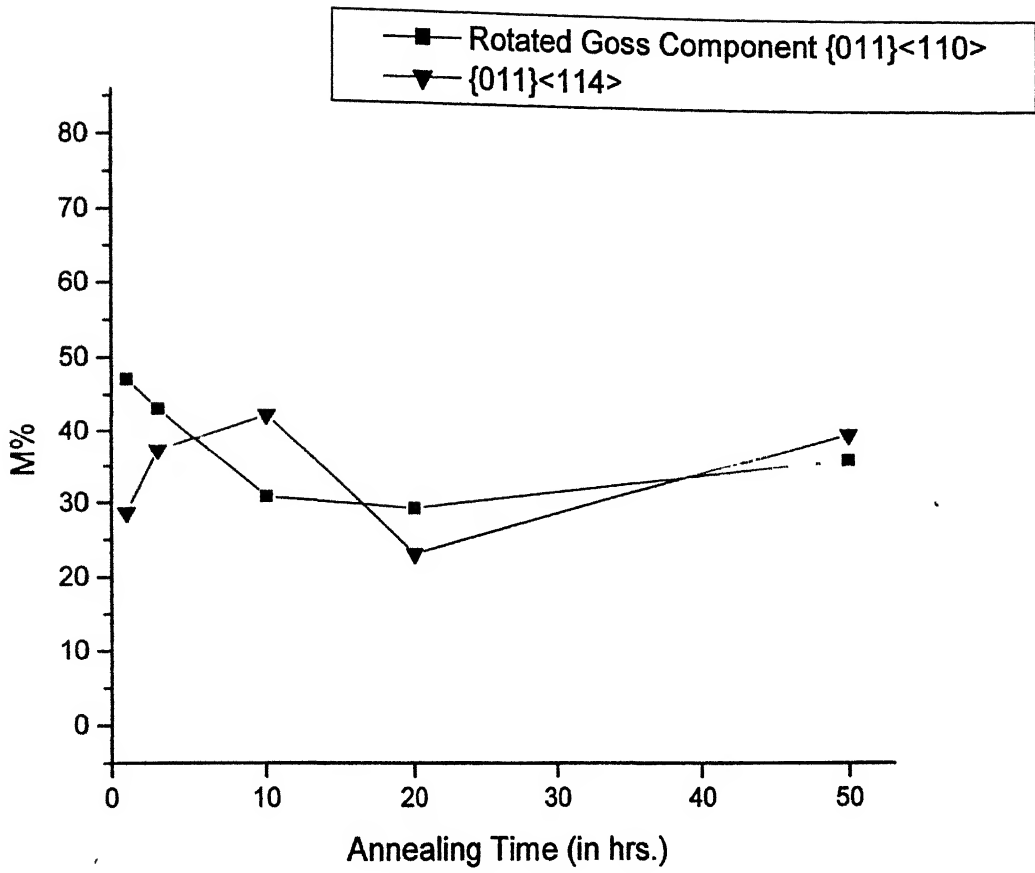


**Figure 4.59:** Variation of volume fractions of different texture components in Ni-60% Co alloy as a function of annealing time.

## DISCUSSION

Pure Ni has moderately high stacking fault energy. With upto 68% of Co, the Ni-Co alloys form continuous series of solid solution. This is evident from our study that throughout the annealing process the microstructures of all the samples consist of a single phase only. All the samples showed recrystallisation even after the shortest period of annealing time. Immediately after recrystallisation, grain growth started on further annealing.

The frequency distributions of the relative energy ratios reveal that the  $\gamma_1/\gamma_3$  ratios of higher frequencies lie within values of 0.6 to 0.8. In the class of 0.9 to 1,  $\gamma_1/\gamma_3$  ratio drastically decreases, becoming zero at  $\gamma_1/\gamma_3 = 1$ . The ratio of  $\gamma_1/\gamma_3$  can only be 1 when the dihedral angles become equal. At equilibrium the dihedral angles of polycrystalline materials come closer to  $120^\circ$  and the corresponding grain boundary energies also approach values close to one another. There is a wide range of frequencies of  $\gamma_1/\gamma_3$  for different annealing time. This indicates that grain growth after recrystallisation is clearly a dynamic process with some grain boundaries becoming more active than others at a particular time and then some other boundaries may take over at a later stage. The profiles of the  $\gamma_1/\gamma_3$  plots, after the longest annealing time, namely 50 hours, do not show maxima at  $\gamma_1/\gamma_3 = 1.0$  for all the five Ni-Co alloys. This indicates that equilibrium is not yet achieved, otherwise this ratio should have gone to 1.0.

It is observed from **Figures 4.29 and 4.33** that the frequencies of the  $\gamma_2/\gamma_3$  ratios vary within a rather narrow range, eventually assuming maxima at  $\gamma_2/\gamma_3 = 1.0$ . But in no case the frequency of  $\gamma_2/\gamma_3$  is greater than 0.6 when  $\gamma_2/\gamma_3 = 1$ . This result, coupled with the fact that  $\gamma_1/\gamma_3$  value never reached 1.0 for any of the alloys, it can safely be inferred that we are still far from reaching the equilibrium when at triple points the grain boundaries will be  $120^\circ$  apart from one another.

The texture results have been given in a tabular form in **Tables 4.1 to 4.30**. It is clear from these tables that there are a number of components present in the textures of all the annealed samples of the five alloys. The cube component and its twin orientations occupy the predominant volume fractions in Ni-10% Co to Ni-30% Co alloy. In Ni-40% Co alloy the important components are the cube component, the BsR component  $\{236\}\langle 385 \rangle$ , the  $\{279\}\langle 7\ 11\ 7 \rangle$  component, and the retained S component

$\{123\}<634>$ . In Ni-60% Co alloy the important components are the rotated Goss component  $\{011\}<110>$  and the component  $\{011\}<114>$  which is near to the rotated Goss component.

After considering all the relative grain boundary energy parameters and texture parameters it was found that the best correlation can be found out if we compare the variation of the frequencies of  $\gamma_1/\gamma_3$  ratio as well as the variation of volume fraction of texture components with annealing time for different alloys.

In case of Ni-10% Co alloy it is seen that upto an annealing time of 20 hours there is no regular pattern in the variation of frequencies of  $\gamma_1/\gamma_3$  ratio with annealing time. This indicates a dynamic situation where some specific grain boundaries become active at one instant, which could change after further annealing, leading to some other specific boundaries becoming more active than the previous one. This kind of behavior has been obtained for all the Ni-Co alloys. Beyond 20 hours of annealing time the frequencies of different classes of  $\gamma_1/\gamma_3$  ratio do not show any large variation. Also the same thing is true if we consider the variation of volume fraction of the cube component and the variation of volume fraction of cube and its twin component as a function of annealing time.

For Ni-20% Co alloy even after 50 hours of annealing equilibrium is not reached both in terms of variation of frequencies of  $\gamma_1/\gamma_3$  ratio with time and variation of volume fraction of cube and its twin component with time and variation of volume fraction of BsT component with time.

In case of Ni-30% Co the frequency of the 0.6 to 0.7 class of  $\gamma_1/\gamma_3$  ratio increases drastically after 20 hours of annealing time. This can be correlated with the increase of volume fraction of the BsT component with time after 20 hours of annealing.

In case of Ni-40% Co alloy after 20 hours of annealing time the class of 0.7 to 0.8 of  $\gamma_1/\gamma_3$  ratio decreases rapidly. From the texture plot of that alloy it can be seen that the volume fraction of the retained S component also decreases after 20 hours of annealing time. On the other hand there is an increase in the frequency of the classes of 0.5 to 0.6 and 0.6 to 0.7 of  $\gamma_1/\gamma_3$  ratio after 20 hours of annealing. Similarly there is an increase in the volume fraction of the BsR component with time after 20 hours of annealing.

In case of Ni-60% Co alloy after 20 hours of annealing time the 0.7 to 0.8 and 0.8 to 0.9 classes of  $\gamma_1/\gamma_3$  ratio increase after 20 hours of annealing time. If we consider the

texture results the rotated Goss component and the  $\{011\}\langle 114 \rangle$  component also increase in volume fraction after 20 hours of annealing time. There is a rapid decrease of the class of 0.6 to 0.7 of  $\gamma_1/\gamma_3$  ratio after 20 hours of annealing. It can be correlated with the decrease in the volume fraction of the component  $\{16\ 4\ 13\}\langle 194 \rangle$  (near to Bs rex. first generation twin) after 20 hours of annealing.

The microstructural and textural study of Ni-Co alloys indicates that these materials are somewhat not stable, texture-wise and grain boundary energy wise even after 50 hours of annealing at 800°C. It would be worthwhile to try to correlate texture and microstructure in these alloys by annealing them at 800°C for much longer periods of time or at temperatures higher than 800°C.

1. The recrystallisation textures of Ni-10% Co to Ni-30% Co alloys are very similar. These are comprised of mainly the cube, its twin components, and BsT component.
2. In Ni-40% Co alloy the important recrystallisation texture components are the BsR component, the  $\{279\}\langle 7\ 11\ 7\rangle$  component, the retained S component, and the cube component.
3. The recrystallisation texture of Ni-60% Co alloy consists mainly of rotated Goss component and the component  $\{011\}\langle 114\rangle$ .
4. There is a wide range of frequencies of  $\gamma_1/\gamma_3$  for different annealing times. This indicates that grain growth after recrystallisation is a dynamic process.
5. The peaks of frequency distribution of  $\gamma_1/\gamma_3$  ratio are spread out in the region of  $\gamma_1/\gamma_3=0.6$  to  $\gamma_1/\gamma_3=0.8$  for different annealing times.  $\gamma_1/\gamma_3$  ratio never reached 1.0 for any of the alloys.
6. In no case the frequency of  $\gamma_2/\gamma_3$  is greater than 0.6 when  $\gamma_2/\gamma_3=1$ .
7. From 5 and 6 it can be concluded that equilibrium has not been reached within the annealing period used.
8. Beyond 20 hours of annealing time the frequencies of different classes of  $\gamma_1/\gamma_3$  ratio do not show any large variation for Ni-10% Co alloy. This is not true for rest of the alloys.
9. The frequency distribution of the grain boundary energy ratios correspond well with the volume fraction of the texture components in all the five alloys after 20 hours of annealing treatment.

## REFERENCES

---

1. G. E. Dieter, *Mechanical Metallurgy*, McGraw-Hill Book Company, London, UK, 1988.
2. K.K. Singh and S. Sangal, *Proceedings of the International Conference on Superplasticity in Advanced Materials*, pp. 149, 1997.
3. <http://www.webelements.com>
4. W. Betteridge, *Nickel and its Alloys*, Macdonald and Evans Ltd., London, UK, 1977.
5. P. Cotterill and P. R. Mould, "Recrystallisation and Grain Growth in Metals," Surrey University Press, London, UK, 1976.
6. R. K. Ray, Ph. D. Thesis, University of Birmingham, 1973.
7. V. Yu, Novikov, Poverkh. Fiz, *Khim. Mekh.*, vol. 5, pp. 47, 1982.
8. H. J. Bunge, H. P. Lee and E. Dehlen, *Growth Selection and Texture Changes during Continuous Grain Growth*.
9. H. J. Bunge, *Mathematische Methoden der Texturanalyse*, Academic Press, Berlin, Germany, 1969.
10. R. K. Ray, *Acta Met*, vol. 43, n. 10, pp. 3861, 1995.
11. P. H. Pumphery and H. Gleiter, *Phil. Mag.*, vol. 30A, pp. 593, 1974.
12. N. A. Gjostein and F. N. Rhines, *Acta Met.*, vol. 7, pp. 319, 1959.
13. S. Sangal, *Metals Materials and Processes*, vol. 10, n. 4, pp. 313, 1998.
14. K. K. Singh, Ph. D. Thesis, IIT Kanpur, 1998.
15. L. G. Schluz, *J. Appl. Phys.*, vol. 20, pp. 1030, 1949.
16. J. Hansen, J. Pospiech, and K. Lucke, *Tables for Texture Analysis of Cubic Crystals*, Springer-Verlag, Berlin, Germany, 1978.
17. A. K. Jain, "Fundamentals of Digital Image Processing", Printice Hall, New Jersey, USA, 2000.
18. S. Chhabra, P. Chhillar, S. Sangal, *Practical Metallography*, submitted in January 2002.



# Appendix A

## Computer Programs

### A1. Program to read image data and convert into coordinate System

```
/* mod_exgb.c*/
#include <stdio.h>
#include <conio.h>

#define MAXPIXEL 15000 /* size for the max points analysed*/
#define MAXSEG 1000 /* maximum pixels in a gb segment */
#define GBPIXEL '0' /* value of gb pixel */

int getap(int value[][2], int nc, int n, int p[], int m);
int test_tp(int value[][2], int p[]);

main()
{
    int p[3],q[3],gb[MAXSEG],value[MAXPIXEL][2];
    int i,j,k,l,nc,count;
    char c;

    for(i=0,j=0,nc=0;(((c=getc(stdin))!=EOF) && (nc<MAXPIXEL));)
    {
        /* reading pixel coordinates */
        if(c=='\n') {
            /* end of line */
            fprintf("(%i,%i)\n",i,j);
            i=i++;
            j=0;
        }
        if(c == GBPIXEL) {
            value[nc][0] = j; /* array stores x,y position */
            value[nc][1] = i; /* of gb pixel */
            nc++;
        }
        if((c == '0') || (c == '1')) j++;
    }
    if(nc>=MAXPIXEL) fprintf("Warning: Could not read all of image data!\n");

    count = 0; /* set triple point counter */
    for (i=0;i<nc;i++)
    {
        k = getap(value,nc,i,p,3);
        if (k == 3) { /* k=3 : it is a triple point */
            if(test_tp(value,p)==1) continue;
            if(count > 0) printf("-1\n"); /* end of line marker */
        }
    }
}
```

```

for (j=0;j<3;j++)
{
    l=2;
    gb[0] = i;
    gb[1] = p[j];
    do {
        if ((k = getap(value,nc,gb[l-1],q,3)) == 2) {
            if (gb[l-2] == q[0]) /* exclude the duplicate pixel */
                gb[l] = q[1];
            else
                gb[l] = q[0];
            l++;
        }
    } while ((k == 2) && (l < MAXSEG));
    for(k=0;k<l;k++) printf("%i %i ",value[gb[k]][0],value[gb[k]][1]);
    if (j < 2) printf("-1\n"); /* end of line marker */
}
count++;
}
}
printf(" %d\n",count);
printf("-99\n"); /* end of file marker */
}

```

```

int getap(int value[][2], int nc, int n, int p[], int m)
{
    /* returns no. of adjacent pixels touching pixels n */
    /* on return, p[] contains the first m adjacent points */

```

```

    int i,j,k,x,y,dx,dy;

```

```

    x = value[n][0];

```

```

    y = value[n][1];

```

```

    i = n;

```

```

    j = -1;

```

```

    k = 0;

```

```

    do {

```

```

        i = i + j;

```

```

        if (i >= nc) break; /* no more gb pixels to check */

```

```

        if (i < 0) {

```

```

            i = n;

```

```

            j = 1;

```

```

        }

```

```

    } else {

```

```

        dy = value[i][1] - y;

```

```

        if ((dy < -1) || (dy > 1)) {

```

```

            if (j == -1) {

```

```

                i = n;

```

```

                j = 1;

```

```

            }

```

```

        } else

```

```

            /* no need to check further */

```

```

    }
    else {
        dx = value[i][0] - x;
        if ((dx > -2) && (dx < 2)) {
            if (k < m) p[k] = i; /* found a pixel "i" touching pixel "n" */
            k++;
        }
    }
}
} while(1);
return(k);
}

```

```

int test_tp(int value[][2], int p[])
{
    int x[3],y[3];
    int i,j;

    for(i=0;i<3;i++)
    {
        x[i]=value[p[i]][0];
        y[i]=value[p[i]][1];
    }

    for(i=0;i<3;i++)
    {
        j=i+1;
        if(j==3) j=0;

        if(x[i]==x[j])
        { if(y[i]==(y[j]+1)||y[i]==(y[j]-1))
            return(1);
        }

        if(y[i]==y[j])
        { if(x[i]==(x[j]+1)||x[i]==(x[j]-1))
            return(1);
        }
    }

    return(0);
}

```

## A.2 Program for Evaluating Plane Dihedral Angles

```
/* modtpa3.c*/
#include <errno.h>
#include <stdio.h>
#include <alloc.h>
#include <math.h>
#include <conio.h>

#include "modcfit3.c"      /* this file is given in Appendix A.3 */

#define MAX_DATA 100
#define MAX_TP 400

#define DISTANCE(x1,y1,x2,y2) ((x1-x2)*(x1-x2)+(y1-y2)*(y1-y2))

typedef struct {
    int order,npts;
    float x,y,r2,*a;
} polycoeff;

typedef struct {
    float tx,ty,beta[3];
    polycoeff g[3];
} triplepoint;

int tpfit(triplepoint t[], int *ntp);
int gb_line(float x[], float y[], int *ndat);
void pda(triplepoint t[], int ntp);
get_distance(double d[], double s1, double s2, triplepoint t, int i);
double slope(float a[], int order, int x);

main()
{
    int ntp;

    triplepoint t[MAX_TP];
    cprintf("\nProgram Begin\n");
    tpfit(t,&ntp);
    pda(t,ntp);
    cprintf("ntp = %i\n",ntp);
}

void pda(triplepoint t[],int ntp)
{
    int k,i,j,p,q,r;
    double s[3],d[3];
    FILE *fp;
```

```

if ((fp = fopen("coeff.log","w")) == NULL) cprintf("unable to create coeff.log\n");
fprintf(fp, "#,tpx,tpy,order,a0,a1,a2,a3,a4,a5,a6\n");

printf("#,tpx,tpy,ord1,r2_1,ord2,r2_2,ord3,r2_3,beta1,beta2,beta3,sumbeta\n");

for(k=0;k<ntp;k++)
{
    if(t[k].g[0].npts<=4||t[k].g[1].npts<=4||t[k].g[2].npts<=4)
    {
        /* printf("\n%f%f has too few points to continue\n",t[k].tx,t[k].ty);*/
        continue;
    }

    if(t[k].tx== -1)
        continue;
    printf("%i,%f,%f,",k+1,t[k].tx,t[k].ty);

    for(i=0;i<3;i++)
    {
        s[i]=slope(t[k].g[i].a,t[k].g[i].order,t[k].tx);
        /* printf(" slope %d is %lf ",i,s[i]);*/
    }
    /* printf("\n");*/

    for(i=0;i<3;i++)
    {
        j=i+1;
        if(j==3) j=0;
        get_distance(d,s[i],s[j],t[k].i);
        t[k].beta[i]=acos((d[0]+d[1]-d[2])/(2*sqrt(d[0])*sqrt(d[1])))*(180/3.1412);
    }
    check = ' ';
    if((t[k].beta[0]+t[k].beta[1]+t[k].beta[2])<360) {
        check = '*';
        for(p=0;p<3;p++){
            q=p+1;
            if(q==3) q=0;
            r=q+1;
            if(r==3) r=0;
            if(((t[k].beta[p]+t[k].beta[q])>=(t[k].beta[r]-0.001))
            &&((t[k].beta[p]+t[k].beta[q])<=(t[k].beta[r]+0.001)))
            {
                t[k].beta[p]=180-t[k].beta[p];
                t[k].beta[q]=180-t[k].beta[q];
            }
        }
    }
}

```

```

for(p=0;p<3;p++) printf("%i,%f",t[k].g[p].order,t[k].g[p].r2);
for(p=0;p<3;p++) printf("%f",t[k].beta[p]);
printf("%f",t[k].beta[0]+t[k].beta[1]+t[k].beta[2]);
if (check == ' ')
    printf("\n");
else
    printf(",%c\n",check);

for(p=0;p<3;p++)
{
    fprintf(fp,"%i,%f,%f,%i",k+1,t[k].tx,t[k].ty,t[k].g[p].order);
    for(i=0;i<=t[k].g[p].order;i++) fprintf(fp,"%f",t[k].g[p].a[i]);
    fprintf(fp,"\n");
}
}
fclose(fp);
}

```

```

get_distance(double d[], double s1, double s2, triplepoint t, int i)
{
    double c1,c2,y1,y2,x1,x2,m1,m2,k1,k2;
    int j;

```

```

j=i+1;
if(j==3) j=0;
c1=t.ty-s1*t.tx;
c2=t.ty-s2*t.tx;
x1=t.g[i].x;
x2=t.g[j].x;
y1=t.g[i].y;
y2=t.g[j].y;

```

```

if (s1 == 0) {
    x1 = t.g[i].x;
    y1 = t.ty;
}
else {
    m1=-(1/s1);
    k1=(y1-(m1*x1));
    x1=((k1-c1)/(s1-m1));
    y1=((m1*c1)-(s1*k1))/(m1-s1);
}

```

```

if (s2 == 0) {
    x2 = t.g[j].x;
    y2 = t.ty;
}

```

```

else {
    m2=-(1/s2);
    k2=(y2-(m2*x2));

```

```

    y2=((((m2*c2)-(s2*k2))/(m2-s2));
}

d[0]=DISTANCE(t.tx,t.ty,x1,y1);
d[1]=DISTANCE(t.tx,t.ty,x2,y2);
d[2]=DISTANCE(x1,y1,x2,y2);
}

```

```

double slope(float a[], int order, int x)
{
    int i;
    double sum = 0;

    for(i=1;i<=order;i++)
        sum=sum+i*((double) a[i])*pow(x,i-1);

    return(sum);
}

```

```

int tpfit(triplepoint t[], int *ntp)
{
    float x[MAX_DATA],y[MAX_DATA],sig[MAX_DATA],a[MAX_SIZE];
    int ndat,i,ord,j,l,err,fe,upperord;
    float r2;
/*    FILE *fp;*/

/*    DATA INPUT & CALCULATIONS */
    for (i=0;i<MAX_DATA;i++) sig[i] = 1;

/*    fp = (FILE *) fopen(fname,"r");
    if (fp == NULL) {
        printf("file error: %i\n",errno);
        exit(0);
    }
*/

    (*ntp) = 0;
    do
    {
        for(i=0;i<3;i++)
        {
            fe = gb_line(x,y,&ndat);
            err = polyfit(x,y,sig,ndat,1,6,&ord,a,&r2,1,x[0],y[0]);
            if (!err)
            {
                t[*ntp].tx = x[0];
                t[*ntp].ty = y[0];
                t[*ntp].g[i].order = ord;

```

```

        t[*ntp].g[i].y=y[ndat-1];
        t[*ntp].g[i].r2 = r2;
        t[*ntp].g[i].npts=ndat;
        if (((t[*ntp].g[i].a = (float *)
            malloc((ord+1)*sizeof(float))) == NULL)
        {
            fprintf("warning: out of memory in tpfit\n");
            getch();
            return(-1);    /* out of memory */
        }
        for(j=0;j<=ord;j++) t[*ntp].g[i].a[j] = a[j];
    }
    else {
        t[*ntp].tx = -1;
        for (l=i+1;l<3;l++)
            fe = gb_line(x,y,&ndat);
        break;
    }
}
(*ntp)++;
} while(fe != -99);
return(0);
}

```

```

int gb_line(float x[], float y[],int *ndat)
{
    int num;

    (*ndat) = 0;
    do
    {
        scanf("%i",&num);
        if(num >= 0) {
            if (*ndat < MAX_DATA)
                x[*ndat] = (float) num;
            scanf("%i",&num);
            if (*ndat < MAX_DATA) {
                y[*ndat] = (float) num;
                (*ndat)++;
            }
        }
    } while(num >= 0);
    return(num);
}

```



### A.3 Program for Curve Fitting

```
/* modcfits.c */
#include <stdio.h>
#include <stdlib.h>
#include <math.h>

#include "cfits.h"      /* This header file is given in Appendix A.4 */

/*
main()
{

float x[100], y[100], sig[100], a[MAX_SIZE], xi;
int i, ord;

for (i=0;i<50;i++)
{
xi = ((float) i)/50.0;
x[i] = xi;
y[i] = 0.01+0.02*xi+0.04*xi*xi + ((float) random(100))/100;
sig[i] = 1;
}
polyfit(x,y,sig,50,1,7,&ord,a,0,0,0);
}
*/

int polyfit(float x[],float y[],float sig[],int ndat,int ord1,int ord2,int *ord,float a[],float
*r2,int ianch,float anch_x,float anch_y)
{
/* Polynomial Least Square Fit:
x, y: "ndat" data points; sig: "ndat" standard deviations;
ord1,ord2: search poly order ord1 to ord2 and return best value in *ord (to
implement)
a: on return contains "**ord+1" polynomial coefficients
ianch: non-zero value => set anchor at "anch_x,anch_y"
return value: non-zero => no solution possible */

int temp,i,j,deg1,deg2,err, ia[MAX_SIZE];
float chisq,chisq1,a1[MAX_SIZE],f1est;
double yc,ym;
long double covar[MAX_SIZE][MAX_SIZE], a_x, st, sr;

void (*fn)(float, long double [], int);      /* function pointer */

if (ord2<ord1) SWAP(ord1,ord2)
if ((ord1<0)||((ord2>MAX_ORDER))) return(-1); /* invalid polynomial order */
if (ndat<=ord1) return(-1); /* invalid no. of data points */
if (ndat<=ord2) ord2=ndat-1; /* reduce the upper polynomial order */
```

```

fn = polyfunc1;
if (ianch) {          /* set anchor point */
    anchor_x = anch_x;
    anchor_y = anch_y;
    fn = polyfunc2;
}

for(*ord=ord1;*ord<=ord2;*ord++)
{
    for(i=0;i<=*ord;i++) ia[i] = 1;
    if (ianch) {      /* set anchor for each order value */
        ia[0] = 0;
        a[0] = anchor_y;
    }
    err = gllsq(x,y,sig,ndat,a,ia,(*ord)+1,covar,&chisq,fn);
    if (err != 0) return(err);    /* Error: solution not possible */
    if (ianch) {
        a_x = 1;
        for (i=1;i<=*ord;i++)
        {
            a_x = a_x*((long double) anchor_x);
            a[0] -= a[i]*a_x;
        }
    }
    if((*ord)>ord1)
    {
        deg1=ndat-(*ord);
        deg2=ndat-((*ord)+1);
        if (chisq1 < chisq) break;
        if((deg2!=0)&&(chisq1!=chisq))
            ftest=(((deg1-deg2)*chisq)/((chisq1-chisq)*deg2));
        else
            break;
        if(ftest > 1)
            break;
    }
    for(i=0;i<=(*ord);i++)
        a1[i]=a[i];
    chisq1=chisq;
}
(*ord)=(*ord)-1;
for(i=0;i<=(*ord);i++) a[i] = a1[i];
ym = 0;          /* calculation of correlation coefficient */
for(i=0;i<ndat;i++) ym += y[i];
ym = ym/ndat;
sr = st = 0;
for(i=0;i<ndat;i++)
{
    st += (long double) ((y[i] - ym)*(y[i] - ym));
}

```

```

    for(j=0;j<=*ord;j++) yc += a[j]*pow((double) x[i],(double) j);
    sr += (long double) ((y[i] - yc)*(y[i] - yc));
}
if ((st == 0.0) || (sr == 0))
    (*r2) = 1;
else
    (*r2) = (float) ((st - sr)/st);
return(0);
}

```

```

void polyfunc1(float x, long double afunc[], int ma)
{

```

```

/* returns basis functions (at x) in "afunc" in a polynomial of order "ma-1" */

```

```

    int i;
    afunc[0] = 1;
    for (i=1;i<ma;i++)
    {
        afunc[i] = ((long double) x) * afunc[i-1];
    }
}

```

```

void polyfunc2(float x, long double afunc[], int ma)
{

```

```

/* returns basis functions (at x) in "afunc" in a polynomial of order "ma-1"
   under constraint that curve is anchored at: (anchor_x, anchor_y) */

```

```

    int i;
    long double x1 = 1, x2 = 1;

    afunc[0] = 1;
    for (i=1;i<ma;i++)
    {
        x1 = x1*x;
        x2 = x2*((long double) anchor_x);
        afunc[i] = x1 - x2;
    }
}

```

```

int gllsq(float x[], float y[], float sig[], int ndat, float a[], int ia[], int ma, long double
covar[][MAX_SIZE], float *chisq, void (*gfunc)(float, long double [], int))
{

```

```

/* General Linear Least Square Routine:

```

```

x, y: "ndat" data points; sig: "ndat" standard deviations; ma: # of parameters;
ia: "ma" size with only zero or non-zero values; zero value implies, corresponding
parameter held fixed to value stored in "a"; gfunc: user routine to supply "ma"
basis functions evalated in array afunc (size: "ma");
returns ChiSquare in "chisq" and covariance matrix in covar;
return value: non-zero => no solution possible */

```

```

int err,i,j,k,l,m,mfit=0;
float ym,wt,sum,sig2i;
long double beta[MAX_SIZE],afunc[MAX_SIZE];

for (j=0;j<ma;j++)
    if (ia[j]) mfit++;
if (mfit == 0) return(-1);    /* no parameters to be fitted */

for (j=0;j<mfit;j++)
{
    /* Initialize the (symmetric) matrix */
    for (k=0;k<mfit;k++) covar[j][k]=0.0;
    beta[j]=0.0;
}
for (i=0;i<ndat;i++)
{
    /* Loop over data to accumulate coefficients of the normal equations */
    (*gfunc)(x[i],afunc,ma);
    ym=y[i];
    if (mfit < ma)
    {
        /* Subtract off dependences on known pieces of the fitting function */
        for (j=0;j<ma;j++)
            if (!ia[j]) ym -= a[j]*afunc[j];
    }
    sig2i=1.0/SQR(sig[i]);
    for (j=-1,l=0;l<ma;l++)
    {
        if (ia[l]) {
            wt=afunc[l]*sig2i;
            for (j++,k=-1,m=0;m<=l;m++)
                if (ia[m]) covar[j][++k] += wt*afunc[m];
            beta[j] += ym*wt;
        }
    }
}
for (j=1;j<mfit;j++) /* Fill in above the diagonal from symmetry */
    for (k=0;k<j;k++)
        covar[k][j]=covar[j][k];
if ((err=gaussj(covar, mfit, beta)) != 0)    /* Matrix solution */
    return(err); /* no solution possible */
for (j=-1,l=0;l<ma;l++)
    if (ia[l]) a[l]=beta[++j]; /* Partition solution to appropriate coefficients a */
*chisq=0.0; /* and Evaluate ChiSquare of the fit */
for (i=0;i<ndat;i++)
{
    (*gfunc)(x[i],afunc,ma);
    for (sum=0.0,j=0;j<ma;j++)
        sum += a[j]*afunc[j];
    *chisq += SQR((y[i]-sum)/sig[i]);
}
covsrt(covar,ma,ia,mfit); /* Sort covariance matrix to true order of fitting coefficients

```

```

    return(0);
}

void covsrt(long double covar[][MAX_SIZE], int ma, int ia[], int mfit)
{
/* Expand in storage the covariance matrix covar, so as to take into account
   parameters that are being held fixed (For latter, return zero covariances) */

    int i,j,k;
    long double temp;

    for (i=mfit;i<ma;i++)
        for (j=0;j<=i;j++) covar[i][j]=covar[j][i]=0.0;
    k=mfit;
    for (j=ma-1;j>=0;j--) {
        if (ia[j]) {
            for (i=0;i<ma;i++) SWAP(covar[i][k],covar[i][j])
            for (i=0;i<ma;i++) SWAP(covar[k][i],covar[j][i])
            k--;
        }
    }
}

int gaussj(long double a[][MAX_SIZE], int n, long double b[])
{
/* Gauss-Jordon Method; uses Full Pivoting
   a: square matrix of size "n x n"; b: vector of size n
   on return: "a" contains inverse of "a" and the solution in "b"
   return value: == 0 => no error; != 0 => no solution possible */

    int indxc[MAX_SIZE],indxr[MAX_SIZE],ipiv[MAX_SIZE];
    int i,col,irow,j,k,l,ll;
    long double big,dum,pivinv,temp,temp1;

    for (j=0;j<n;j++) ipiv[j]=0;    /* set pivot tracking elements to zero */

    for (i=0;i<n;i++)    /* main loop for pivot search */
    {
        big=0.0;
        for (j=0;j<n;j++)
        {
            if (ipiv[j] != 1)    /* skip, if diagonal element in jth row is a pivot */
            {
                for (k=0;k<n;k++)
                {
                    if (ipiv[k] == 0)
                    {
                        if (a[j][k] < 0)

```

```

        else
            temp1 = a[j][k];
            if (temp1 >= big)
            {
                big = temp1;
                irow=j;
                icol=k;
            }
        }
        else if (ipiv[k] > 1) return(1); /* Error: Singular Matrix-1 */
    }
}
++(ipiv[icol]);          /* irow, icol should contain the position of pivot */
if (irow != icol)        /* if irow = icol, then pivot already in place */
{                          /* else position pivot by swapping rows */
    for (l=0;l<n;l++) SWAP(a[irow][l],a[icol][l])
    SWAP(b[irow],b[icol])
}
indxr[i]=irow;           /* keep track of the original pivot position */
indxc[i]=icol;

if (a[icol][icol] == 0.0) return(2); /* Error: Singular Matrix-2 */

pivinv=1.0/a[icol][icol]; /* Now divide the pivot row by the pivot element */
a[icol][icol]=1.0;
for (l=0;l<n;l++) a[icol][l] *= pivinv;
b[icol] *= pivinv;

for (ll=0;ll<n;ll++) /* Reduce the rows except the pivot one */
{
    if (ll != icol)
    {
        dum=a[ll][icol];
        a[ll][icol]=0.0;
        for (l=0;l<n;l++) a[ll][l] -= a[icol][l]*dum;
        b[ll] -= b[icol]*dum;
    }
}
} /* End of Main Loop */

for (l=n-1;l>=0;l--) /* Unscramble the solution by interchanging columns */
{
    if (indxr[l] != indxc[l])
        for (k=0;k<n;k++)
            SWAP(a[k][indxr[l]],a[k][indxc[l]]);
}
return(0);
}

```

## A.4 Header File Used by Curve Fitting Program

```
/* cfit.h*/  
#define SWAP(a,b) {temp=(a);(a)=(b);(b)=temp;}  
  
static float sqrarg;  
#define SQR(a) ((sqrarg=(a)) == 0.0 ? 0.0 : sqrarg*sqrarg)  
  
#define MAX_ORDER 9  
#define MAX_SIZE MAX_ORDER+1  
  
static float anchor_x, anchor_y;  
  
int polyfit(float x[],float y[],float sig[],int ndat,int ord1,int ord2,int *ord,float a[],float  
*r2,int ianch,float anch_x,float anch_y);  
void polyfunc1(float x, long double afunc[], int ma);  
void polyfunc2(float x, long double afunc[], int ma);  
void covsrt(long double covar[][MAX_SIZE], int ma, int ia[], int mfit);  
int gllsq(float x[], float y[], float sig[], int ndat, float a[], int ia[], int ma, long double  
covar[][MAX_SIZE], float chisq[], void (*gfunc)(float, long double [], int));  
int gaussj(long double a[][MAX_SIZE],int n, long double b[]);
```

## A.5 Program to Convert PDA to TDA

```
/*pda2tda.c*/
#include<stdio.h>
#include<stdlib.h>
#include "gaussj.c"      /* This program is give in appendix A.6*/

main()
{

    FILE *fp,*fa,*fb;
    long double a[MAX_SIZE][MAX_SIZE];
    long double b[MAX_SIZE];
    char fname1[50],fname2[50];
    int i=0,j=0,nc;
    float x;

    fp=fopen("table.txt","r");      /* Table 2.3 is used here*/

    if(fp==NULL)
        printf("error1");

    do {
        fscanf(fp,"%f",&x);
        if(x < 0)
        {
            i=i+1;
            j=0;
        }
        else {
            a[i][j] = (long double) x;
            j=j+1;
        }
    } while(x > -99);

    nc = i;
    fclose(fp);

    printf("Input File Name: ");
    scanf("%s",fname1);
    printf("Output File Name: ");
    scanf("%s",fname2);
    fa=fopen(fname1,"r");
    fb=fopen(fname2,"w");
    if(fa==NULL)
    {
        printf("error2\n");
        exit(0);
    }
}
```



```
for (i=0;i<nc;i++)  
{  
    fscanf(fa,"%Lf",&b[i]);  
}
```

```
fclose(fp);  
fclose(fa);
```

```
gaussj(a,17,b);
```

```
for(i=0;i<17;i++)  
{  
    printf("%Lf\n",b[i]);  
    fprintf(fb,"%Lf\n",b[i]);  
}
```

```
getch();  
}
```

## A.6 Program Used by PDA to TDA Conversion Program

```
/*gaussj.c*/
#include <stdio.h>
#include <stdlib.h>
#include <math.h>

#include "cfit.h"          /* This header file is given in appendix A.4*/

/*main()
{

float x[100], y[100], sig[100], a[MAX_SIZE], xi;
int i, ord;

for (i=0;i<50;i++)
{
    xi = ((float) i)/50.0;
    x[i] = xi;
    y[i] = 0.01+0.02*xi+0.04*xi*xi + ((float) random(100))/100;
    sig[i] = 1;
}*/

polyfit(x,y,sig,50,1,7,&ord,a,0,0,0);

}
int gaussj(long double a[][MAX_SIZE], int n, long double b[])
{

/* Gauss-Jordon Method; uses Full Pivoting
a: square matrix of size "n x n"; b: vector of size n
on return: "a" contains inverse of "a" and the solution in "b"
return value: == 0 => no error; != 0 => no solution possible */
int indxc[MAX_SIZE],indxr[MAX_SIZE],ipiv[MAX_SIZE];
int i,col,irow,j,k,l,ll;
long double big,dum,pivinv,temp,temp1;

for (j=0;j<n;j++) ipiv[j]=0; /* set pivot tracking elements to zero */

for (i=0;i<n;i++)          /* main loop for pivot search */
{
    big=0.0;
    for (j=0;j<n;j++)
    {
        if (ipiv[j] != 1)          /* skip, if diagonal element in jth row is a pivot */
        {
            for (k=0;k<n;k++)
            {
                if (ipiv[k] == 0)
```

```

        if (a[j][k] < 0)
            temp1 = -a[j][k];
        else
            temp1 = a[j][k];
        if (temp1 >= big)
        {
            big = temp1;
            irow=j;
            icol=k;
        }
    }
    else if (ipiv[k] > 1) return(1); /* Error: Singular Matrix-1 */
}
}
}
++(ipiv[icol]);          /* irow, icol should contain the position of pivot */
if (irow != icol)        /* if irow = icol, then pivot already in place */
{                          /* else position pivot by swapping rows */
    for (l=0;l<n;l++) SWAP(a[irow][l],a[icol][l])
    SWAP(b[irow],b[icol])
}
indxr[i]=irow;          /* keep track of the original pivot position */
indxc[i]=icol;

if (a[icol][icol] == 0.0) return(2); /* Error: Singular Matrix-2 */
pivin=1.0/a[icol][icol]; /* Now divide the pivot row by the pivot element */
a[icol][icol]=1.0;
for (l=0;l<n;l++) a[icol][l] *= pivin;
b[icol] *= pivin;

for (ll=0;ll<n;ll++)    /* Reduce the rows except the pivot one */
{
    if (ll != icol)
    {
        dum=a[ll][icol];
        a[ll][icol]=0.0;
        for (l=0;l<n;l++) a[ll][l] -= a[icol][l]*dum;
        b[ll] -= b[icol]*dum;
    }
}
}
/* End of Main Loop */
for (l=n-1;l>=0;l--)    /* Unscramble the solution by interchanging columns */
{
    if (indxr[l] != indxc[l])
        for (k=0;k<n;k++)
            SWAP(a[k][indxr[l]],a[k][indxc[l]]);
}
return(0);
}

```

## A.7 Program to Calculate Grain Boundary Energy Ratios

```
/*gdist.c*/
#include<stdio.h>
#include<math.h>
#include<stdlib.h>

#define PI 3.1415927

float gdist(float class[],float freq[],float cum[],int n);

main()
{
FILE *fa,*fb,*fc,*fd,*fe;
int i,j,m;
float
class[50],freq_max[50],freq_min[50],cum1[50],cum2[50],a1,a2,a3,b1,b2,b3,g_max,g
_min,g_middle,g_min_max,g_middle_max;
char max_tda[50],min_tda[50],output1[50],output2[50];

fa=fopen("\\tc\\source\\arijit\\class.txt","r");
for(i=0;i<17;i++)
{
fscanf(fa,"%f",&class[i]);
}

printf("\nInput MAX_TDA File : ");
scanf("%s",max_tda);
printf("\nInput MIN_TDA File : ");
scanf("%s",min_tda);
printf("\nOutput File (g1/g3):");
scanf("%s",output1);
printf("\nOutput File (g2/g3):");
scanf("%s",output2);

fb=fopen(max_tda,"r");
fc=fopen(min_tda,"r");
fd=fopen(output1,"w");
fe=fopen(output2,"w");

for(i=0;i<17;i++)
fscanf(fb,"%f",&freq_max[i]);

for(i=0;i<17;i++)
fscanf(fc,"%f",&freq_min[i]);

printf("No of Iteration : ");
```

```

for(j=0;j<m;j++)
{
a1=gdist(class,freq_max,cum1,17);
a2=gdist(class,freq_min,cum2,17);
a3=360-(a1+a2);
b1=sin(PI*a1/180);
b2=sin(PI*a2/180);
b3=sin(PI*a3/180);
if(b1>b2)
{
if(b2>b3)
{g_max=b1;g_min=b3;g_middle=b2;}
else
if(b1>b3)
{g_max=b1;g_min=b2;g_middle=b3;}
else
{g_max=b3;g_min=b2;g_middle=b1;}
}
else
{
if(b3>b2)
{g_max=b3;g_min=b1;g_middle=b2;}
else
if(b1<b3)
{g_max=b2;g_min=b1;g_middle=b3;}
else
{g_max=b2;g_min=b3;g_middle=b1;}
}
g_min_max=g_min/g_max;
g_middle_max=g_middle/g_max;
if((g_min_max < 0) || (g_middle_max<0))
{
printf("%f, %f, %f, %f\n",a1,a2,g_min_max,g_middle_max);
}
fprintf(fd,"%f\n",g_min_max);
}

fclose(fa);
fclose(fb);
fclose(fc);
fclose(fd);

getch();
}

```

```

float gdist(float class[],float freq[],float cum[],int n)
{
int i;

```

```

cum[0]=freq[0];
for(i=1;i<n;i++)
{
cum[i]=cum[i-1]+freq[i];          /* calculation of cumulative frequency*/
}

f=((float)rand())/RAND_MAX;    /* random number generation*/

i=0;
while(f > cum[i])
    i++;

upper=class[i];
uf=cum[i];
if(i>0)
{
    lower=class[i-1];
    lf=cum[i-1];
}
else
{
    lower=0;
    lf=0;
}

if(uf>lf)
{
    y=(upper*(f-lf)+lower*(uf-f))/(uf-lf);
    return(y);
}
else
    return(-1);
}

```

A 141866



A141866

---